QUANTIZED GROWTH OF SEMICONDUCTOR NANOPARTICLES, INVESTIGATION OF AGGREGATION DYNAMICS AND THE GROWTH KINETICS

by

PINAR DAGTEPE

B.S., IZMIR INSTITUTE OF TECHNOLOGY,IZMIR,TURKEY, 2003
M.S., IZMIR INSTITUTE OF TECHNOLOGY,IZMIR,TURKEY, 2005

AN ABSTRACT OF A DISSERTATION

submitted in partial fulfillment of the requirements for the degree

DOCTOR OF PHILOSOPHY

Department of Chemistry
College of Arts and Sciences

KANSAS STATE UNIVERSITY
Manhattan, Kansas

2010

Abstract

Colloidal semiconductor nanoparticles will be important and practical next generation materials that can be cheaply manufactured. The objective of this project is to gain more inside into chemistry is used to control the formation and assembly of semiconductor nanoparticles (NPs). As a model system CdSe and CdTe nanoparticles are used in this work. The growth kinetics, aggregation dynamics, and heterogeneous growth of NPs by using novel tools such as; *in-situ* monitored fluorescence and absorption techniques, time-resolved and static fluorescence spectroscopy, TEM (transmission electron microscopy), and numerical simulations are studied.

This study can be divided into the following four parts. The first part presents experimental observation of the quantized growth of CdTe quantum dots (QD). The high-temperature absorption spectra indicate the evolution of multiple peaks corresponding to various sizes of QDs. The observed aggregation is driven by dipole-dipole interaction of NPs. The second part is an investigation of the aggregation dynamics of magic-sized CdTe quantum dots and how this process can be controlled. It is shown that the growth kinetics of the QDs is very sensitive to the Cd/Te ratio. Cd-rich conditions form very different aggregation pattern due to the lack of formation of magic-sized nanoparticles. Simulations also suggest that the formation mechanism is mainly coalescence of the particles rather than the 'neck formation' within the CdTe aggregates. The next part investigates the growth of NPs in the presence of two distinctly sized NPs in the bimodal growth regime via numerical simulations. The bimodal distribution (or quantized Ostwald ripening) technique is found to be a slower process than the repeated injection technique to focus the size distribution of NPs. Slower growth will reduce inhomogeneity in a scaled-up production of NPs. The last part focuses on the effect of addition of doping on

heterogeneous growth and the growth kinetics. The low temperature synthesis lacks the heterogeneous growth regime. However, as the temperature is increased to 120 ^{0}C, two different sizes emerge. Addition of In dopants seems to accelerate the growth kinetics and the magic sized NPs in the solution possess a negative anisotropy that is most likely due to supperlatice formation of magic-sized NPs.

QUANTIZED GROWTH OF SEMICONDUCTOR NANOPARTICLES, INVESTIGATION OF AGGREGATION DYNAMICS AND THE GROWTH KINETICS

by

PINAR DAGTEPE

B.S., IZMIR INSTITUTE OF TECHNOLOGY,IZMIR,TURKEY, 2003
M.S., IZMIR INSTITUTE OF TECHNOLOGY,IZMIR,TURKEY, 2005

A DISSERTATION

submitted in partial fulfillment of the requirements for the degree

DOCTOR OF PHILOSOPHY

Department of Chemistry
College of Arts and Sciences

KANSAS STATE UNIVERSITY
Manhattan, Kansas

2010

Approved by:

Major Professor
Viktor Chikan

Copyright

Abstract

Colloidal semiconductor nanoparticles will be important and practical next generation materials that can be cheaply manufactured. The objective of this project is to gain more inside into chemistry is used to control the formation and assembly of semiconductor nanoparticles (NPs). As a model system CdSe and CdTe nanoparticles are used in this work. The growth kinetics, aggregation dynamics, and heterogeneous growth of NPs by using novel tools such as; *in-situ* monitored fluorescence and absorption techniques, time-resolved and static fluorescence spectroscopy, TEM (transmission electron microscopy), and numerical simulations are studied.

This study can be divided into the following four parts. The first part presents experimental observation of the quantized growth of CdTe quantum dots (QD). The high-temperature absorption spectra indicate the evolution of multiple peaks corresponding to various sizes of QDs. The observed aggregation is driven by dipole-dipole interaction of NPs. The second part is an investigation of the aggregation dynamics of magic-sized CdTe quantum dots and how this process can be controlled. It is shown that the growth kinetics of the QDs is very sensitive to the Cd/Te ratio. Cd-rich conditions form very different aggregation pattern due to the lack of formation of magic-sized nanoparticles. Simulations also suggest that the formation mechanism is mainly coalescence of the particles rather than the 'neck formation' within the CdTe aggregates. The next part investigates the growth of NPs in the presence of two distinctly sized NPs in the bimodal growth regime via numerical simulations. The bimodal distribution (or quantized Ostwald ripening) technique is found to be a slower process than the repeated injection technique to focus the size distribution of NPs. Slower growth will reduce inhomogeneity in a scaled-up production of NPs. The last part focuses on the effect of addition of doping on

heterogeneous growth and the growth kinetics. The low temperature synthesis lacks the heterogeneous growth regime. However, as the temperature is increased to 120 ^{0}C, two different sizes emerge. Addition of In dopants seems to accelerate the growth kinetics and the magic sized NPs in the solution possess a negative anisotropy that is most likely due to supperlatice formation of magic-sized NPs.

Table of Contents

List of Figures

List of Tables

Acknowledgements

First of all, I would like to express my gratitude to my doctorate major professor Dr. Viktor Chikan for his guidance, encouragement and support. I am grateful for this opportunity for pursuing my career.

Secondly, I would like to thank my graduate committee members: Professor Bossman, Professor Jankowiak, Professor Corwin and outside chairperson Professor Rezac for their valuable time, and discussions.

I would like to thank my labmates; Chris, Naween, Raj, Santanu and Dr. Mandal for their help.

Additionaly, I would like to thank several people working in chemistry department who helped me in various ways; Richard Bachamp, Ron Jackson, Tobe Eggers and Jim Hodgson for making and fixing electronics/instruments/glassware for my experiments, and Linda Gibbs and Mary Dooley for making my day with their cheerful smiles and providing me whatever I need in the storeroom.

I would like thank to all the friends I met along the way that gave me great opportunity to learn and experience their cultures and made me think it is not such a big world afterall.

I want to thank also one lovely person that made this journey better with her valuable discussions, different views and support; Prof. Carole Setser for her friendship for the last five years. She made me like home by cooking me some Turkish food and making me feel less homesick when talking about her almost a year stay in Istanbul.

Last but not least I would like to thank my family; my mom Senay, she is one of the strongest and most positive women I met in my life and was the one who made me hang in there

last five years of this journey, my dad Mustafa and my brothers, Fatih and Akin for their constant support love and care, I do not think that I would be the person I am now without their support. Thank you so much for being there and being so supportive at whatever I do and helping me find myself, I love you all so very much.

Dedication

To the loving memory of

Fatih Dagtepe, my brother

Preface

Growth of nanoparticles is investigated.

CHAPTER 1 - Introduction

Nanophase materials have been crucial in both fundamental research and technology in the last decade. Many interdisciplinary attempts have been made to advance nano-sized materials. Nanomaterials have many different shapes, sizes, and properties which lead to various functionalities. As a result of optical, electronic and magnetic properties of nanomaterials, they possess potential applications in imaging, photo-voltaics, fluorescent tags, energy conversion, biomedical applications and thin film coatings.[1] Most widely studied nanostructures are metals, oxides and semiconductors. One special class is the quantized semiconductor nanoparticles also known as quantum dots (QDs). QDs exhibit size-dependant electro-optical properties. Quantization in NPs is observed when particles have radii smaller than or equal to the average distance between electron and hole (Bohr radius). Electron and the holes are confined to an infinite potential. Therefore, QDs possess larger band gaps than the corresponding bulk material and also in discrete sets of energy states. As the size of the QDs is reduced, their absorbance spectra shift to shorter wavelengths (blueshift). [2]

Growth of Nanoparticles

Understanding of nanoparticle growth is important to produce good quality (monodisperse) particles with uniform properties. Synthesizing NPs with desired size and size distribution affects the properties which is very important in order for them to be used in specific applications. In order to obtain monodisperse colloidal particles, the nucleation and growth processes must be separated.[3] In this process of separation nucleation from the growth, fast nucleation is followed by a slow controlled growth. In order to achieve nucleation, the solution must be supersaturated. Supersaturation takes place when the solute is dissolved at high temperature and then cooled

down or by directly addition of reactants to get supersaturated solution. In the nucleation process, nucleation takes place due to the instability of the supersaturated solution. The total free energy of the system after formation of new volume and the new surface is given by the following equation;[4]

$$\Delta G = -\frac{4}{3V_m}\pi r^3 RT\ln(S) + 4\pi r^2\gamma \qquad (1.1)$$

$$d\Delta G / dr = 0 \qquad r^* = \frac{2\gamma V_m}{RT\ln S} \qquad (1.2)$$

where γ is the surface free energy, V_m is the molar volume R is the gas constant, r is the particle size, and S is the saturation ratio.

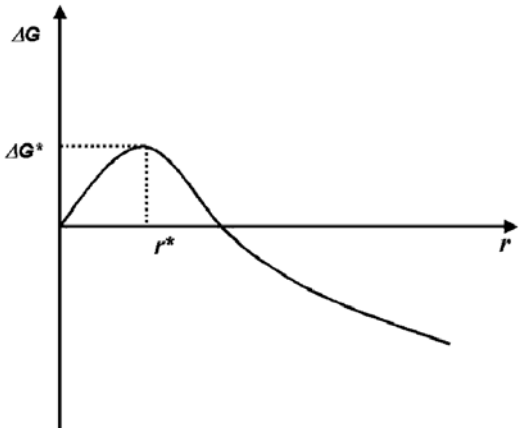

Figure 1.1 Overall free energy as a function of particle size[4]

Figure 1.1 gives the free energy change as a function of particle radius. The maximum in the graph indicates the free energy at so called "critical size" (equation 1.2) which takes place when S > 1. This maximum free energy corresponds to the activation energy for the nucleation. As the figure shows, after the activation energy for the nucleation is reached, nuclei larger than the critical radius have lower free energy.

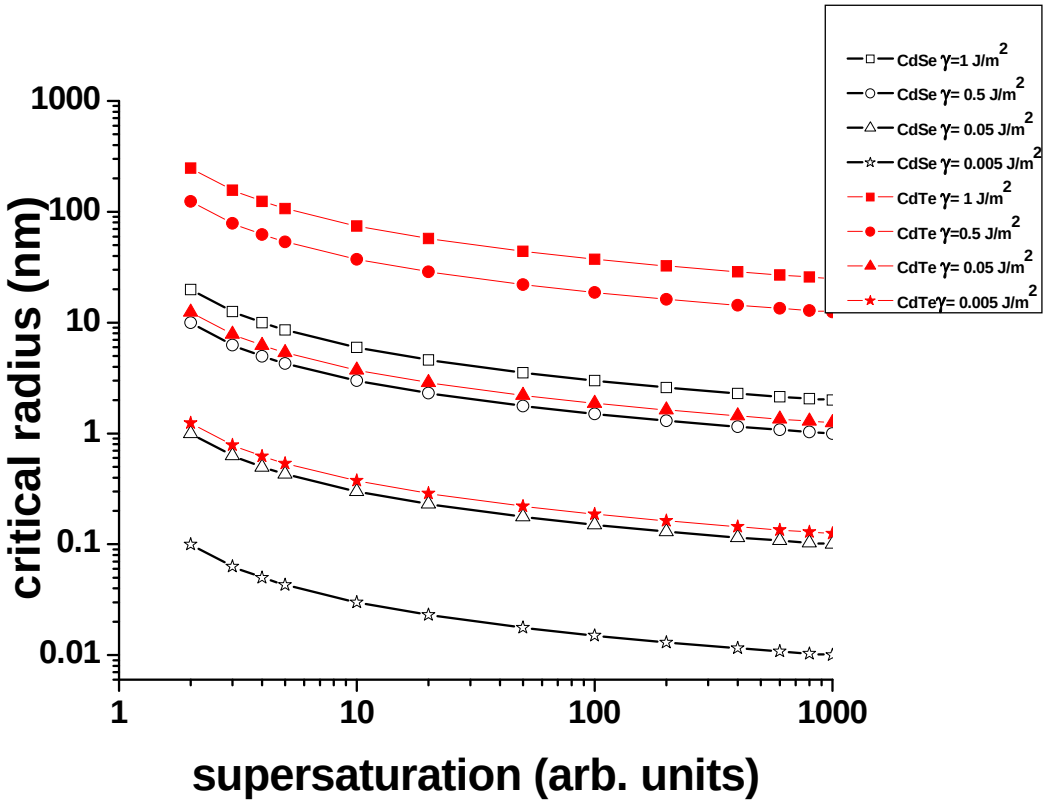

Figure 1.2 Change of critical radius with different supersaturation values for CdSe and CdTe NPs

Figure 1.2 presents how critical radius changes with different supersaturation values for different NPs (CdSe and CdTe). The relation between critical radius and the supersaturation is given by equation 1.2. As the equation and also Figure 1.2 indicate, with decreasing critical radius the supersaturation value increases. CdSe NPs have lower critical radius value that is because they have smaller molar volume than CdTe NPs. The figure also shows the effect of changing the specific surface energy values. As the critical radius equation shows, high surface

energies cause larger critical radii. Therefore, at higher surface energy the critical value stays high as well.

Lamer diagram[5] illustrates below how the nucleation occurs in terms of concentration change. First, stage I, molecular precursors (monomers) form and monomer formation continues until the minimum concentration for the nucleation threshold (C^*_{min}) is exceeded. Nucleation (stage II) takes place when C^*_{min} is reached. Concentration of solute increases and reaches a maximum value of C^*_{max} and after that, it starts decreasing and when C^*_{min} value is reached again, the nucleation process stops. After the nucleation step, growth step (stage III) sets in and continues until solubility concentration (C_s) is reached.

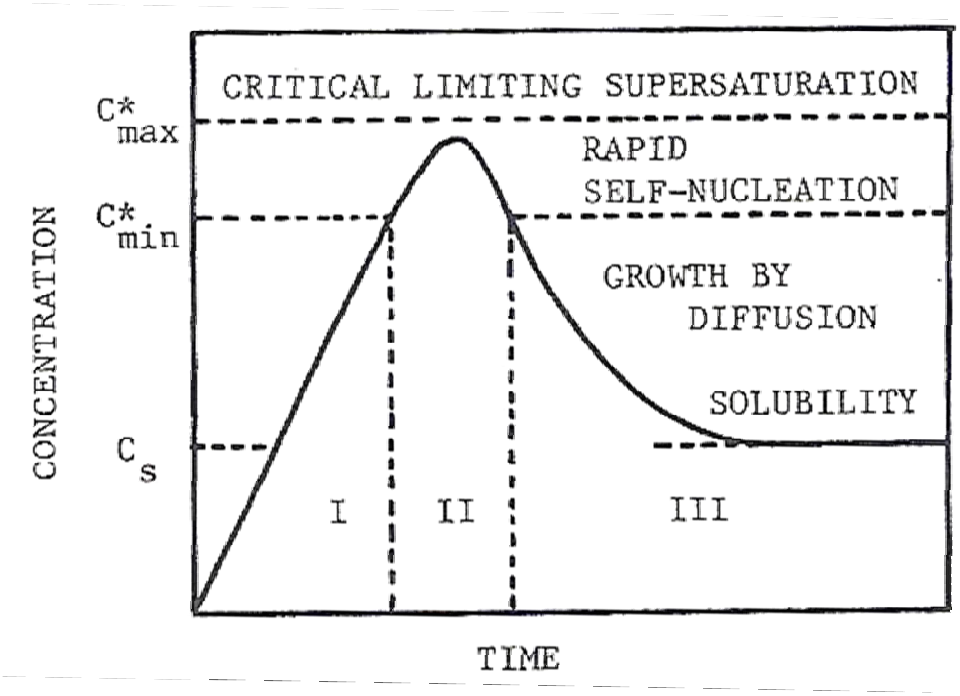

Figure 1.3 Lamer diagram- formation of monodisperse particles[5]

Above diagram shows that in order to separate nucleation and the growth processes, the nucleation rate should be high enough to exceed the growth stage. If concentration of the solute

is below C^*_{min}, then the nucleation and growth stages take place at the same time, which will produce a polydispersed solution. In the nucleation process, the concentration increases rapidly, and the supersaturation of the monomers takes place. Therefore, rapid growth of nuclei reduces the concentration below the nucleation concentration resulting in a slow rate of growth.

Mechanism of Growth

Nucleation of particles ends when the monomers are consumed in the process of surface growth of clusters, which happens when the monomer concentration decreases below the critical level of supersaturation (Figure 1.4). After the nucleation step, smaller particles (larger than the critical radius) tend to change their size faster than the larger ones in order to decrease their higher surface energies and at this step the "focusing" of the size distribution takes place. Figure 1.4 illustrates the overall nucleation, and growth stages. Due to the growth, concentration of the precursors is exhausted and the Ostwald ripening (defocusing) process which causes the broad size distribution to start.

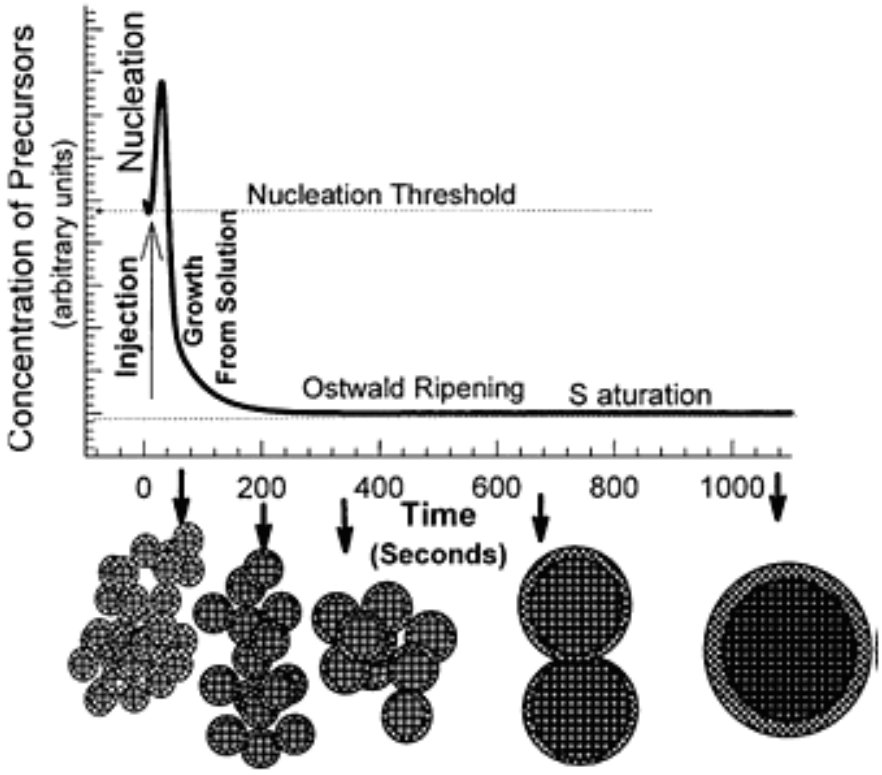

Figure 1.4 Growth of colloidal particles[6]

In colloidal particles, the growth takes place by the monomer diffusion at the surface of particles (Figure 1.5a). In the below diagram, δ is the thickness of the diffusion layer, c_b is the bulk monomer concentration, c_i is the monomer concentration at the particle interface, and c_e is the solubility of a particle with a radius r. Figure 1.5b is a diffusion layer of a spherical particle with r representing the radius of the particle, and x is the distance from center of the particle.

a) **b)**

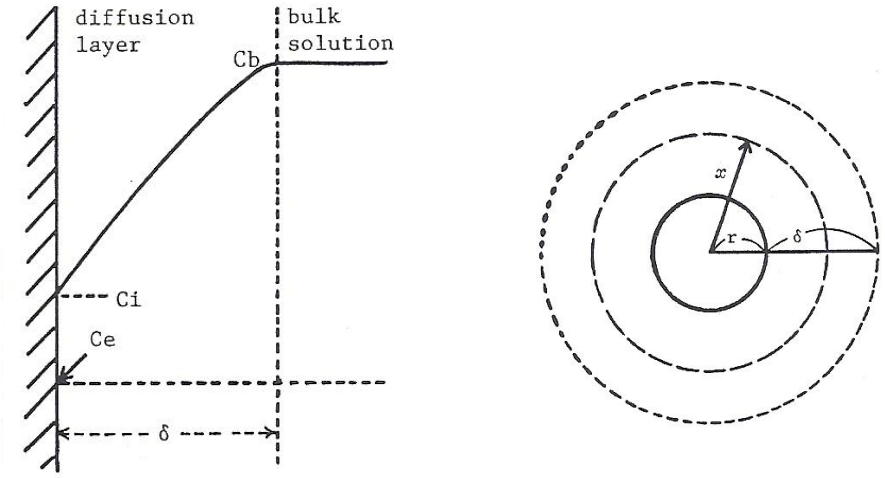

Figure 1.5 a) Sketch of solute concentration of a diffusion layer b) diffusion layer around a spherical particle [5]

Diffusion of the monomer from bulk to spherical particle surface is given by Fick`s first law; [7]

$$J = 4\pi x^2 DdC/dx \qquad (1.3)$$

In the equation J is the flux of monomers, D is the diffusion coefficient, C is the monomer concentration at x. At steady state condition, Fick`s first law can be integrated from r + δ to r (r is the average radius) and following equation results;[7]

$$J = \frac{4\pi Dr(r+\delta)}{\delta}(c_b - c_i) \qquad (1.4)$$

Under real conditions, the thickness of the diffusion layer is much larger than the size of the NP, so the equation can be simplified to;[7]

$$J = 4\pi r^2 k_g^{flat}(c_i - c_e) \qquad (1.5)$$

k_g^{flat} is the rate constant for a first order deposition reaction. The size dependent rate of the particle radius rate equation is given by;[7]

$$\frac{dr}{dt} = \frac{\frac{D}{r}\left(1+\frac{r}{\delta}\right)V_m\left(c_b - c_e\right)}{1+\frac{D}{k_g^{flat} r\left(1+\frac{r}{\delta}\right)}} \qquad (1.6)$$

Gibbs-Thompson equation in terms of c_e and c_b are given by the following equations respectively;[7]

$$c_e = C_{flat}^0 \exp\left(\frac{2\gamma V_m}{rRT}\right) \approx C_{flat}^0\left(1+\frac{2\gamma V_m}{rRT}\right) \qquad (1.7)$$

$$c_b = C_{flat}^0 \exp\left(\frac{2\gamma V_m}{r_b RT}\right) \approx C_{flat}^0\left(1+\frac{2\gamma V_m}{r_b RT}\right) \qquad (1.8)$$

where, C_{flat}^0 is the solubility of a flat particle. Since, under real conditions thickness of the diffusion layer is much larger than the size of the NP, size dependent particle radius rate equation can be expressed as follows;[8]

$$\frac{dr}{dt} = \frac{2\gamma V_m^2 C_{flat}^0}{RT(1/D + 1/k_g^{flat} r)}\frac{1/r_b - 1/r}{r} \qquad (1.9)$$

Diffusion-controlled growth

When D << k_g^{flat} r, the particle growth is defined as under diffusion control, particle growth is controlled by the monomer diffusion. It is observed when the diffusion is the slowest step in the particle growth process. Then, the growth rate equation reduces to the following form;[7]

$$\frac{dr}{dt} = \frac{2\gamma V_m^2 C_{flat}^0}{RT} \frac{r/r_b - 1}{r^2} = K_D \frac{(r/r_b - 1)}{r^2} \qquad (1.10)$$

LSW theory considers the growth process in terms of the diffusion limited growth and it investigates the supersaturated spherical particles. This theory explains Ostwald ripening process quantitatively.

Reaction-controlled growth

When k_g^{flat} << D, particle growth is defined as the reaction-controlled process, and the growth rate is limited by the surface reaction of monomers. In this case, the diffusing particles at the surface join to the growing particles and the growth process is controlled by the reaction of the monomers at the surface. The following growth rate equation is obtained as a result of the reaction-controlled growth;[7]

$$\frac{dr}{dt} = \frac{2\gamma V_m^2 k_g^{flat} C_{flat}^0}{RT} \frac{r/r_b - 1}{r} = K_R \frac{(r/r_b - 1)}{r} \qquad (1.11)$$

Finally, one of the most important differences between the reaction and the diffusion controlled processes is that, the size distribution observed in reaction-controlled growth is broader than the diffusion controlled growth.

Ostwald Ripening Process

When the concentration of precursor is depleted during the growth after the nucleation Ostwald ripening (coarsening) is the dominant mechanism of particle growth. In the Ostwald ripening process, the driving force for ripening is the curvature dependence (surface energy) of the chemical potential. In general, colloidal particles are inclined to minimize their surface-to-volume ratio, and thereby their surface free energy. Smaller particles possess higher chemical potential than larger ones, which leads to material transport from small to big particles

quantatively explained by Kelvin`s equation. As a result of that, larger particles continue to grow but smaller ones gets smaller and eventually disappear (Figure 1.6).[9] The figure demonstrates how the Ostwald ripening process occurs schematically. As time evolves from figure a to d, the number of droplets (particles) decreases and the average size increases. In this system, large particles grow by the evaporation and then condensation of material diffused from small droplets.

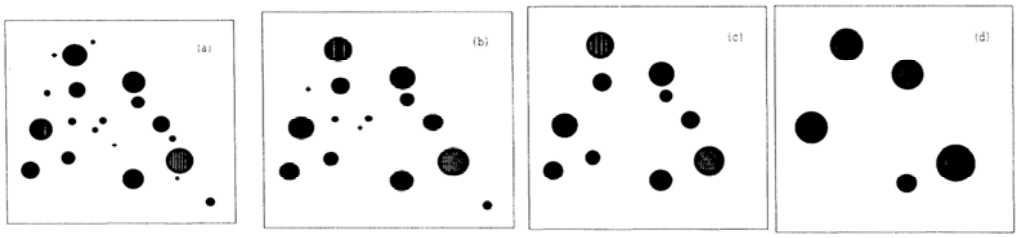

Figure 1.6 Ostwald ripening process in 2-dimension[9]

The Ostwald Ripening process, which is given by Kelvin`s equation is theoretically described by the Lifshitz-Slyozov-Wagner (LSW) theory. The LSW theory explains the diffusion-controlled coarsening in a stationary regime. This coarsening rate is given by;[8]

$$\nu = \frac{8\gamma V_m^2 D C_{flat}^0}{9RT} \quad (1.12)$$

The limiting stationary size distribution is given by the following equations;[8]

$$W(r/r_{cr}) = W(u) = \frac{(3^4 e/2^{5/3})u^2 \exp[-1/(1-2u/3)]}{[(u+3)^{7/3}(1.5-u)^{11/3}]} \qquad (1.13)$$

$$(0 \le u \le 15)$$

$$W(u) = 0 \qquad (u > 15) \qquad (1.14)$$

with a cut-off for u = 15 and here $\langle r \rangle = r_{cr}$. According to a simulation study by De Semet et. al.[10] of Ostwald Ripening process, following Figure 1.7 shows the initial size distribution of LSW

(curve 1) with a size distribution of 1.5 nm, Gaussian distribution with standard deviations of 4.5 nm (curve 2), 9 nm (curve 3) and a log-normal distribution with a 9 nm size distribution. Figure 1.8 shows the evolution of the initial Gaussian size distribution with a standard distribution of 1.5 nm. The standard deviation changes from the Gaussian distribution to LSW stationary distribution. Curve starts out with a narrow size distribution (curve 1, Figure 1.8) and broadens very rapidly (curve 2, Figure 1.8).

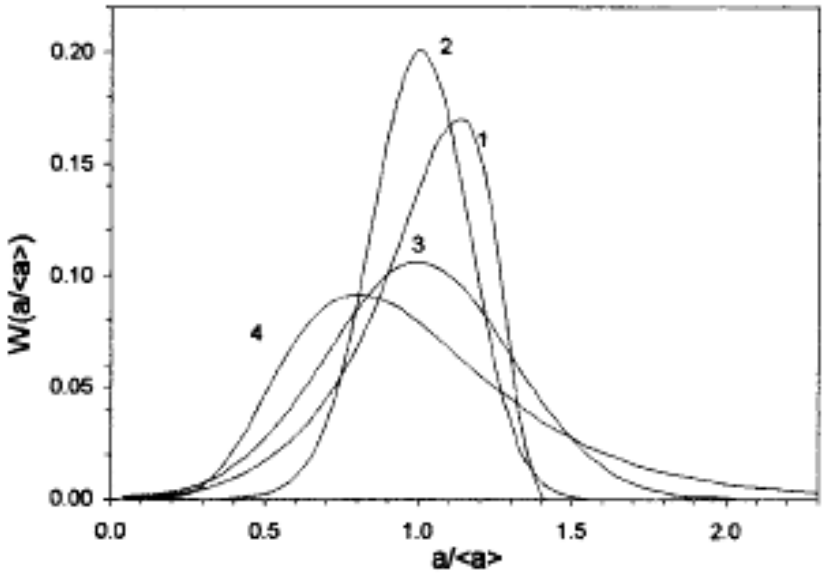

Figure 1.7 Different initial size distributions[10]

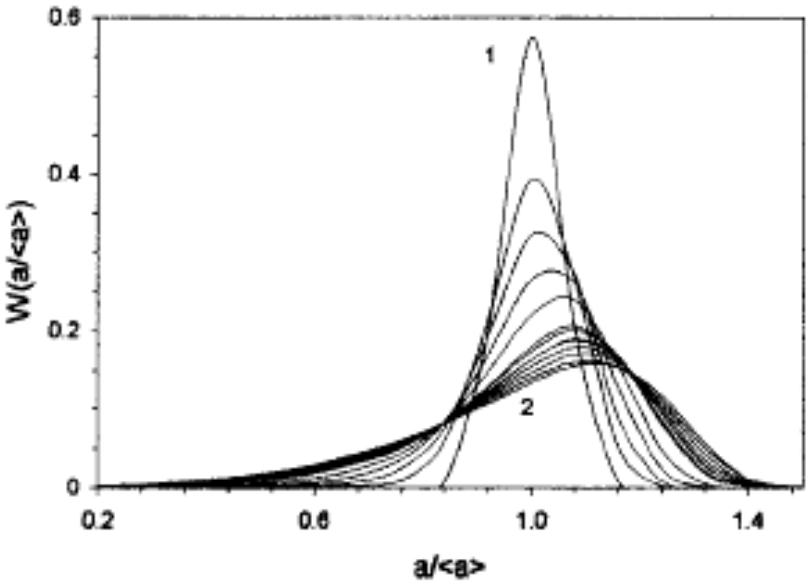

Figure 1.8 Evolution of the Gaussian size distribution[10]

Size Focusing and Narrow Size Distribution

Developing methods to obtain nanomaterials with uniform size and shape has been a challenge for nanosized material research. In crystal growth, obtaining monodispersed colloidal particles and controlling the growth are important not only in the field of physical chemistry but also in industries such as; catalysts, ceramic pigments, pharmacy, etc.[5] The general approach to generate particles with narrow size distribution is achieved by separating nucleation and growth processes in the high temperature colloidal nanoparticle synthesis. However, separating nucleation and growth by injection of molecular precursors to induce fast nucleation is not an easy process in terms of experimental conditions. A widely accepted approach to narrow the size distribution of NPs has been developed by Peng et. al.[4] by the multiple injection method. Figure 1.9a illustrates how the focusing of size distribution takes place stepwise by second injection of molecular precursor. After the first injection of molecular precursors, as can be seen from Figure 1.9b, the size distribution of NPs starts decreasing and the average size has a sharp increase. This step is

called “focusing of the size distribution”. During focusing, the monomer concentration decreases fast; on the other hand, number of particles remains constant. After the focusing step, the average particle size does not change drastically. There is a slower growth process that leads to de-focusing and larger size distribution. In order to focus the size distribution, a second molecular precursor injection takes place (re-focusing). During this “re-focusing” step, the number of particles remains constant, the monomer concentration drops drastically and the narrowing of the size distribution is observed.

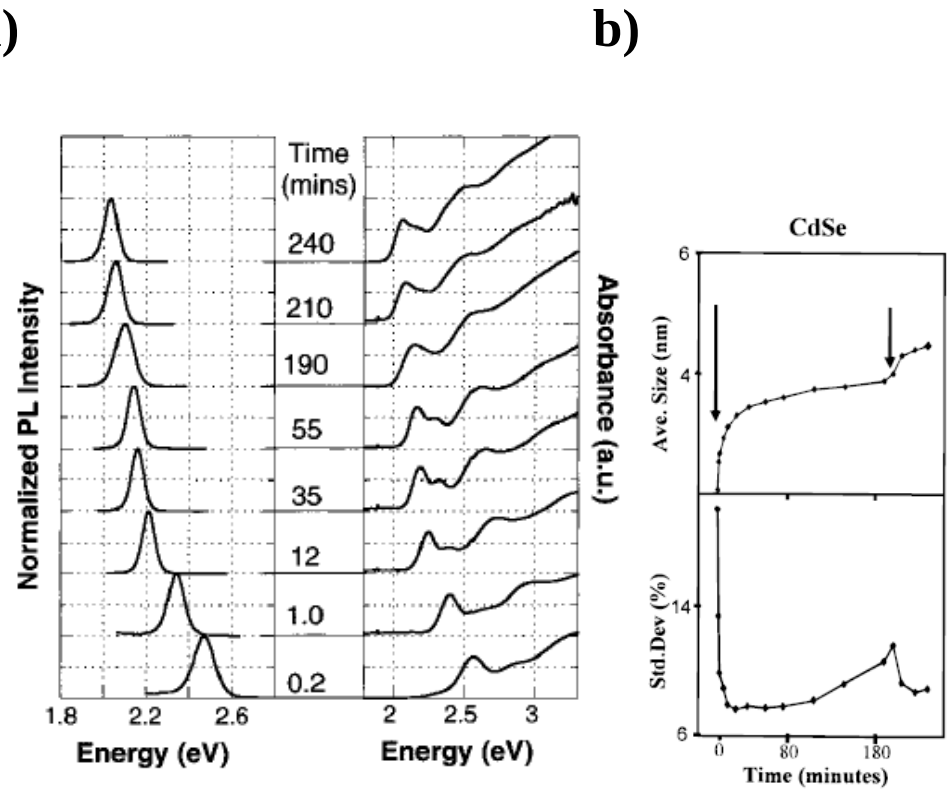

Figure 1.9 a) Absorption and photoluminescence spectra during multiple injection method b) temporal change of average size and the size distribution during multiple injection method[4]

When the diffusion-controlled growth rate is expressed as a function of critical radius (r*), the growth rate equation is given by the following equation;[4]

$$\frac{dr}{dt} = K_D(1/r + 1/\delta)(1/r^* - 1/r) \qquad (1.15)$$

Nanoparticles smaller than the critical radius value (negative growth rate) dissolve and particles larger than the critical radius value (positive growth rate) grow. Focusing of the NP size takes place when the NPs are slightly larger than the critical radius. Size distribution starts broadening (de-focusing) when the monomers are consumed and the critical radius becomes larger than the average NP size in the system. At this stage, a second injection of molecular precursors is applied to focus the size distribution and the critical radius gets smaller.

Shape-Guiding Growth Mechanism

Shape control of nanomaterials leads to different types and different functionalities. Most of the literature work has been focused on the 1-dimensional systems. Nanorods growth is an example of the basic anisotropic growth. Therefore, understanding the growth of nanorods leads to ways to understanding the growth of more complicated structures such as, tetrapods, star-shaped nanostructures and so forth. Studying the mechanisms of the nanorod growth is significant not just for 1-dimensional structures but also for more complicated structures. Key factor in shape control of crystals is the surface free energy of the individual faces. Free energy is minimized, which is the factor determining the overall shape of the crystal structure. In order to modify the surface free energy, different surfactant mixtures are used, which leads to the selective adsorption of surfactants at different faces of the crystal. As a result of selective adsorption, crystallographic growth at different planes takes place and it is the reason for observed shape anisotropy. In such methods, syntheses similar to the spherical nanoparticles syntheses are

applied and different surfactant mixtures (TOPO and HPA in CdSe synthesis) are used to cause the anisotropy on the crystal surface. Another method which has been studied more recently is called the oriented attachment method.[11] In this growth method, crystals attach in a specific crystallographic phase and shape then transformation takes place. In nanocrystals, the surface to volume ratio is higher than the bulk phase; therefore surface energy plays a significant role on the overall energy of the system. In order to obtain lower energy surfaces, aggregation or growth of particles contributes to lowering of the energy of the NPs. The aggregation of the particles is described by the Smoluchowski equation;[12, 13]

$$\frac{dn_k}{dt} = \frac{1}{2}\sum_{i=1}^{k-1} q(k-1,i)n_{k-i}n_i - n_k\sum_{i=1}^{\infty} q(i,k)n_i \qquad (1.16)$$

Here, dn/dt describes the population change of the k^{th} particles due to the formation of new aggregates from smaller particles. In this equation, q is the collision frequency of particles i and j. D_i is the size-dependent diffusion coefficient of particle i.

$$q(i,j) = 4\pi(D_i + D_j)(R_i + R_j) \qquad (1.17)$$

$$D_i = \frac{k_B T}{6\pi\mu R_i} \qquad (1.18)$$

In oriented attachment, particles self organize by a common crystallographic orientation then attach at a planar interface.[14] As a result of self organization and joining of particles, the overall energy decreases by reducing the surface to volume ratio. During the attachment, twin boundaries and/or defects form which separate the crystals. The mechanism of oriented attachment has been applied on many different nanodot systems to form nanorods/nanowires (Figure 1.10). In the CdTe system, starting from the nanodots, formation of nanowires has been observed.[15, 16] In this system, first the surfactants from the surface of the nanodots are removed

and then self assembling of particles into a "pearl necklace aggregate" takes place, following nanowire formation (Figure 1.11). The reason behind the formation of such structures starting from the nanodots is attributed to the intermolecular forces between the particles. One of the intermolecular interactions is the hydrogen bonding caused by the stabilizers and another interaction is the van der Waals forces between the anisotropic nanoparticles forming the aggregates. However, the effect of van der Waals forces and the Hydrogen bonding is minor when it is compared to the effect of dipole-dipole interactions which is a stronger force. Dipole-dipole interactions are originated from the polar character of the crystals being attached. Due to the electronegativity differences in the crystals, the polar character emerges.[14]

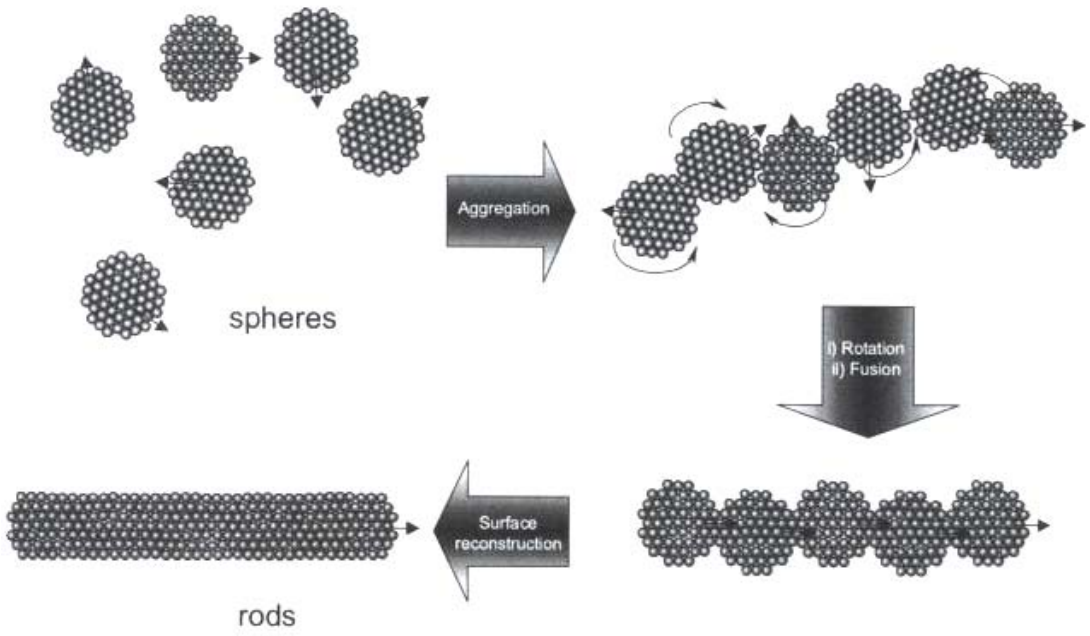

Figure 1.10 Oriented attachment process[11]

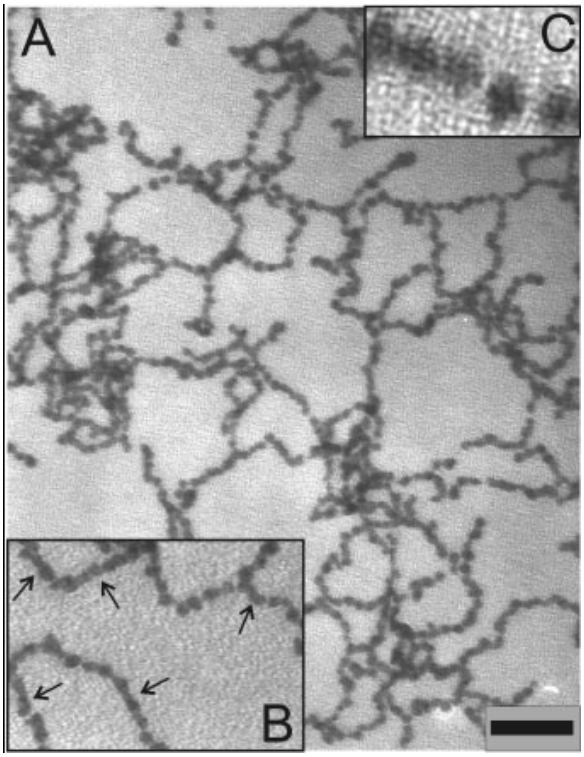

Figure 1.11 Experimental result of oriented attachment process, formation of pearl necklace aggregate formation[15]

Formation of aggregation is starting from the magic size nanoclusters also leads to formation of nanowires after the surface modification.[17] Magic size particles are very small, in the size range of 1-2 nm (CdSe). They are very stable particles with a closed shell structure. Due to the closed-shell structure, these clusters are thermodynamically more stable than materials without a closed-shell structure. Because of the stability, magic size particles appear at a certain size and remain for a long time during the growth.

Effect of Doping on NP Growth

Dopants are foreign atoms added to change electronic the properties of the NPs. [23, 24] When dopants are added to the growth solution of NPs, they are expected to affect the growth kinetics of NPs, which is an area has not been studied in great details. Interesting questions are

how dopants affect the growth of NPs and how the dopant will be distributed inside the NPs. Experimentally, this question is recently studied by our group by investigating the addition of In atoms to the growth solution of CdSe NPs. In this system, In dopants can cause the increase of the growth and dissolution rate of NPs. Addition of dopants accelerate the dissolution of magic-sized particles present in the reaction solution. In dopants increase the growth rate due to the surface energy change when a + 3 ion replaces a + 2 charged ion. This surface energy change makes the rate of attachment of next monomer to the particle surface faster than the rate of detachment. Some of the basic thermodynamics of doped nanoparticles is discussed in the next paragraph. Doping can be considered as a special case of binary mixture when one of the components is significantly less (dopant) than the other (host) material. During nanoparticle growth in the solution when dopants are present, the components of the NPs (the dopant and the host) interchange with the components dissolved in the growth solution. Whether growth or dissolution will take place, it depends on the chemical potential difference of the dopant and the host in the NP and the solution, therefore understanding the components of the free energy of binary mixture is important. Qualitative explanation of free energy diagram of a generic binary system is shown in Figure 1.12. As it shown in the figure, the chemical potential of the dopant and the host is the projected slope at $x_B=0$ and $x_B=1$, respectively. Briefly, the three main contributions to the free energy of binary mixture of the NPs are the entropic contribution (a), the enthalpic contribution that can be either positive (c) or negative (b) and the contribution of the surface energy that is usually positive (d). To quantify the relative contributions of each of these components is difficult, but it is clear that the chemical pontential difference for the dopant and host compnennt varies differently, therefore it is expected that doped NPs will grow at a different rate than their undoped counterparts. Experimentally, the addition of dopant molecules can

enhance the growth rate of NPs as it has been observed for In doping of CdSe[25] where, addition of dopants enhances the growth kinetics of CdSe NPs.

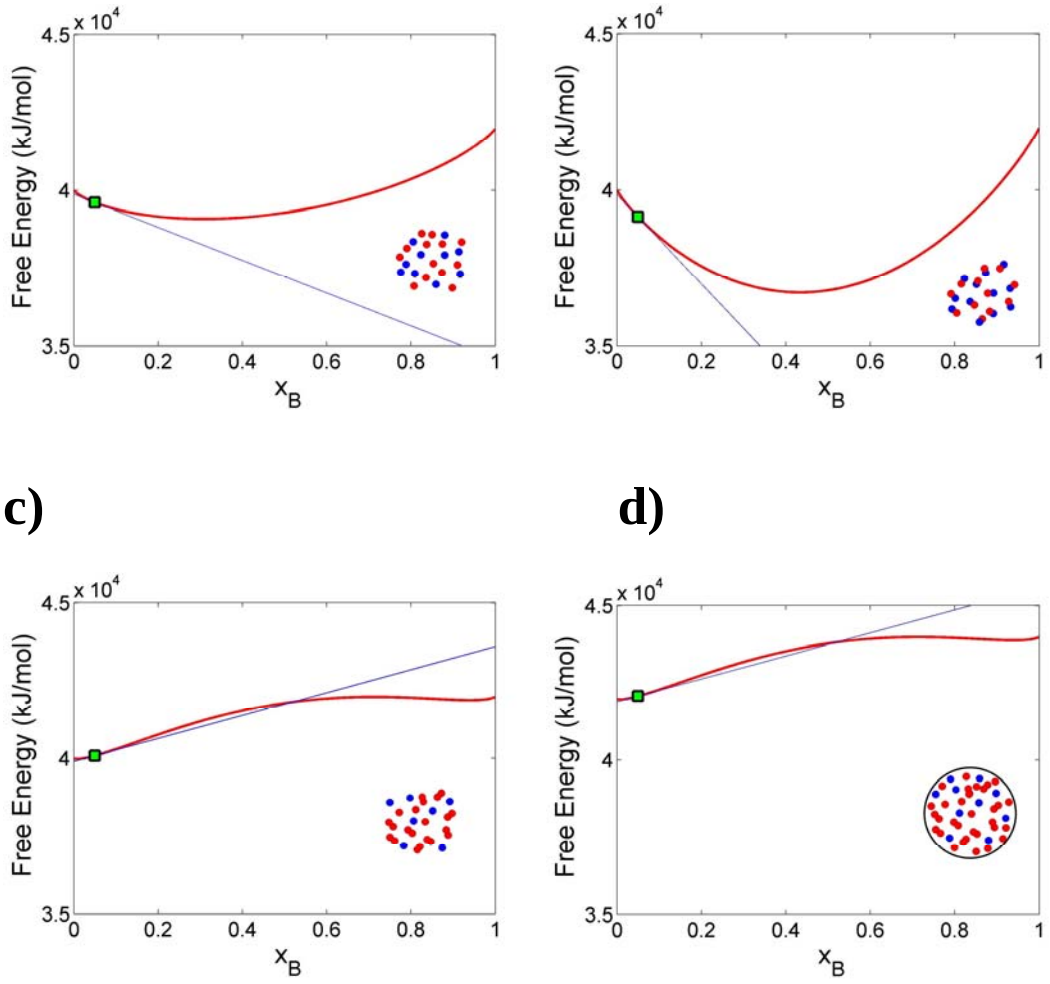

Figure 1.12 Free energy change by addition of dopant molecules

Goals of the Current Research

Significant research efforts have been spent on investigating the properties of semiconductor nanoparticles to attain well defined colloidal particles with uniform size and distribution. In this work much of the effort has been spent on the investigation of growth mechanism of colloidal NPs by using different experimental and simulation tools. In the following sections, the general aspects of the research explored will include: observation of the magic-sized CdTe QDs[27], the aggregation of CdTe during high temperature synthesis; controlling the aggregation of CdTe magic-sized NP system[28]; quantized Ostwald ripening in bimodal growth regime and size focusing phenomenon; and the last part will focus on the time resolved fluorescence spectroscopy of NPs including; magic-sized NPs, and doped and undoped CdSe nanostructures. Overall, the conducted research will shed light mostly on the fundamental aspects of nanoparticle growth, investigating ways to control the growth and eventually achieving routes to conjugate previous experimental methods as well as simulation approaches to obtain uniform materials. Chapter two and the chapter three, the properties of CdTe NPs has been investigated and the resultant conclusions is just for CdTe specific and cannot be generalized for a large scope of NPs. However, chapter four, the simulation study, can be generalized for NPs and the results and the conclusions can be applied to other NPs as well.

The following chapters have been focused on achieving following specific research goals:

- Investigating the growth kinetics of aggregation of magic-sized CdTe QDs in the presence of HDA and TOPO coordinating solvents mixtures

- Designing and developing an experimental and a simulation method to investigate the reasoning behind the aggregation dynamics of magic-sized CdTe NPs and controlling the aggregation mechanism
- Developing a method based on Monte Carlo simulation to explore the growth of colloidal semiconductor NPs in the presence of two distinct sized NPs (bimodal growth regime) to achieve narrowing of the size distribution of NPs
- Exploring the effect of the doping on the NP growth by time-resolved fluorescence spectroscopy

References

1. Kamat, P. K., & Meisel, D., *Semiconductor nanoclusters-physical, chemical, and catalytic aspects*. Elsevier: 1997; Vol. 103, p 5-8.

2. Owens, F. J., Poole, C. P., *The physics and chemistry of nanosolids*. Wiley: 2008; p 104-106.

3. Peng, Z. A.; Peng, X. G., Nearly monodisperse and shape-controlled CdSe nanocrystals via alternative routes: Nucleation and growth. *Journal of the American Chemical Society* **2002,** 124, (13), 3343-3353.

4. Burda, C.; Chen, X. B.; Narayanan, R.; El-Sayed, M. A., Chemistry and properties of nanocrystals of different shapes. *Chemical Reviews* **2005,** 105, (4), 1025-1102.

5. Sugimoto, T., Preparation of Monodispersed Colloidal Particles. *Advances in Colloid and Interface Science* **1987,** 28, (1), 65-108.

6. Murray, C. B.; Kagan, C. R.; Bawendi, M. G., Synthesis and characterization of monodisperse nanocrystals and close-packed nanocrystal assemblies. *Annual Review of Materials Science* **2000,** 30, 545-610.

7. Rao, C. N. R., Muller, A., Cheetham, A. K., *Nanomaterials chemistry*. Wiley-VCH: 2007; p 1-3.

8. Talapin, D. V.; Rogach, A. L.; Haase, M.; Weller, H., Evolution of an ensemble of nanoparticles in a colloidal solution: Theoretical study. *Journal of Physical Chemistry B* **2001,** 105, (49), 12278-12285.

9. Yao, J. H.; Elder, K. R.; Guo, H.; Grant, M., Theory and Simulation of Ostwald Ripening. *Physical Review B* **1993,** 47, (21), 14110-14125.

10. De Smet, Y.; Deriemaeker, L.; Finsy, R., A simple computer simulation of Ostwald ripening. *Langmuir* **1997,** 13, (26), 6884-6888.

11. Peng, X. G.; Wickham, J.; Alivisatos, A. P., Kinetics of II-VI and III-V colloidal semiconductor nanocrystal growth: "Focusing" of size distributions. *J. Am. Chem. Soc.* **1998,** 120, (21), 5343-5344.

12. Rotello, V., *Nanoparticles*. Kluwer: 2004; p 29-32.

13. Ethayaraja, M.; Bandyopadhyaya, R., Mechanism and modeling of nanorod formation from nanodots. *Langmuir* **2007,** 23, (11), 6418-6423.

14. Friedlander, S. K., *Smoke, Dust, and Haze: Fundamentals of Aerosol Dynamics*. 2000.

15. Kumar, S.; Nann, T., Shape control of II-VI semiconductor nanomateriats. *Small* **2006,** 2, (3), 316-329.

16. Tang, Z. Y.; Wang, Y.; Shanbhag, S.; Giersig, M.; Kotov, N. A., Spontaneous transformation of CdTe nanoparticles into angled Te nanocrystals: From particles and rods to checkmarks, X-marks, and other unusual shapes. *Journal of the American Chemical Society* **2006,** 128, (20), 6730-6736.

17. Zhang, Z. L.; Tang, Z. Y.; Kotov, N. A.; Glotzer, S. C., Simulations and analysis of self-assembly of CdTe nanoparticles into wires and sheets. *Nano Letters* **2007,** 7, (6), 1670-1675.

18. Riehle, F. S.; Bienert, R.; Thomann, R.; Urban, G. A.; Krugert, M., Blue Luminescence and Superstructures from Magic Size Clusters of CdSe. *Nano Letters* **2009,** 9, (2), 514-518.

19. Jun, Y. W.; Lee, S. M.; Kang, N. J.; Cheon, J., Controlled synthesis of multi-armed CdS nanorod architectures using monosurfactant system. *Journal of the American Chemical Society* **2001,** 123, (21), 5150-5151.

20. Manna, L.; Scher, E. C.; Alivisatos, A. P., Synthesis of soluble and processable rod-, arrow-, teardrop-, and tetrapod-shaped CdSe nanocrystals. *Journal of the American Chemical Society* **2000,** 122, (51), 12700-12706.

21. Peng, X. G.; Manna, L.; Yang, W. D.; Wickham, J.; Scher, E.; Kadavanich, A.; Alivisatos, A. P., Shape control of CdSe nanocrystals. *Nature* **2000,** 404, (6773), 59-61.

22. Peng, Z. A.; Peng, X., Mechanisms of the Shape Evolution of CdSe Nanocrystals. *Journal of the American Chemical Society* **2001,** 123, (7), 1389-1395.

23. Bryan, J. D.; Gamelin, D. R., Doped Semiconductor Nanocrystals: Synthesis, Characterization, Physical Properties, and Applications. In *Progress in Inorganic Chemistry, Vol 54*, John Wiley & Sons Inc: New York, 2005; Vol. 54, pp 47-126.

24. Sun, C.-J.; Wu, Y.; Xu, Z.; Hu, B.; Bai, J.; Wang, J.-P.; Shen, J., Enhancement of quantum efficiency of organic light emitting devices by doping magnetic nanoparticles. *Applied Physics Letters* **2007,** 90, (23), 232110-232110-3.

25. Tuinenga, C.; Jasinski, J.; Iwamoto, T.; Chikan, V., In situ observation of heterogeneous growth of CdSe quantum dots: Effect of indium doping on the growth kinetics. *Acs Nano* **2008,** 2, (7), 1411-1421.

26. Atkins P., P. d. J., *Physical Chemistry*. seventh ed.; Oxford University Press Inc.: New York, 2002.

27. Dagtepe, P.; Chikan, V.; Jasinski, J.; Leppert, V. J., Quantized growth of CdTe quantum dots; Observation of magic-sized CdTe quantum dots. *Journal of Physical Chemistry C* **2007,** 111, (41), 14977-14983.

28. Dagtepe, P.; Chikan, V., Effect of Cd/Te ratio on the formation of CdTe magic-sized quantum dots during aggregation. *Journal of Physical Chemistry A* **2008,** 112, (39), 9304-9311.

CHAPTER 2 - Quantized Growth of CdTe Quantum Dots; Observation of Magic-Sized CdTe Quantum Dots

Introduction

Understanding and controlling the growth of semiconductor QDs is an important step towards developing materials with well defined optical and physical properties. One challenge of growing semiconductor nanoparticles is to obtain QDs with well defined size and narrow size distribution. The rapid development in synthetic procedures has allowed growing semiconductor nanoparticles of narrow sizes and of various shapes[1]. The resulting new semiconductor nanostructures exhibit new interesting phenomena not observable otherwise. For instance, magic-sized CdSe has very broad so called white light emission[2] with appreciable emission quantum yield, which is very different from the very narrow bandgap emission observed from typical semiconductor QDs. The white light emission from magic-sized QDs has the potential to be very useful as a phosphor in efficient lighting applications.

One of the most common synthetic procedures of growing CdX (Te, S, Se) semiconductor nanoparticles is based on the high temperature synthesis described by Bawendi et. al.[3] The synthesis is carried out at 200-350 °C in the presence of a coordinating solvent such as TOPO. The Cd and X precursor molecules are injected into the hot, rapidly stirring solution forming CdX monomers complexed by a coordinating solvent. After the fast nucleation, the subsequent reaction of the monomers leads to the slow growth of semiconductor nanocrystals. Depending on the experimental conditions, the method yields QDs with very narrow size distributions. The average size and size distribution of the QDs is determined by the growth and the dissolution kinetics. A widely accepted explanation of the growth kinetics of the QDs in high

temperature coordinating solvents is described by Talapin et. al.[4] The model calculates the size-dependent growth rate of the nanoparticles, which leads to accurate prediction of the self focusing and Oswald ripening of the nanoparticle ensemble.

There are numerous examples when the size and size distribution of the nanoparticle growth is determined by the thermodynamics of the nanoparticles rather than the kinetics. The thermodynamic control of the nanoparticle growth may lead to the formation of magic-sized nanoparticles. The realization of magic size can be the result of a stable electronic structure. One example of such a magic size cluster is Au_{55}, which shows extreme stability.[5] The intrinsic stability of Au_{55} is the result of the closed shell electronic structure of the cluster. Another reason for large thermodynamic stability may originate from the delicate balance between the surface and the intrinsic energy of the nanoparticle. An example of a magic-sized nanoparticle where the surface plays an important role is gold again.[6] Digestive ripening of polydisperse gold nanoparticles in the presence of excess amount of alkane thiols yields narrowing in size distribution. The details of the theory of surfactant-mediated size control of Au nanocrystals are described in the literature.[7] Observation of magic-sized clusters is not unique to metal clusters. Ptatschek et. al. observed the formation of several magic-sized II-VI semiconductor colloids during room temperature synthesis.[8] Rogach et. al. also observed the formation of magic-sized CdTe and CdSe clusters in the presence of thiol capping agent at relatively moderate synthetic temperatures.[9,10] Some of these clusters undergo quantized aggregation resulting in larger clusters similar to the observation in this study, but at much lower synthetic temperatures.[8,11] Clearly, in these studies the surface ligands play the critical role in determining the size of the magic-sized clusters and their aggregation kinetics.

This work presents experimental evidence of magic size CdTe QDs in the presence of HDA and TOPO coordinating solvent mixture during crystal growth. The growth kinetics of the CdTe QDs indicates coalescent or quantized growth of smaller QDs into larger QDs. The smallest observed magic-sized CdTe QD are isolated and fractionated into either to polar methanol phase or toluene phase. The methanol phase QDs exhibit very broad white light emission with approximately 4% emission quantum yield. The toluene phase magic-sized QDs indicate a very different, but complex emission behavior with reduced quantum yield.

Experimental Section

Chemicals: tellurium powder (99.999%), CdO (99.999%), trioctylphosphine (TOP) (97%) are purchased from Strem. Trioctylphosphine oxide (TOPO) (90%), 1-hexadecylamine (HDA) (90%), anhydrous methanol (99.8%), anhydrous toluene (99.8%) are obtained from Sigma Aldrich. n-hexylphosphonic acid (HPA) (100%) is obtained from Alfa Aesar. TOPO, TOP and HDA are purified by vacuum distillation.

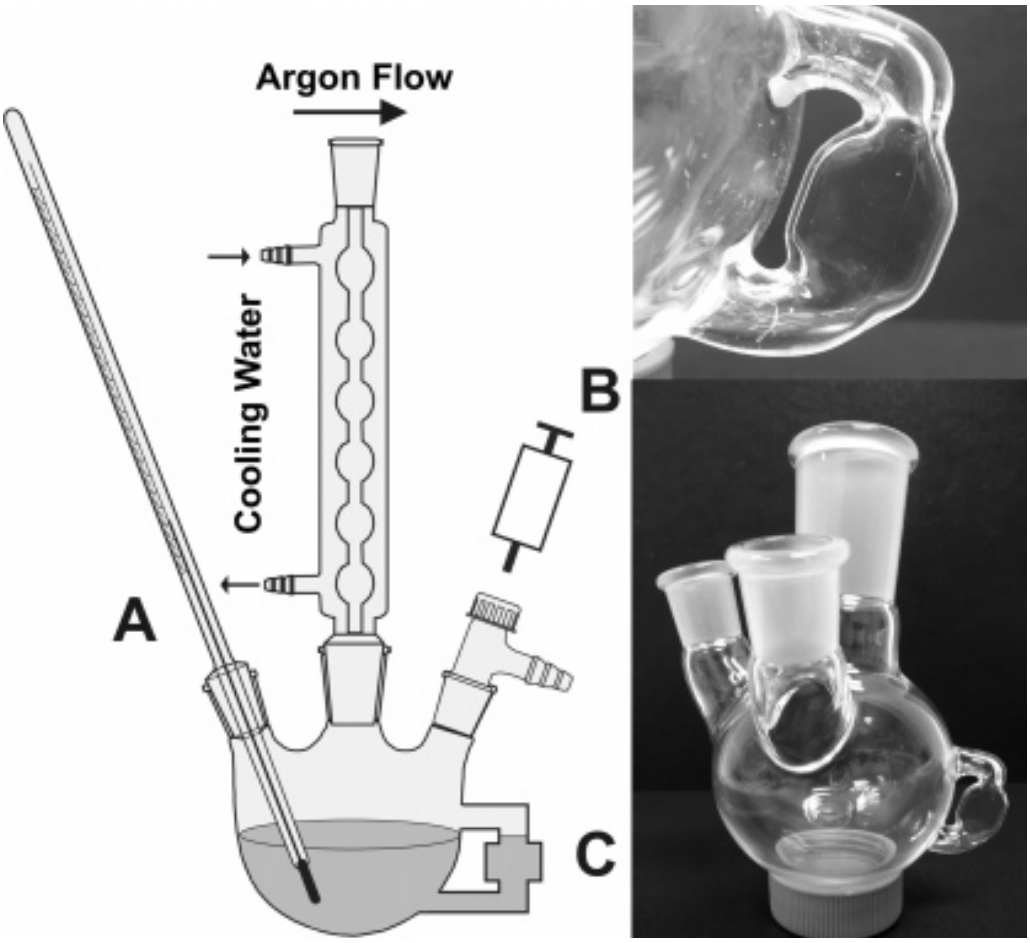

Figure 2.1 Experimental apparatus used in this study to grow CdTe QDs. The band gap of the CdTe QDs is continuously monitored by UV-vis absorption spectroscopy; A: temperature probe connected to the temperature controller; B: injection port; C: glass port to probe absorption spectrum of QDs.

The synthesis of the CdTe QDs is carried out in the setup shown in Figure 2.1. The temperature of the reaction is continuously monitored and recorded (Figure 2.1 A). The precursor molecules are injected through a port sealed with a teflon septum (Figure 2.1 C). The UV-VIS spectra are continuously monitored by using a fiber optic spectrometer during the synthesis via a small cuvette attached to the reaction vessel (Figure 2.1 B). The path length of the cuvette is optimized to achieve fast circulation of the reaction mixture and optimal optical

density from 0.5 mm up to 3 mm. The optical path lengths of the cuvette used in the data presented here are taken with the synthetic setup with the 1 mm path length cuvette. The estimated volume of the cuvette is about 200 times smaller than the total volume of the reaction mixture; therefore the temperature gradient in the reaction is negligible. The synthesis is carried out in moisture- and oxygen-free environment by purging the experimental setup with argon. In order to prepare the Cd precursor, a mixture of CdO (1 mmol) and HPA (5 mmol) is heated to approximately 300 ^{0}C to obtain a clear solution in a three-neck flask. The reaction mixture is cooled and kept under argon for approximately 24 hours. Then, HDA (8.5 g) and TOPO (8.5 g) are added, the temperature of the reaction vessel is increased to 200 ^{0}C, and homogeneous, optically clear solution is obtained. The injection temperature of TOPTe (0.052 M) is varied between 240-270 °C. After injection, the temperature of hot solution drops approximately 40 °C. Depending on the HDA/TOPO ratio, the injection temperature is limited to approximately 240 °C, because at lower temperature the solution may become turbid. At different stages of the synthesis, aliquots are taken out to determine various sized QDs while monitoring the UV-VIS spectrum simultaneously. The CdTe QDs react with atmospheric water and/or oxygen in a few weeks timescale so the optical measurements are carried out immediately after synthesis. As purification, the solution is washed several times with anhydrous methanol. The precipitate is isolated by centrifugation, dried in a vacuum oven at room temperature. After removing the solvents, the precipitate is dissolved in anhydrous toluene.

The HRTEM is performed using a JEOL JEM2010 instrument operating at 200 kV and equipped with a LaB_6 electron source. TEM images are recorded using a 1 k x1 k Gatan Image Filter camera.

Results and the Discussion

The in situ absorption spectra of the CdTe QDs at different growth stages in the synthesis are shown in Figure 2.2a. The QDs are grown in 50/50% HDA/ TOPO solvent mixture. The mixture is heated to 240 °C and the TOPTe solution is injected. The initial flat line indicates the absorption spectrum before the injection of the TOPTe solution into the hot TOPO/HDA mixture. Upon injection, the temperature of the solution drops approximately 40 °C. The temperature profile of the synthesis is also shown in Figure 2.2b. The sharp drop in the temperature is a clear indication of the fast injection for efficient nucleation. The complete injection of the TOPTe takes approximately 10 s. The arrows specify when the spectra are taken during the synthesis. After injection, the spectra develop sharp absorption features. The position of the shorter absorption peaks does not seem to shift to the red as expected from traditional QD growth, but the absorption peaks to the red appear to grow on the expense of the absorption peaks to the blue. The absorption peaks seemed to be less pronounced in the red part of the spectra compared to the absorption peaks to the blue. Figure 2.2c presents generally observed absorption spectra of CdTe NPs with different reaction conditions (higher Cd concentration than the Te concentration) than the Figure 2.2a. The figure illustrates how different the observed multiple peaks in Figure 2.2a than the generally observed mechanism of QD formation. After formation of the first excitonic peak, the NPs grow and form larger particles (Figure 2.2c). In Figure 2.2a different growth of NPs with multiple peaks is observed.

a)

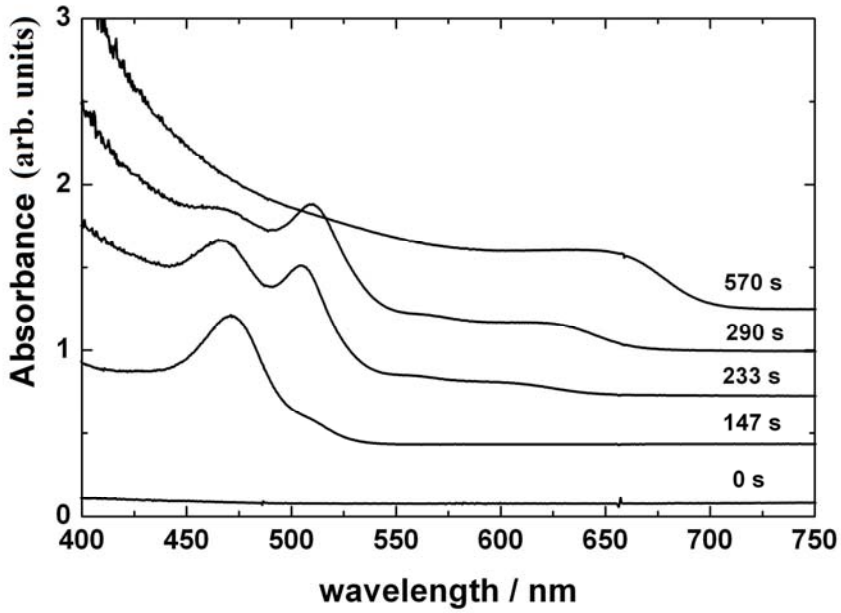
Absorbance (arb. units)
wavelength / nm
570 s
290 s
233 s
147 s
0 s

b)

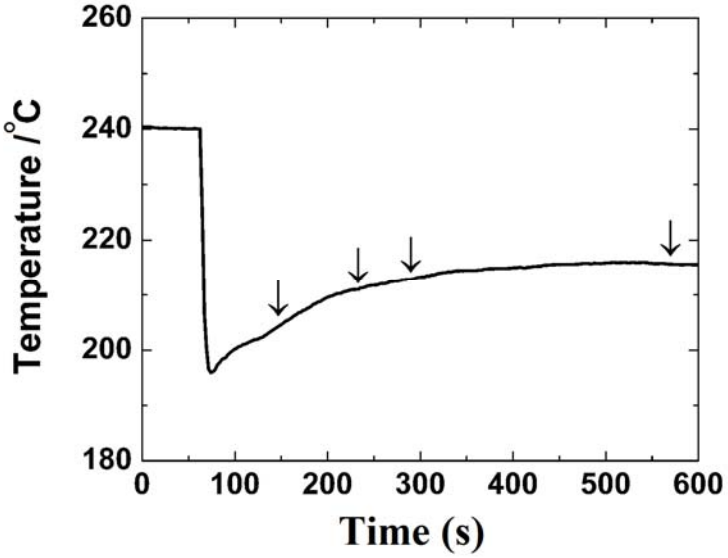
Temperature /°C
Time (s)

c)

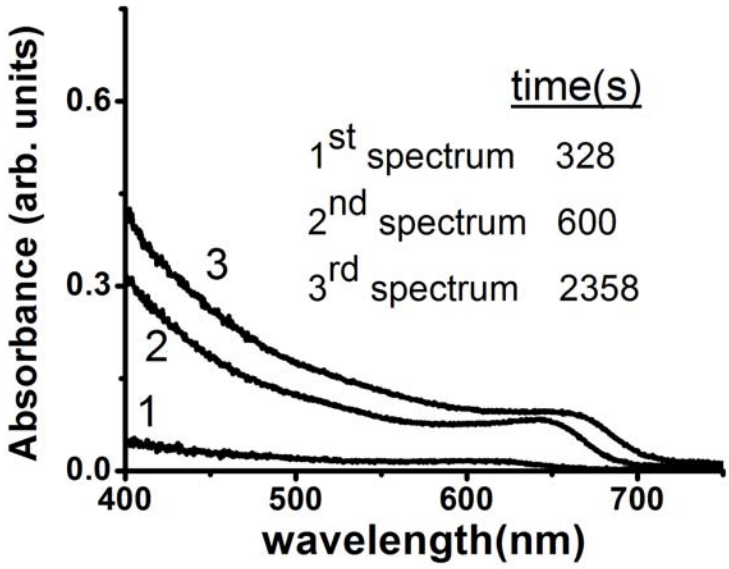

Figure 2.2 (a) In situ absorption spectra of the QDs taken at various times during CdTe QD growth in 50/50% HDA/TOPO coordinating solvent mixture. (b) Time evolution of the temperature during the CdTe QD synthesis shown in (a). Arrows indicate the various times when samples are taken; *t* = 0 corresponds to the injection time. (c) General growth mechanism observed for the CdTe QDs.

There are several absorption peaks identified at 470, 505, 557 and 606 nm. In order to better observe the kinetics of the species associated with the peaks, the peak positions are plotted as a function of time in Figure 2.3a. The first and second peak positions clearly indicate a maximum. The QDs associated with the other peak positions are expected to have higher excitonic absorption, which does not allow obtaining the kinetic curves clearly. The curve shows that two species at 470 and 505 nm are intermediates, which are indicated by their maxima present in Figure 2.3a. The 505 nm absorption peak seems to show a delayed growth. Also, this

latter absorption peak seems to grow as the 470 nm peak is diminishing. In Figure 2.3b, the evolution of the absorption peak positions modified by subtraction the data obtained for the next absorption peak at longer wavelength. This procedure enhances the visibility of the kinetic behavior of the larger CdTe QDs by correcting for the error caused by the higher excitonic transitions from subsequent sizes of QDs. The method does not yield the clear evolution of the absorption data, because of the unequal absorption strength of the higher excitonic peaks relative to the first excitonic peak. Figure 2.3b presents a less sharp peak at 557 nm is also an intermediate crossing a maximum at around 300 s after injection.

a)

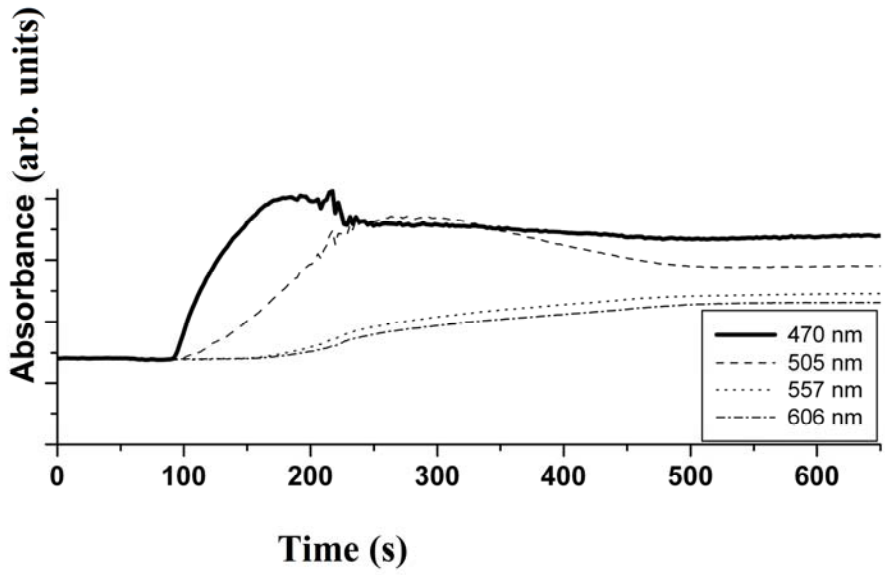

b)

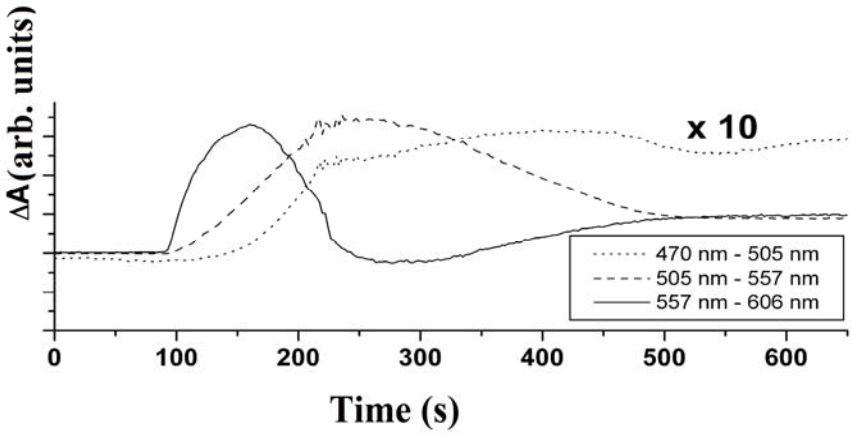

c)

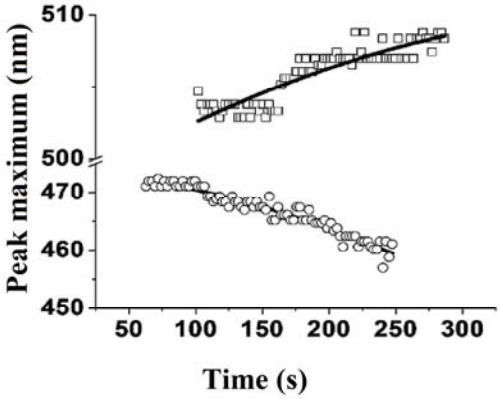

Figure 2.3 (a) Time evolution of the absorption peaks indicated in Figure 2.2a. (b) For better visibility of the kinetics of the individual absorption peaks, the time evolution of the next absorption peak at longer wavelength is subtracted from the peak monitored as indicated in the figure. The absorption peaks at 470, 505, and 557 nm cross a maximum at 100, 200, and 350 s. *t* = 0 corresponds to the injection time. (c) The peak maxima shift of two distinctly observed peaks (~470 and ~505 nm) as a function of the reaction time. The shifts are not large enough to cause a significant change in the observed kinetics.

The high temperature samples are cooled down to a temperature above the melting point of the solvent mixture (approximately 50 °C). The data for the four are shown in Figure 2.4 a-d respectively. The spectra observed during the in situ experiments are sharpened and shifted to the blue approximately 30 nm. This shift is expected due to the change in the relative phonon populations at lower temperature. In addition to the sharper features in Figure 2.4a a new absorption peak appears, which can be either assigned to a higher excitation transition or a smaller cluster. In the figure, the structured fluorescence emission and absorption spectrum show a feature at around 425 nm. Based on previous observation this can be assigned to smaller magic-sized nanoclusters, as well.[12] However, no evidence is found in the TEM images for clusters that small in size, which may be the result of their low crystallinity and low contrast in HRTEM images. In addition to the 425 nm absorption peak, a shoulder is identified at 501 nm in Figure 2.4.b and c, which may be also as a result of a different sized CdTe QD not identifiable from the high temperature absorption data. The reason of not observing the generally observed absorption and emission peaks are attributed to the inhomogeneous broadening, internal and the surface defects. The observed particles are not spherical, that is the reason why the emission spectra are very low and they most probably the Raman lines.

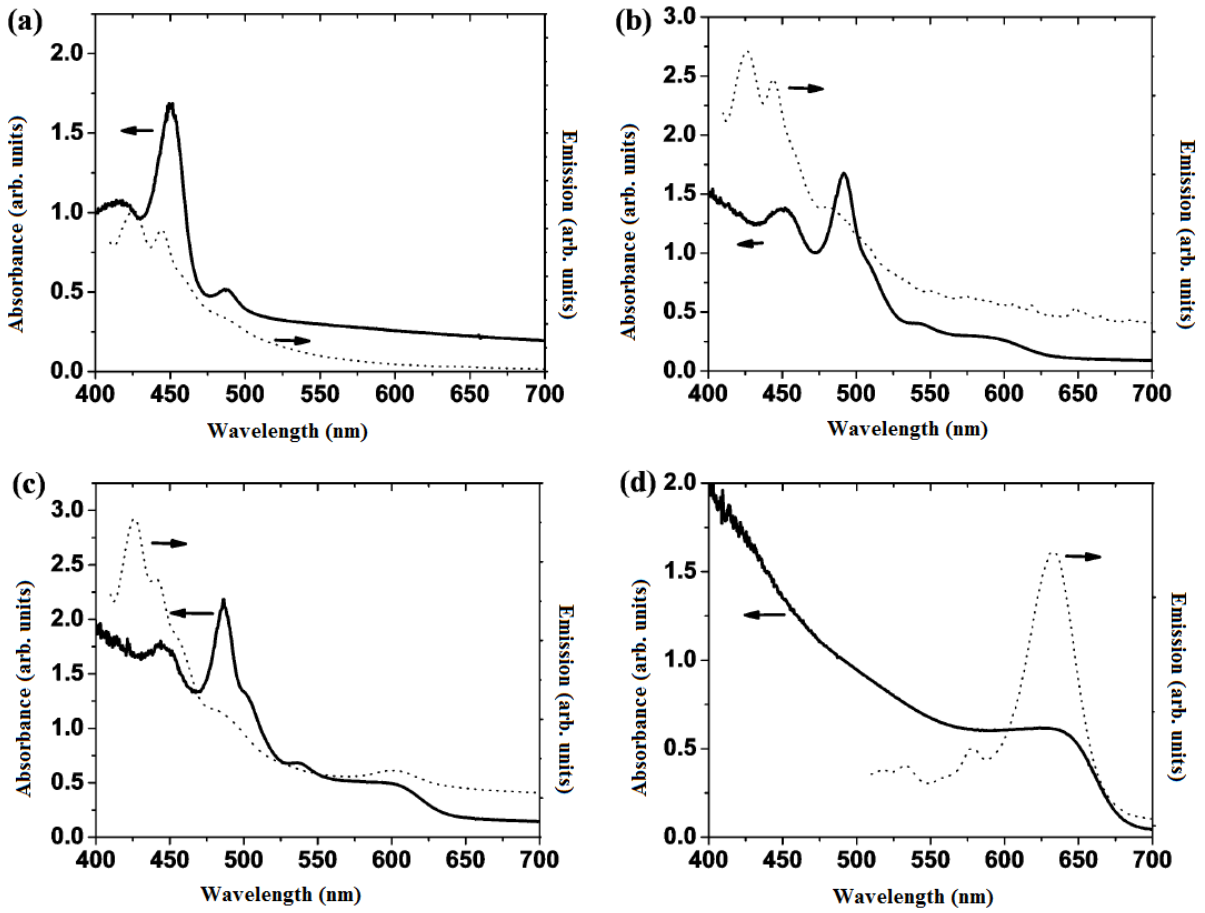

Figure 2.4 (a-d) Absorption and fluorescence spectra of the samples taken during the CdTe QD synthesis as indicated in Figure 2.2a, b. The excitation wavelengths of the fluorescence spectra in Figure 2.2a-c are 400 nm. The excitation wavelength of the fluorescence in Figure 2.2d is 500 nm. All the samples are washed by methanol several times.

Some representative TEM images of the CdTe QD samples are shown in Figure. 2.5. The absorption data are taken for the same samples above. The images show increasing sizes of CdTe QDs as the reaction proceeds. To extract the average size and size distributions, the images are analyzed. The smallest sizes are observed in the first sample. As expected, based

on the absorption spectra, the average size and size distribution of the first sample is 1.9±0.3 nm. The subsequent images show nanoparticles with sizes of 2.8±0.3 nm, 2.8±0.6 nm and 4.4±0.8 nm, respectively. The average radius becomes greater and, subsequently, the size distribution increases as well. The size distribution does not seem to be Gaussian, but rather the sizes seem to concentrate at some distinct sizes. This trend is most obvious and easily observed in fraction 4, where two distinctly different kinds of nanoparticles are visible. Besides the 4.4 nm size, a set of CdTe QDs are also observed with an average size of 7.5±0.5 nm.

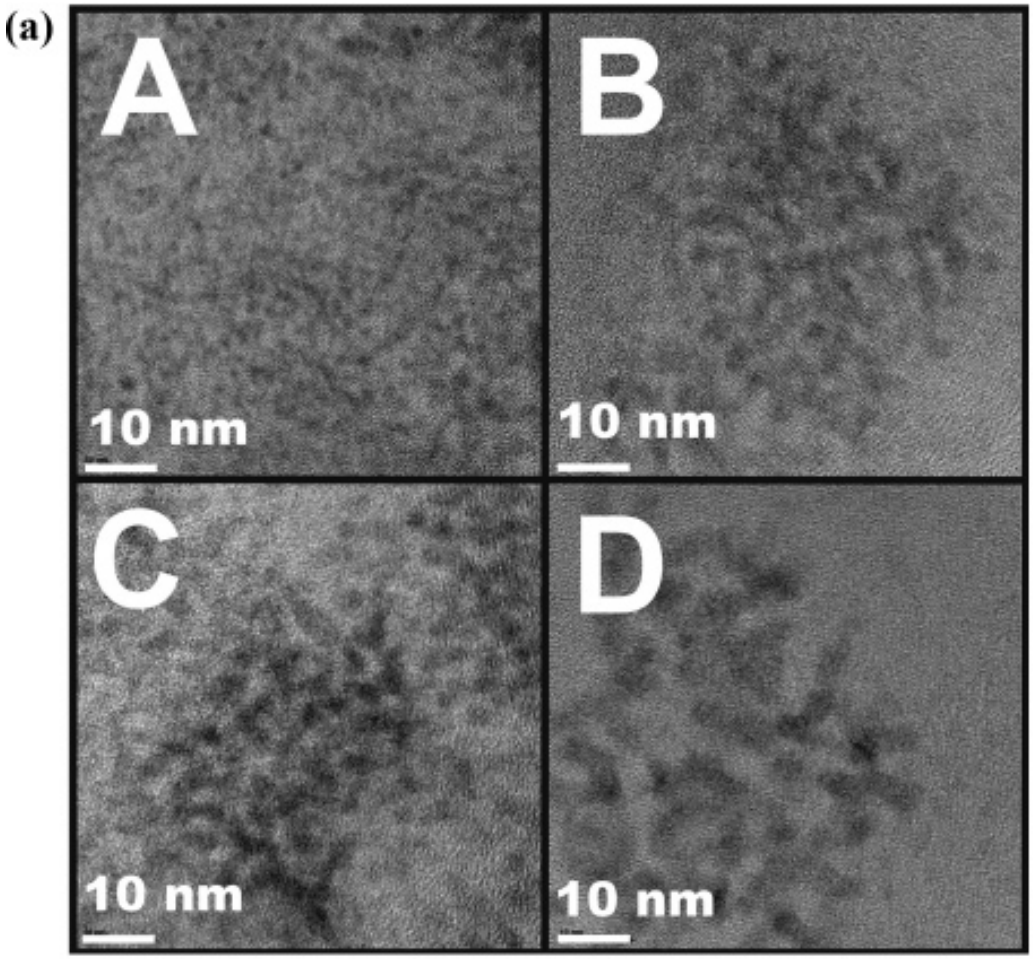

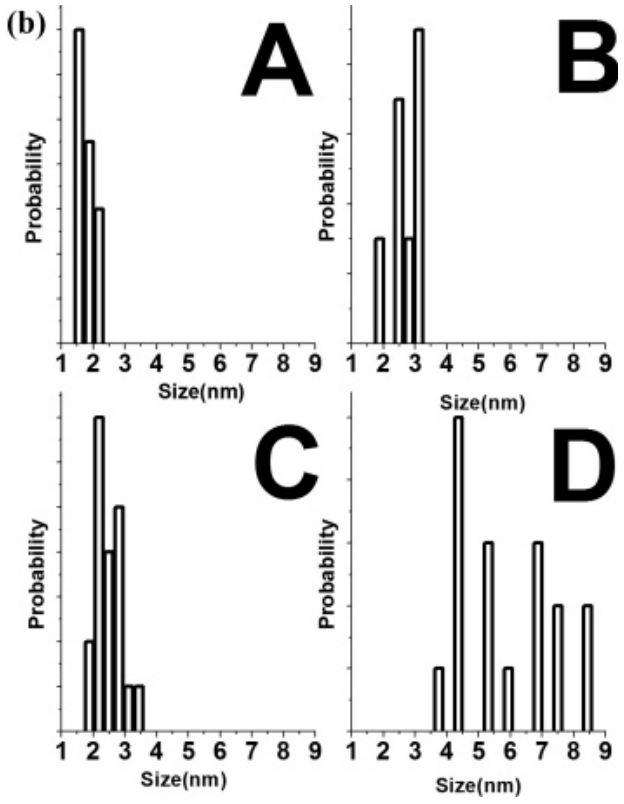

Figure 2.5 (a) HRTEM images of the fractions extracted at A: 85 s, B: 171 s, C: 228 s, and D: 508 s of the synthesis process. Corresponding absorption spectra of these fractions are shown in Figure 2.2a and the extraction times are indicated by arrows in Figure 2.2b. (b) Histograms of the QDs shown in (a)

For fractions 3 and 4, representative HRTEM images of the QDs are shown in Figure 2.6 a-c and Figure 2.6 d-f, respectively. Most of the nanoparticles reveal the cubic zinc blende (ZB) structure. However, many of the nanoparticles, especially the ones from fraction 4, exhibit nanotwinning and/or stacking faults (SFs). Moreover, some of the nanoparticles have partially ZB and partially hexagonal wurtzite (W) phase, like the one shown in Figure 2.6f.

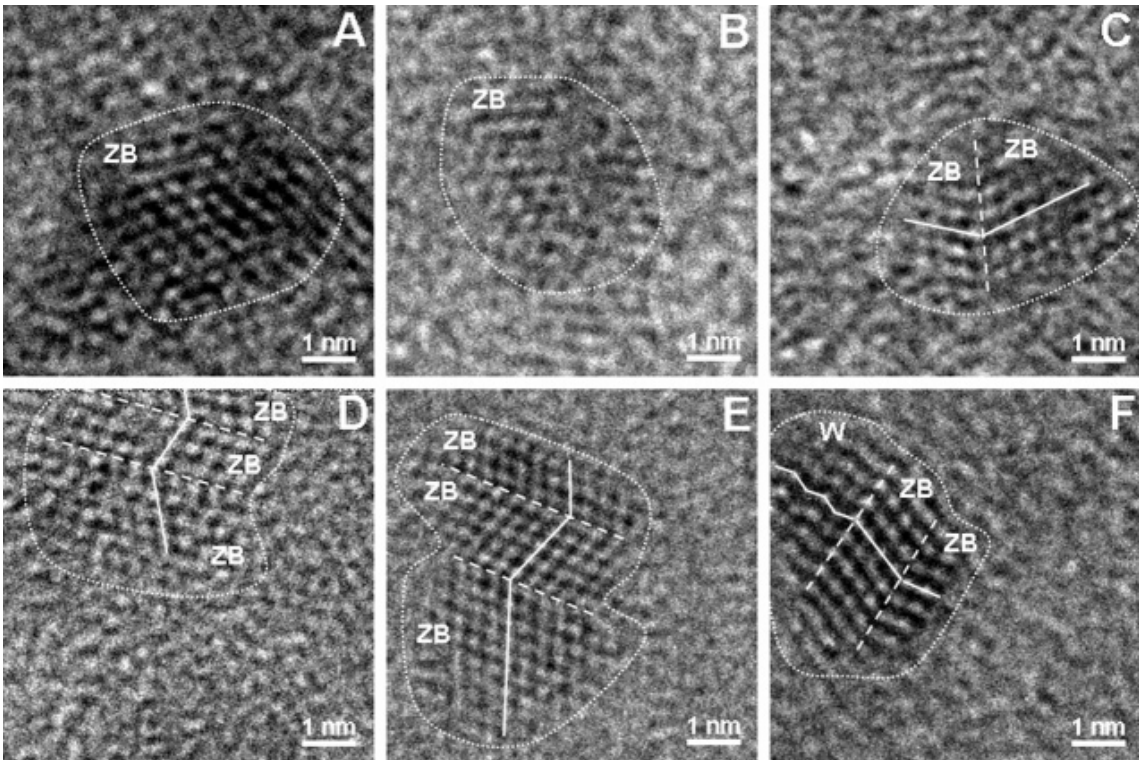

Figure 2.6 Representative HRTEM images of nanoparticles from samples 3 (A-C) and 4 (D-F). Approximate borders of the particles are marked using dotted lines. Twinning planes and/or stacking faults are indicated. Notice that the nanoparticle shown in (F) consists of twinned ZB as well as of W.

CdTe, similar to other II-VI and III-V compound semiconductors, can exist in either the cubic zinc blende or hexagonal wurtzite crystal structure. In either case, the cation and anion atoms are tetrahedrally coordinated and these two structures differ only by the stacking sequence of the atomic planes. The ZB structure of CdTe can be characterized by the …ABCABC… stacking sequence in the close packed model when viewed along any of the <111> crystallographic direction. Each capital letter in this notation represents a bi-atomic Cd-Te {111} layer. In the case of the W structure, the stacking can be represented by the ...ABABAB… sequence when the crystal is viewed along the <0001>, *e.g.* along the direction equivalent to the

<111> in the cubic system. There are two intrinsic (I_1 and I_2) and one extrinsic (E) types of stacking faults (SFs) in the W structure.[13] Using stacking sequence notation, they can be represented as …AB**ABC**BCB…, …AB**ABCA**CA… and …AB**ABCAB**AB…, respectively. In each case, a SF is an equivalent of local cubic stacking, as indicated. Similarly, SFs in the ZB structure are the equivalent of local hexagonal stacking.

Under normal temperature and pressure conditions, the ZB structure is a stable, energetically preferable phase of bulk CdTe.[14] However, at the nanoscale, the relative phase stability of ZB and W structures can be influenced by the nanoparticle size and surface environment. Thus, when the growth substantially reduces overall surface energy, nanoparticles can form in a phase that is unstable in the bulk. This is especially true when the total energy difference between the two phases is relatively small. In such a case, an easy switching between the two phases, for instance in the form of frequent SF formation, can also occur. Therefore, frequent formation of SFs revealed by the HRTEM data is consistent with a relatively small value (0.009 ±0.001 J/m^2) of SF energy (which is closely related to the free energy difference between ZB and W phase) in CdTe.[15-17] Similar behavior, *e.g.* an easy phase switching between the two phases has also been reported in the case of other compounds with small SF energy, such as ZnS[18,19] or CdS.[20]

a)

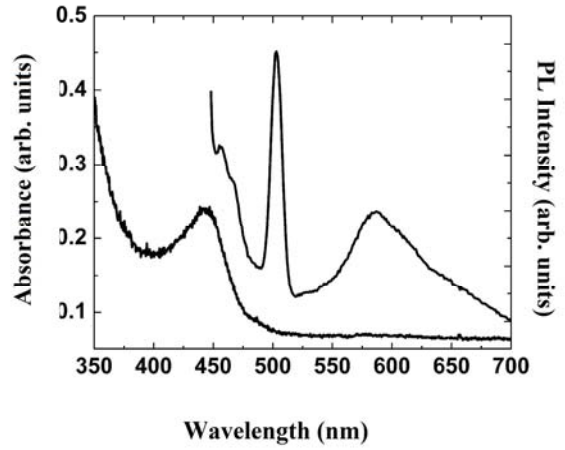

b)

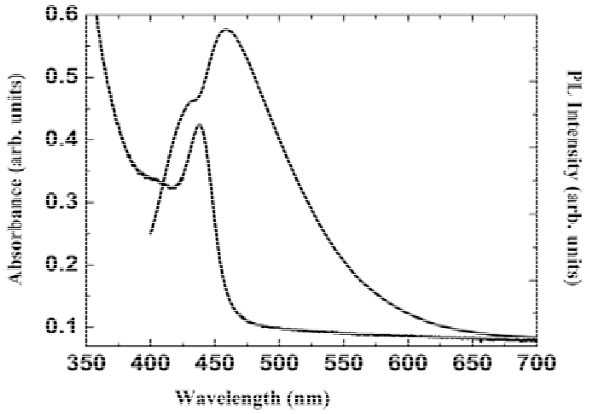

Figure 2.7 (a) Absorption and fluorescence spectra of the purified smallest-sized CdTe QDs in toluene. (b) Absorption and fluorescence spectra of the unpurified smallest-sized CdTe QDs in methanol. The excitation wavelengths of the fluorescence spectra are 437 nm for Figure 2.7a and 390 nm for Figure 2.7b. The unpurified absorption spectrum of the sample is represented by a dashed line in both parts (a) and (b) of Figure 2.7.

Finally, a synthesis is carried out to isolate the magic-sized QDs. The synthesis is completed using exactly the same procedure described above, except the reaction is quenched by addition of large amount of TOP when the first peak is developed. The QDs are purified using the previous method by adding methanol to the freshly prepared solution. It is observed that both the methanol and the toluene phase indicate color, which is assigned to CdTe nanoparticles. The toluene phase is easily purified. Low resolution TEM images and electron diffraction are taken and are in agreement with the previous assignments. The QDs in the toluene phase are approximately 1.8±0.5 nm in size and have the zinc blende crystal structure. The absorption and PL spectrum of the toluene phase are shown in Figure 2.7a. At 390 nm excitation, the fluorescence quantum yield of the solution is 0.16%, which is comparable to the background fluorescence of the solvent used in the experiments. The methanol phase is used without purification. The amount of methanol phase QDs varies from synthesis to synthesis and precipitation of QDs can be observed over time. The absorption and PL spectrum of the methanol phase nanoparticles are shown in Figure 2.7b. The fluorescence of the CdTe QDs in the methanol phase extends from approximately 400 nm to 650 nm. The fluorescence quantum yield of the methanol phase is approximately 4%. There is some noticeable difference between the two phases. The absorption spectrum of the toluene phase seems to be much broader and slightly shifted to the red, which is attributed to the different termination of the QDs. Further studies will be conducted to better understand the difference between the methanol and toluene phase samples. In addition, the methanol phase shows promising application for white light emission due to its very broad emission. Specifically, the observed white light emission seems to cover better the visible range than the white light emission observed for CdSe QDs. The

measured 4% quantum yield seems to be comparable with what is observed for magic-sized CdSe QDs recently reported by Bowers et. al.[2]

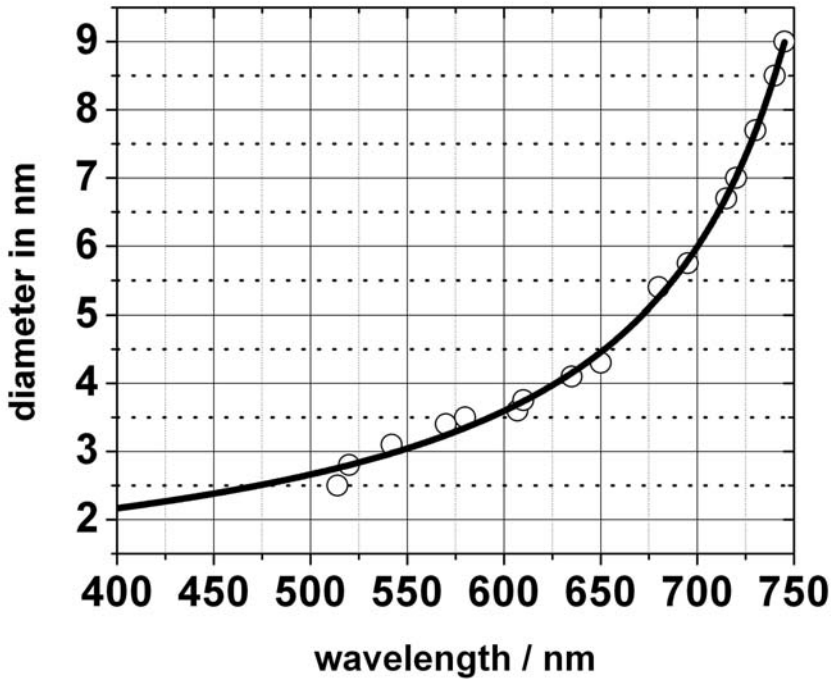

Figure 2.8 Sizing curve of CdTe QDs. The data are taken from the literature as indicated in the text.

To better correlate the observed peaks with sizes, an empirical relationship between the room temperature peak positions and sizes is derived. The size vs. room temperature absorption peak maximum is plotted in Figure 2.8. The data points are derived from the literature observation. The data points are fitted with the function according to equation 2.1. The derived function has no physical meaning, except it is used to be able to extract the predicted sizes of the nanoparticles. The function is extended down to approximately 400 nm. No data points are located in the literature for very small sized CdTe QDs, therefore, the data points below 500 nm on the size curve are extrapolated points.

$$r = \frac{1.38435 - 0.00066\lambda}{1 - 0.00121\lambda} \qquad (2.1)$$

There are three proposed mechanisms of the QD growth under the experimental conditions shown in Figure 2.9. The first mechanism designated by A shows the diffusion controlled growth of the QDs. The mechanism shows that one magic-sized $(CdTe)_n$ QD reacts with (CdTe) monomers resulting in a cluster $(CdTe)_{n+1}$. This growth mechanism forms the basis of the diffusion controlled growth of QDs. According to mechanism A, the nanoparticles may undergo either focusing or defocusing of the particles. At high monomer concentration, the focusing of particles dominates as previously shown. At low monomer concentration the defocusing or Ostwald ripening is the dominating process, which simply means that the large nanoparticles grow on the expense of the small ones. From the data presented earlier, there is a large separation between sizes, which makes this mechanism unlikely.

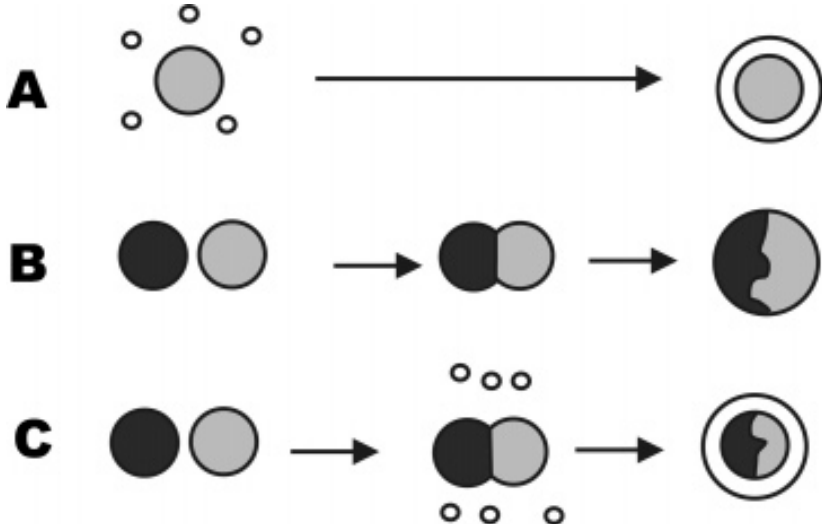

Figure 2.9 Another sample figure suggested scheme of the growth of the magic-sized CdTe QD; A: monomer assisted growth; B: coalescence of magic-sized CdTe QDs; C: monomer and coalescence assisted growth of the CdTe QDs.

A more reasonable mechanism for growth of the magic size CdTe QDs is the aggregation of QDs, which may or may not involve the addition of monomers units (Figure 2.9 B and C). Mechanism B omits involvement of the monomer units so it is only able to capture the aggregation part of the dynamics. Evidence of the aggregation of magic-sized QDs in the crystal structure of the HRTEM images of the aggregated CdTe can be seen in Figure 2.6. The regions defined by the twinning planes and stacking faults seem to correlate well with the isolated magic-sized CdTe QD in Figure 2.7. If the aggregation is the primary mechanism for the QD growth under the experimental conditions, then it is expected that the volume of the resulting QD would be multiple of the original QD. Since multiple peaks can be observed, simple calculation has been done based on the size derived from the absorption peak positions. The observed room temperature peak positions for the fractions taken are 410, 449, 491, 501, 539 and 588 nm respectively. The calculated sizes based on equation 2.1 are 2.26 (6.00 nm_3), 2.37 (7.0), 2.60 (9.2 nm_3), 2.67 (10.0 nm^3), 2.95 (13.40 nm^3) and 3.44 (21.3 nm^3) nm in diameter, respectively. Since the sizing curve may not be accurate for very small QDs, a similar calculation can be done based on the observed sizes from the HRTEM images for the very small sizes. The 1.9 nm CdTe QDs has a volume of 3.6 nm^3. The volume of the magic size CdTe QD is four or six times larger than the magic-sized CdTe QDs, which seems to correlate well with the QDs with at 539 nm and 588 nm peak positions.

Table 2.1 Some Parameters of CdTe QDs

peak positions (nm)	410	449	491	501	539	588
QD diameter (nm)	2.26	2.37	2.6	2.67	2.95	3.44
QD volume (nm3)	6.00	7.0	9.2	10.0	13.40	21.3
$V_{\text{QDaggregate}}/V_{\text{magic-sized QDs}}$	1.66	1.94	2.55	2.77	3.72	5.91

Mechanism C in Figure 2.9 combines the two previous mechanisms, where both aggregation (mechanism B) and focusing defocusing (mechanism A) plays an important role. The broad peaks at the later stage indicate that Ostwald ripping plays a role. Similarly, at higher monomer concentration the role of the focusing effects can not be excluded. If the experiments carried out with approximately ten times higher initial Cd concentration, the results show that similar aggregation dynamics, but the number of peaks observed is fewer and the remaining peaks show focusing with time. The conclusion is that both aggregation and focusing-defocusing have roles under the experimental conditions and the aggregation mechanism competes with the usual monomer-induced growth mechanism. Manipulating the monomer concentration, conditions can be found where one dominates over the other.

Based on the data above, the quantized growth of the CdTe QDs clearly involves the thermodynamic control QD synthesis. The formation of magic-sized QDs can be the result of intrinsic stability of the QDs or the QD and the ligand at a specific size. Magic-sized CdTe QDs can only be observed at some specific solvent systems, which suggests that the ligand is the key in this process. Several straight chain amines/TOPO mixtures (not presented here) have been investigated as a solvent and the peak positions does not seem to be affected only the rate and sharpness of the peaks are changing. However the HPA used in this synthesis for the complexion of CdO precursor may also act as a ligand for the magic-sized CdTe QD formation. Experiments have been carried out to remove the HPA, in which the quantized growth of the CdTe QDs is not observed. Other experiments have been carried out to switch the CdO precursor with Me_2Cd, which resulted in quantized growth similar to the CdO/HPA precursor system.

An example of the aggregation of CdTe nanoparticles is observed by Tang et. al.[21] After the removal of surface capping reagents, the nanoparticles formed linear aggregates at room temperature, which are subsequently recrystallized from their original zinc blende into wurtzite nanowires. In this reaction system, the HPA is a strongly binding surface capping, which makes its removal rather difficult. However, the reaction temperature is sufficiently high, providing the necessary energy to cross the activation energy for aggregation of individual CdTe nanoparticles. Similarly to the example mentioned above, partial recrystallization of the CdTe aggregates is observed experimentally. As Tang points out, the driving force of the aggregation is most likely the existence of the dipole-dipole interaction between particles to from chain like aggregates. Zinc blende CdTe does not have intrinsic permanent dipole; however, the presence of defects can produce strong permanent dipoles as it has been shown by theoretical calculations.[22] The calculations are based on semi empirical PM3, showing the existence of 50-100D permanent dipole. Also, the presence of other dipoles, such as water, strongly influences the directionality of the dipole. It is assumed that the aggregation dynamic presented under the experimental conditions are driven by the presence of permanent dipoles in the CdTe nanoparticles. Some directionality in the CdTe nanoparticles are observed in agreement with the observation by Tang et. al.

Conclusions

This work reports the observation of quantized growth of CdTe QDs at relatively high reaction temperatures (above 200 °C). Magic-sized CdTe nanoparticles are observed by in situ absorption spectroscopy during the crystal growth. The magic-sized nanoparticles undergo aggregation leading to larger particles. The high stability of the magic-sized QDs is due to the presence of HPA. The result suggests that under low monomer conditions quantized growth is important in

the presence of strongly binding surfactant molecules in the case of CdTe nanoparticle growth. In agreement with previous experimental and theoretical data, the aggregation is assumed to proceed because of the existence of permanent dipole in the zinc belende CdTe nanoparticles. The smallest magic-sized QDs are separated, which exhibit interesting optical properties sensitive to their surface chemistry.

References

1. Peng, Z. A.; Peng, X. G. *Journal of the American Chemical Society* **2002**, *124*, 3343.

2. Bowers, M. J.; McBride, J. R.; Rosenthal, S. J. *Journal of the American Chemical Society* **2005**, *127*, 15378.

3. Murray, C. B.; Norris, D. J.; Bawendi, M. G. *Journal of the American Chemical Society* **1993**, *115*, 8706.

4. Talapin, D. V.; Rogach, A. L.; Haase, M.; Weller, H. *Journal of Physical Chemistry B* **2001**, *105*, 12278.

5. Boyen, H. G.; Kastle, G.; Weigl, F.; Koslowski, B.; Dietrich, C.; Ziemann, P.; Spatz, J. P.; Riethmuller, S.; Hartmann, C.; Moller, M.; Schmid, G.; Garnier, M. G.; Oelhafen, P. *Science* **2002**, *297*, 1533.

6. Stoeva, S.; Klabunde, K. J.; Sorensen, C. M.; Dragieva, I. *Journal of the American Chemical Society* **2002**, *124*, 2305.

7. Leff, D. V.; Ohara, P. C.; Heath, J. R.; Gelbart, W. M. *Journal of Physical Chemistry* **1995**, *99*, 7036.

8. Platschek, V.; Schmidt, T.; Lerch, M.; Muller, G.; Spanhel, L.; Emmerling, A.; Fricke, J.; Foitzik, A. H.; Langer, E. *Berichte Der Bunsen-Gesellschaft- Physical Chemistry Chemical Physics* **1998**, *102*, 85.

9. Rogach, A. L.; Katsikas, L.; Kornowski, A.; Su, D.; Eychmuller, A.; Weller, H. *Berichte Der Bunsen-Gesellschaft-Physical Chemistry Chemical Physics* **1997**, *101*, 1668.

10. Rogach, A. L.; Kornowski, A.; Gao, M. Y.; Eychmuller, A.; Weller, H. *Journal of Physical Chemistry B* **1999**, *103*, 3065.

11. Spanhel, L.; Anderson, M. A. *Journal of the American Chemical Society* **1991**, *113*, 2826.

12. Wuister, S. F.; van Driel, F.; Meijerink, A. *Physical Chemistry Chemical Physics* **2003**, *5*, 1253.

13. Hull, D. *Introduction to dislocations*, 3rd ed.; Pergamon Press: Oxford, New York, Beijing, Frankfurt, Sao Paulo, Sydney, Tokyo, Toronto, 1984.

14. Takeuchi, S.; Suzuki, K. *Physica Status Solidi a-Applied Research* **1999**, *171*, 99.

15. Hall, E. L.; Vandersande, J. B. *Philosophical Magazine a-Physics of Condensed Matter Structure Defects and Mechanical Properties* **1978**, *37*, 137.

16. Lu, G.; Cockayne, D. J. H. *Physica B & C* **1983**, *116*, 646.

17. Lu, G.; Cockayne, D. J. H. *Philosophical Magazine a-Physics of Condensed Matter Structure Defects and Mechanical Properties* **1986**, *53*, 307.

18. Cozzoli, P. D.; Manna, L.; Curri, M. L.; Kudera, S.; Giannini, C.; Striccoli, M.; Agostiano, A. *Chemistry of Materials* **2005**, *17*, 1296.

19. Zhang, H. Z.; Chen, B.; Gilbert, B.; Banfield, J. F. *Journal of Materials Chemistry* **2006**, *16*, 249.

20. Jun, Y. W.; Lee, S. M.; Kang, N. J.; Cheon, J. *Journal of the American Chemical Society* **2001**, *123*, 5150.

21. Tang, Z. Y.; Kotov, N. A.; Giersig, M. *Science* **2002**, *297*, 237.18

22. Shanbhag, S.; Kotov, N. A. *Journal of Physical Chemistry B* **2006**, *110*, 12211.

CHAPTER 3 - Effect of Cd/Te Ratio on the Formation of CdTe Magic-Sized Quantum Dots during Aggregation

Introduction

Controlling the growth of semiconductor nanoparticles (NPs) is important for technology to produce materials with well-defined properties.[1] One of the main research efforts of the nanoparticle scientific community has been to create highly crystalline nanomaterials.[2] From this point of view, the aggregation of nanoparticles is an undesirable mechanism for the formation of nanoparticles because it leads to the formation of crystal defects. However, if the aggregation of nanoparticles can be controlled,[3] then the solution-phase self-assembly of materials can be better understood and utilized to create novel materials with well-defined defects.

The growth of nanoparticles can be thought of as a simple crystal growth problem. During crystal growth, the first step is the formation of nuclei from a supersaturated solution. Supersaturation can be achieved by changing the thermodynamic properties of the solution (1) by the fast decomposition of precursor molecules, (2) by decrease the temperature, or (3) by a combination of the two. The initial formation of small nuclei is followed by the slow growth of nanoparticles separated from the nucleation step. According to the accepted model, the nanoparticle growth is mainly controlled by the Gibbs-Thomson effect. The Gibbs-Thomson effect predicts that the particles with larger curvature exhibit higher effective monomer solubility, which is mainly responsible for the deviation from the simple crystal growth problem. An elegant numerical method proposed by Talapin et. al.[4] shows that at high monomer concentrations the initial particle size distribution undergoes focusing as observed experimentally by many research groups.[5] The model Ostwald ripening process.[6] The nanoparticle system as a whole is heading toward the thermodynamic minimum by decreasing

the surface area and forming more bulk-like particles with more flat surfaces. The model assumes that particles can get larger only by exchanging monomers with the solution and consequently with each other.

Alternatively, a nanoparticle system can minimize its overall energy by aggregation, when two particles come into close contact and form a new particle with a volume that is the sum of the constituents. There are attractive and repulsive forces involved in the aggregation, which control the observed aggregation kinetics. If repulsive forces dominate the particle-particle interaction, then aggregation does not take place on the time scale of observation. The interactions can have strong van der Waals character, as in the case of the aggregation of GaSe nanodisks.[7] The interaction of GaSe nanodisks is also increased by the larger interaction surfaces, which are absent in the case of spherical nanoparticles. Electrostatic interaction leads to the aggregation of spherical nanoparticles, as can be observed in solutions containing silver and gold nanoparticles.[8,9] When the attractive forces are deliberately tailored by using cross-linking molecules, the aggregation can lead to nanoparticle-based aggregates with novel properties.[10,11]

A specific example of aggregated growth that has attracted some attention is the oriented attachment of semiconductor nanoparticles to form nanowires. In oriented attachment (OA), nanoparticles attach and organize themselves along the same crystallographic axis via directional dipole-dipole interaction. The proposed reason for the OA has been attributed to the presence of a net dipole moment in the crystal.[12,13] Interestingly, the presence of a net dipole is not limited to polar crystals but may be the result of defects.[13] The typical orientation of dipoles is a head-to-tail arrangement when there is significant attraction between particles. As a result of the OA of *n* spherical NPs, nanowires will be formed with a length approximately *n* times the diameter of the nanoparticles. In the literature, there are many examples of the oriented attachment of

nanoparticles, including ZnS,[14] CdTe,[15,12] ZnTe,[16] PbSe,[17] and CdS nanoparticles. In the study of PbSe, nanowires are synthesized, and the attachment of nanoparticles is through identical crystal faces leading to OA. A recent simulation model explains the formation of nanorods from quantum dots due to OA, predicting the length distribution of the nanorods.[14] Although, the examples of oriented attachment leading to nanowire formation are numerous, not all of the nanoparticle aggregation will yield nanowires, especially at higher temperatures when nanowires can collapse. Although the examples of oriented attachment leading to nanowire formation are numerous not all of the nanoparticle aggregation will yield nanowires, especially at higher temperatures when nanowires can collapse.

In one aggregation mechanism, the nanoparticle aggregates may undergo a complete phase transformation and collapse resulting in a "new" particle. Another possibility for the mechanism of aggregation is that the aggregated nanoparticles will form a neck, which accelerates the growth of the nanoparticle aggregate via monomer exchange as observed experimentally during the fusion of nanoparticles into nanowires.[16-19] This later aggregation mechanism will result in particles with volumes larger than the volumes of their original constituents. Therefore, the two mechanisms can be differentiated by experimental methods that can sensitively measure volume change during nanoparticle growth.

There are an increasing number of reports on nanoparticle synthesis showing that multiple sizes of nanoparticles may coexist in solution.[20,21] Our previous report[22] has shown that magic-sized CdTe nanoparticles aggregate in a high-temperature coordinating solvent, which results in variously sized nanoparticle aggregates as a function of time. However, no experimental control is given over the observed aggregation pattern. In fact, varying the solvent composition and temperature over a wide range yielded a very similar aggregation pattern as a

result of the stabilization or destabilization of magic-sized CdTe nanoparticles. To reproduce the observed aggregation pattern, a simple simulation has been developed to include both monomer exchange and the aggregation-driven growth of the nanoparticles. The simulation shows good agreement with the experiment, considering the qualitative nature of the approach.

Experimental Section

Chemicals: Tellurium powder (99.999%), CdO (99.999%), phenylphosphonic acid (99%), trioctylphosphine (TOP, 97%), trioctylphosphine oxide (TOPO, 90%), 1-hexadecylamine (HDA, 90%), anhydrous methanol (99.8%), anhydrous toluene (99.8%), *n*-hexylphosphonic acid (HPA, 100%), octadecylamine (ODA, 98%), dodecylamine (DDA, +98%), stearic acid (purified), dimethylcadmium (97%) were used. TOPO, TOP, and HDA were purified by vacuum distillation.

Synthesis of CdTe Nanoparticles: The synthesis method and the experimental setup are identical to those given in a previous publication.[22] The experimental setup allows us to obtain in situ absorption spectra at the synthesis temperature. The reaction conditions for preparing CdTe nanoparticles used in this experiment are as follows. A mixture of CdO (1 mmol) and HPA (5 mmol) is heated to approximately 300 ^{0}C to obtain a clear solution in a three-necked flask. The reaction mixture is cooled and kept under argon for approximately 24 h. Hexadecyl amine (8.5 g) and trioctyl phosphine oxide (TOP, 8.5 g) are added, and the temperature of the reaction vessel is increased to 200 ^{0}C until a homogeneous, optically clear solution is obtained. A solution (10 mL) containing tellurium (0.052 M) is injected to initiate the growth of the nanoparticles. The injection temperature is varied between 240 and 270 ^{0}C. After injection, the temperature of the hot solution drops by approximately 40 ^{0}C. At different stages of the synthesis, aliquots are removed to determine variously sized QDs while monitoring the UV-vis spectrum

simultaneously. Cd/Te ratios are also changed, which are given as 1/0.5, 1/1, 1/5, and 1/10. During purification, the solution is washed several times with anhydrous methanol. The precipitate is then isolated by centrifugation and dried in a vacuum oven at room temperature. After the solvents are removed, the precipitate is dissolved in anhydrous toluene.

Results and Discussion

Controlling the self-assembly of quantum dots in solution is important in creating novel structures. A key challenge is to identify important parameters that could potentially manipulate the aggregation of quantum dots. The sequential aggregation of CdTe nanoparticles via the formation of magic-sized QDs has already been reported.[22] Figure 3.1 shows the in situ absorption spectra of CdTe QDs in sequence with different Cd/Te ratios. The spectra show the sequential appearance of relatively sharp peaks at high temperatures. The first sharp absorption peak corresponds to magic-sized nanoparticles appearing in the tellurium-rich reaction mixture at 240 ^{0}C. The kinetics of QD growth in solutions containing different Cd/Te ratios significantly varies. The spectra are taken 70, 152, 238, and 490 s after injection. At 70 s, all of the spectra have different features. In Figure 3.1a (Cd/Te 1:0.5), there is a flat line indicating neither nucleation nor particle growth. In Figure 3.1b, a similar feature can be seen. In Figure 3.1c,d, a sharp peak associated with the magic-sized CdTe QDs already starts forming. A similar trend can be noticed at later times in Figure 3.1a-d. Briefly, the increasing ratio of tellurium accelerates the growth of the CdTe particles. Qualitatively, the amount of absorbance also increases, which indicates that the number density of particles is greater as well. Another key difference among the various ratios of Cd/Te is that Figure 3.1a data corresponding to cadmium-rich conditions does not show the appearance of magic-sized nanoparticles. The absence of magic-sized nanoparticles from the growth solution still does not mean that there is no aggregation of the

quantum dots. In fact, the reduced crystallinity of the cadmium samples from XRD suggests otherwise.

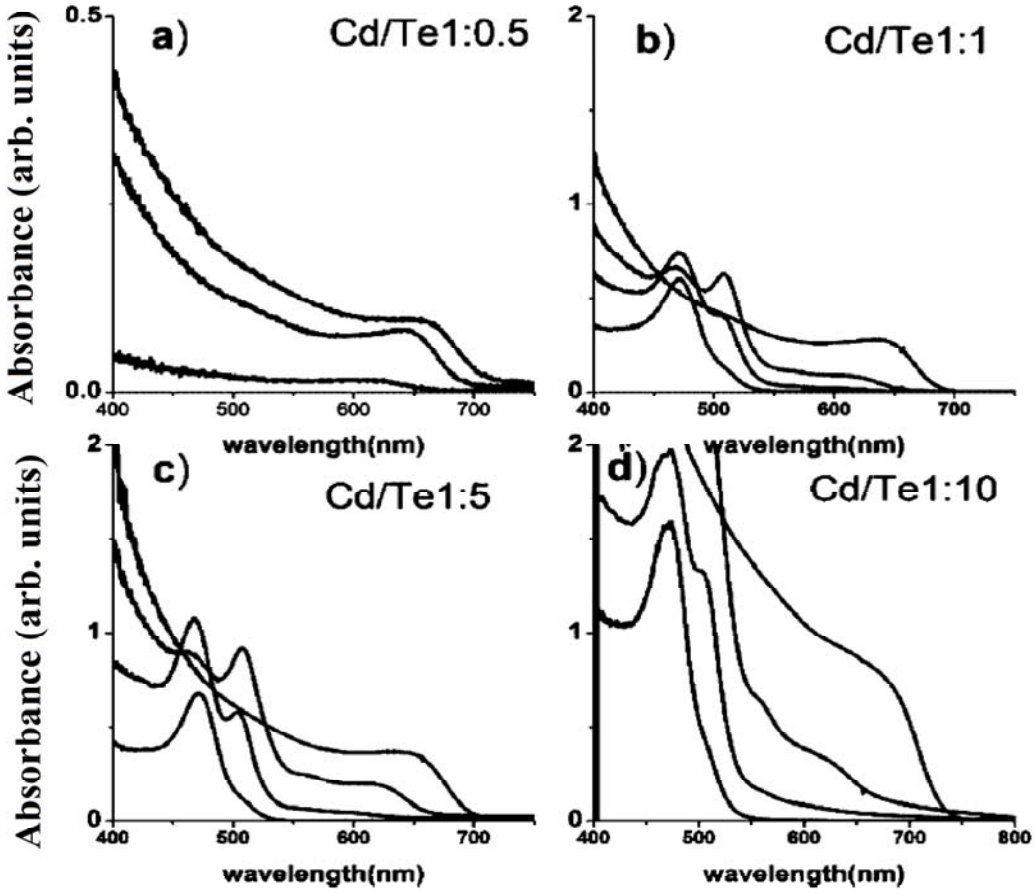

Figure 3.1 Variation of growth kinetics of CdTe nanoparticles with the CdTe ratio. Only the tellurium concentration is changed. The in situ absorption spectra are taken at 240 ^{0}C at the same times after injection (70, 152, 238, and 490 s). For the cadmium-rich condition, the inset shows different times to describe the early-time kinetics better. Notice the appearance of magic-sized nanoparticles for the tellurium-rich conditions.

Figure 3.2 presents the X-ray diffraction patterns of two samples with 1:1 and 1:0.5 Cd/Te ratios. The sample that has a 1:1 Cd/Te ratio has an identical pattern to that of the

tellurium-rich samples; therefore, the XRD from the other samples is omitted. In Figure 3.2a, there are three XRD peaks centered at 2θ angles of 24^0, 40^0, and 47^0. Figure 3.2b only shows one broad XRD peak at 23^0. The tellurium-rich sample in Figure 3.2a indicates a more crystalline structure whereas in Figure 2b the cadmium-rich condition corresponds to a sample that is more amorphous. Although the size analysis of the nanoparticles indicates similar final distributions, the lack of the distinct peak in Figure 3.2 (bottom) and the increased FWHM of the reflection suggest that the crystalline domains in the cadmium-rich samples are smaller. The Debye-Scherer method yields. 3.7 nm±0.3 and 1.1 nm±0.2 domain size of the tellurium- and cadmium-rich samples, respectively. The positions of the peaks match the zinc blende CdTe QDs in Figure 3.2a, but the presence of a (101) peak at 26^0 is an indication of the phase transition from the zinc blende to wurtzite structure, as observed before.[27]

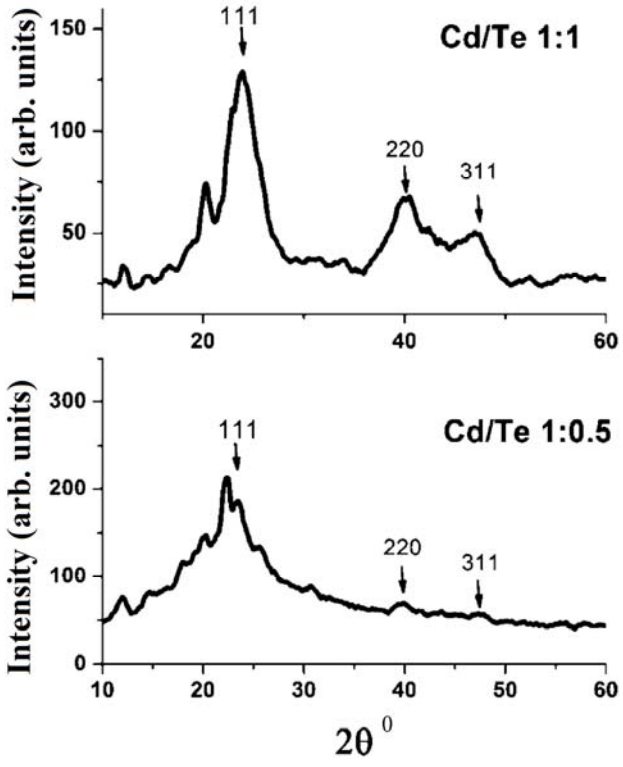

Figure 3.2 XRD pattern of the 1:1 and 1:0.5 Cd/Te initial ratio CdTe nanoparticles.

Figure 3.3 shows the absorption spectra of the very small 1.9 nm CdTe QDs (magic size). To obtain this size, the tellurium-rich reaction is quenched by injecting a large amount of TOP solvent to decrease the reaction temperature. In Figure 3.3, the ratio of Cd/Te in CdTe QDs is 1:5. The QD absorption peak indicates a very narrow size distribution with a spectral full width at half-maximum (FWHM) of 17 nm. The inset is the high resolution transmission electron microscopy (HRTEM) image of the particles. This size is most likely identical to the ones observed by Rockenberger et. al.[23] The observation of a narrow size distribution magic size is very important in these experiments, which makes it possible to extract quantitative information about the aggregation dynamics. Several arguments exist as to why magic-sized quantum dots form. The two important ones are worth mentioning assume thermodynamic reasoning. The realization of magic size can be the result of a closed-shell stable electronic structure.[24] Another reason for the large thermodynamic stability may originate from the delicate balance between the surface and the intrinsic energy of the nanoparticle.[25,26] Under Te-rich conditions, the small particles aggregate and form the larger ones. Various studies on the growth of CdTe nanowires from the oriented attachment of smaller particles suggest that the aggregation is driven by dipole-dipole interactions.[12,32] The small particles have a zinc blende crystal structure, but as they grow, they have the tendency to undergo a phase transition from zinc blende to wurtzite, as shown in the XRD pattern (Figure 3.2 top).[22]

In the next experiment, the CdO precursor is replaced by Me_2Cd. When the same amount of cadmium is used as in the case of the 1:5 Cd/Te ratio, the observed growth kinetics is very similar to the 1:0.5 Cd/Te ratios, which shows that there is a significant difference between the activity of the cadmium precursor and how it affects the growth kinetics. The lack of aggregation growth suggests that if the cadmium concentration is further increased no aggregation should be

observed. Contrary to these expectations, as the cadmium concentration increases, the aggregation pattern returns as shown in Figure 3.4. Interestingly, only two definite sizes are observed, and the growth seems to stop, which is distinctly different from the aggregation mechanism described above. The first size is the same as the magic-sized nanoparticle, and the second observed size is approximately 2.5 ± 1.0 nm from TEM and 2.8 ±0.2 nm on the basis of the sizing curve.[22] Qualitatively, the difference could be the result of the reactivity of the cadmium precursors. Whereas CdO is present in the solution and tellurium is injected, Me_2Cd needs to decompose first to supply the cadmium for the QD growth. In the initial phase of the decomposition, the conditions correspond to the tellurium-rich conditions, but when all the cadmium decomposes, the cadmium-rich condition stops further growth. These results are in agreement with the experimental observation for nanowire growth from oriented attachment. Deng et. al. have found that under cadmium-rich conditions spherical growth is preferred whereas tellurium-rich conditions promote the linear assembly of CdTe nanoparticles.[27] The qualitative explanation of the stopped aggregation could be explained by the change in dipoles in the QDs under the reaction conditions. As will be shown in the simulation part, the presence or lack of a dipole moment in the nanoparticles may influence the rate of aggregation but does not explain the different aggregation patterns. In conclusion, when the conditions are cadmium-rich, no magic-sized nanoparticles are formed, but there the aggregation mechanism seems to be the dominant growth mechanism.[20]

The key question is why there is now magic-size formation under tellurium-rich conditions. The results strongly suggest that the magic-sized nanoparticle formation is driven by thermodynamic control of the system. Thermodynamic control of metal[28] (e.g., digestive ripening of gold nanoparticles in the presence of alkyl thiols) and semiconductor nanoparticles[29]

is well documented in the literature. Briefly, the overall chemical potential (μ_{tot}) of the systems can be described by the following equation:

$$\mu_{tot} = \mu_{surf} + \mu_{bind} \quad (3.1)$$

The first term describes the increased surface energy (μ_{surf}) of the particles due to the Gibbs-Thomson effect. The second term (μ_{bind}) represent the term that will lower the overall chemical potential due to the binding of the surface ligands. When the two terms have different functional dependence on the size of the nanoparticles, the overall chemical potential will have a minimum at a given size. Interestingly, for perfectly spherical particles the argument will not work because both the surface energy and the binding energy scale the same way, resulting in no minimum in the overall chemical potential. These ideas translate into the CdTe system in a similar way. Under cadmium-rich conditions, the binding ligand is the hexyl phosphonic acid, which does not result in a minimum (or very broad minimum) in the overall chemical potential curve, which leads to relatively broad size distribution via thermodynamic control. When the conditions are tellurium-rich, the tellurium will act as a ligand, which produces a minimum in the overall chemical potential, corresponding to the above observed magic-sized CdTe nanoparticles. When various ligands are used under tellurium-rich conditions, the aggregation pattern remains almost identical, supporting this assumption. The above model is rather simplistic and ignores the details of the atomic and molecular structure of the nanoparticles and binding ligands. A more detailed understanding of the binding is expected from calculations.

Simulation of Aggregation Dynamics of Nanoparticles

To understand the aggregation dynamics of the nanoparticles better, a kinetic simulation is implemented. The goal of the simulation is to reproduce the experimentally observed aggregation pattern of the magic-sized CdTe nanoparticles and to verify whether the aggregated

particles form a neck or undergo complete collapse and phase transformation. In other words, if a particle with volume$_1$ and another particle with volume$_2$ collide, then is the volume of the resulting particle the sum of the volumes of the colliding particles or is it larger? The simulation consists of two major parts: (1) the monomer-induced growth of the particles and (2) the aggregation of the nanoparticles. The monomer-induced growth is explained in detail by Talapin et. al.[4] and by equation 3.2 in terms of dimensionless parameters, where dr/dτ is the size-dependent growth rate of nanoparticles, S is the monomer oversaturation, K is a dimensionless parameter describing whether the growth is reaction-controlled or diffusion controlled, and α is the transfer coefficient. For this work only the diffusion-controlled case is considered.

$$\frac{dr}{d\tau} = \frac{S - e^{\frac{1}{r^*}}}{r^* + Ke^{\frac{\alpha}{r^*}}} \qquad (3.2)$$

First, the calculation of the rate of aggregation proceeds by calculation of the Brownian collision frequency of particles. The collision frequency (q) of particles i and j is

$$q(i,j) = 4\pi(D_i + D_j)(R_i + R_j) \quad (3.3)$$

where, D_i is the size-dependent diffusion coefficient of particle i.

$$D_i = \frac{k_B T}{6\pi\mu R_i} \qquad (3.4)$$

The aggregation of the particles is described by the Smoluchowski equation:[30,31]

$$\frac{dn_k}{dt} = \frac{1}{2}\sum_{i=1}^{k-1} q(k-1,i)n_{k-i}n_i - n_k\sum_{i=1}^{\infty} q(i,k)n_i \qquad (3.5)$$

Here, dn/dt describes the population change of the k^{th} particles due to the formation of new aggregates from smaller particles. To consider the effect of the increased aggregation rate due to the presence of the dipole-dipole interaction, the collision frequency is expressed as q(i,

j)/*W*, where *W* describes the modification of the collision frequency due to the presence of a potential. *W* takes values between 0 and 1, thus increasing the collision frequency between particles when there is a strong interaction.

$$W = (R_i + R_j)\int_{R_i+R_j}^{\infty} \frac{e^{\frac{\Phi}{k_B T}}}{h^2} dh \qquad (3.6)$$

The potential can take into account van der Waals, Coulumbic, and dipole-dipole interactions. In the simulation, three cases of *W* are used. The first case is aggregation in the absence of the field when *W* = 1, which is the pure Brownian aggregation mechanism. The second case is the oriented attachment of two dipoles centered on the spherical quantum dots. For the oriented attachment, the dipoles are considered in a head-to-tail arrangement. The third approach takes into account the spatially averaged dipole-dipole interaction between particles. The simulation consists of several steps. Initially, a large number of particles are generated with a given size and size distribution. Although other cases are considered, in this study the size and size distribution of the particles correspond to those of the experimentally observed magic-sized CdTe nanoparticles (Figure 3.3). In the simulation, the actual size and size distribution of the particles are slightly different from those determined from TEM measurements. The sizes used in this article are determined on the basis of the sizing curve of CdTe quantum dots because correlation is sought between the optical measurement and the simulation. In the following step, the evolution of the distribution is calculated in the same manner as described previously. Subsequently, the size distribution of the particles is modified by the aggregation rate. The parameters used in the simulation presented here are shown in table 3.1.

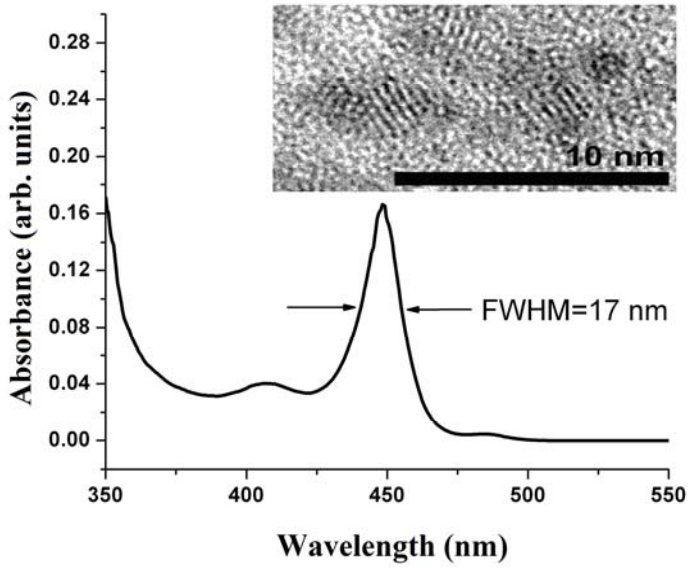

Figure 3.3 Absorption spectrum of the magic-sized CdTe nanoparticles The inset shows the HRTEM image of the zinc blende structure of the magic-sized nanoparticles.

Simulation Results

Figure 3.5a-e shows the results of the simulations. Each subfigure shows the evolution of the particle distribution versus time. The sizes of the particles are expressed in terms of particle volume (nm^3) and wavelength of absorption. The absorption wavelength is derived from the experimentally determined sizing curve for CdTe nanoparticles.[22] The particle population is expressed on a log scale to enhance the population of the larger nanoparticles. Although there is no theoretical justification for using a log scale, it is well known that the particle absorption cross section scales with increasing nanoparticle size. Because of a lack of knowledge of some of the simulation parameters, the simulation intends only to seek qualitative agreement with the experiment. The dashed lines on the right indicate the experimentally observed sizes of CdTe

nanoparticles. Surprisingly, the positions of the absorption peaks remain very close in each experiments even if the experimental parameters are varied widely (different ratios of TOPO/HDA, temperature 240-270 ^{0}C, changing length of the amine).

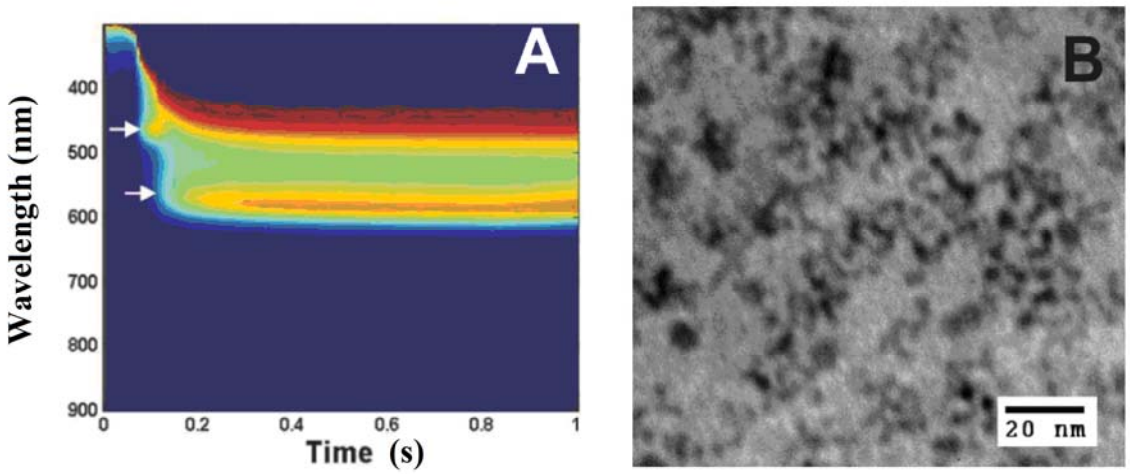

Figure 3.4 a) Evolution of the in situ absorption spectra of the CdTe nanoparticles using Me_2Cd for 2:1 Cd/Te ratio. The arrows indicate the appearance of sharp peaks corresponding to magic sized nanoparticles. b) Low resolution TEM image of the CdTe nanoparticles from the synthesis is shown.

Figure 3.5a shows the evolution of particles in the absence of aggregation and in the case of high initial monomer concentration. The nanoparticle distribution quickly evolves to a larger size; meanwhile, the size distribution of the particles decreases as a result of focusing effects. In the final stage of the simulation, the free monomer concentration drops to close to the solubility of the monomer ($S \approx 1$) from the initially supersaturated solution ($S_{initial} = 900$, used in the literature[4]). Once all of the monomers are used, no appreciable growth occurs; only Ostwald ripening occurs, resulting in an

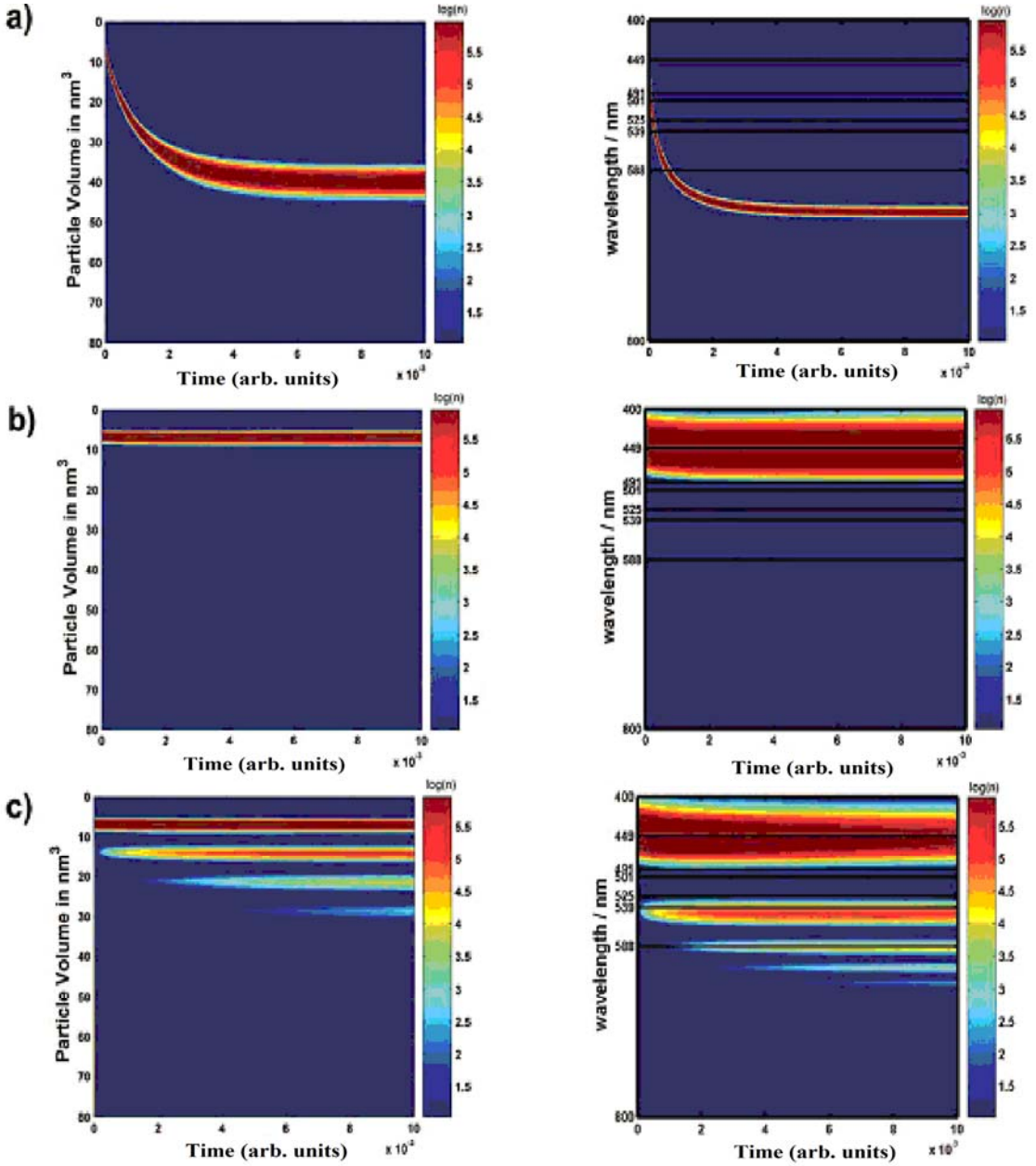
a)
b)
c)
Particle Volume in nm3
wavelength / nm
Time (arb. units)
log(n)

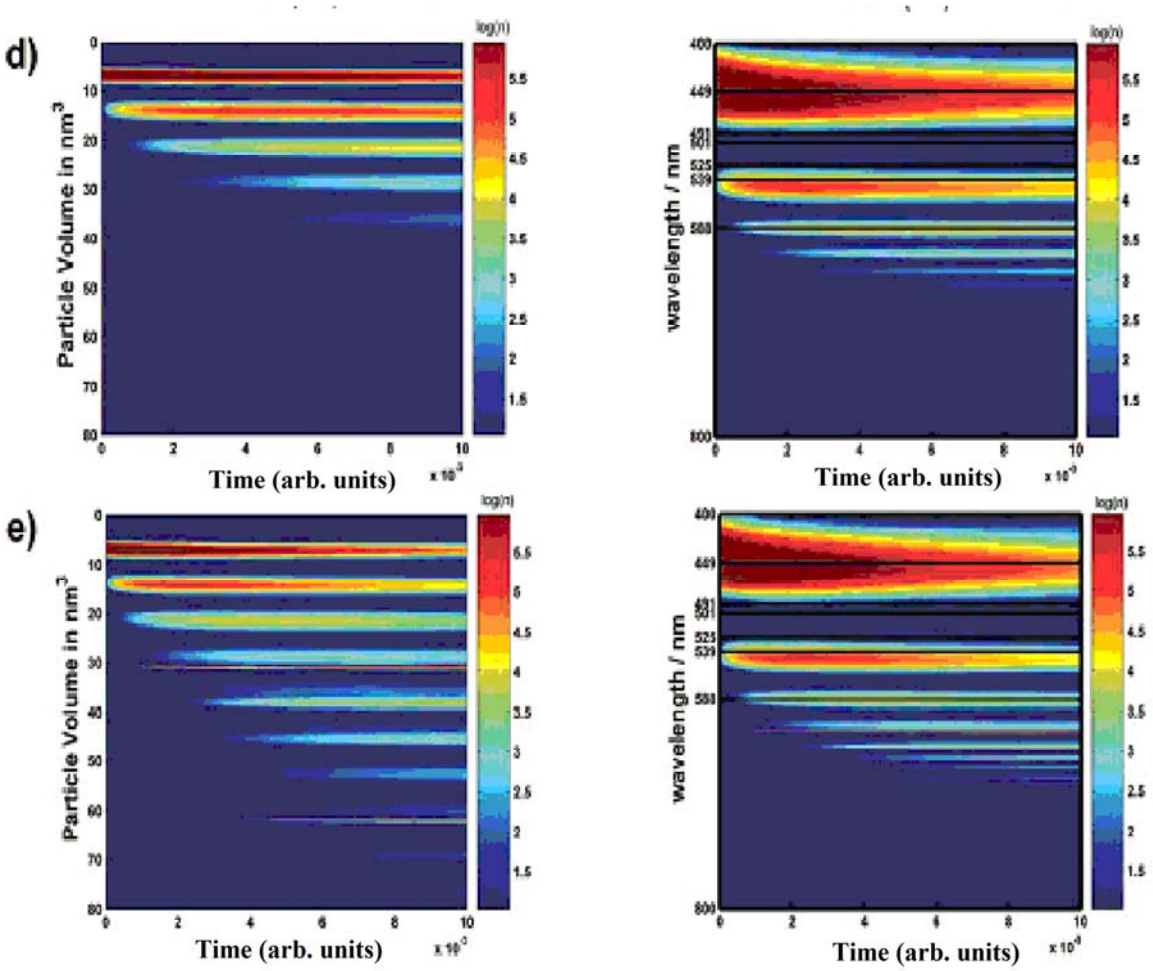

Figure 3.5 Simulation of the nanoparticle ensemble evolution for different conditions. The left and right graphs show the evolution particle distribution in nm^3 and wavelength, respectively (see text). The initial size distribution is 1.185±0.03 nm, which is equal to the size distribution of the magic sized nanoparticles. a) S=900 (used in the literature[4]), no aggregation b) S=10, no aggregation c) S=10, Brownian type aggregation d) S=10, Aggregation with Oriented attachment e) S=10, Aggregation with average dipole-dipole interaction potential

increase in the size distribution. The experiments suggest that the positions of the absorption peaks corresponding to nanoparticle sizes do not show appreciable changes once they are formed. For this reason, Figure 3.5b describes a more reasonable condition when the

supersaturation is much smaller ($S_{initial}$ = 10); therefore, the rate of change of the particle size distribution and the average size is smaller. In this figure, the nanoparticle distribution slightly increases, but the average size stays approximately constant. The slight broadening of the size distribution is a direct result of Ostwald ripening. The relatively slow change in the size distribution is due to how the rate-of-change curve overlaps with the particle size distribution used in the experiments.

Table 3.1 Some Parameters of CdTe QDs

Parameter	Value
S	10/900
K	0.001 (diffusion-controlled)
μ	100 D^{32}
Monomer volume	4.1 × 10-5 mol/m^3 for CdTe
simulation volume	3 × 10-13 m^3
no. of particles	(5-10) × 10^3
Dt	(2-20) × 10^{-3}
A	0.5
initial particle size	*R* = 1.185 and 0.812 nm

fwhm of distribution	*0.03 and 0.3 nm*
dt	(2-20) × 10^{-5} s
no. of steps	(5-20) × 10^{3}

Figure 3.5c-e represents the data obtained when aggregation is turned on in the simulations. As described previously, the supersaturation of the monomer is chosen arbitrarily to be a relatively low value (S =10). The subsequent peaks in the graph correspond to the volume changes induced by the aggregation of the nanoparticles. If the particle distribution is neglected, then the corresponding volume of each peak is an integer times the volume of the magic-sized particles. As mentioned above, three cases considered here are the Brownian aggregation (Figure 3.5c), the oriented attachment (head to tail) of dipoles (Figure 3.5d), and the average attraction between randomly oriented dipoles (Figure 3.5e). The magnitude of the dipoles is set uniformly at 100 Debye, which seems to be in good agreement with literature values.[32] The data from Figure 3.5c-e are different in two ways. First, the rate of aggregation is increased. At the same time, the appearance of the larger aggregates is faster. This is an expected result based on the basic assumption of the model. The increased aggregation rate of the smaller particles from dipoles is from a relatively small W (increased collision frequency) from equation 3.5. The dipole-dipole interactions also change the shape of the individual size distributions because to the left and right of the distribution of particles there will be modified rates of aggregation relative to the one predicted from the simple Brownian aggregation model. Although it might be interesting to evaluate the shape of the individual distributions, the large error in the experiments will not yield meaningful comparisons. More meaningful comparisons can be obtained from the

analysis of the previously observed peak positions. In the previous paper, the observed room-temperature absorption peak positions are 410, 449, 491, 501, 539, and 588 nm. These peak positions consistently appear at the same wavelength even when the experimental parameters are widely varied. The corresponding radii of the CdTe nanoparticles are 1.13 (6.0), 1.185(7.0), 1.3(9.2), 1.335(10), 1.475(13.4), and 1.72(21.3) nm, respectively. The size distribution of the particles is approximately 30% of the average size from TEM measurements, and the values in parentheses indicate the volume of the nanoparticles in nm^3. Naturally, as the reaction proceeds, there are more peaks, but the aggregation effect is washed out and larger sizes are not clearly observable. The first peak at 1.13 nm is identified only on the basis of a room temperature absorption spectrum and is related to the sizing curve. However, this peak has not been clearly identified by HRTEM. It is more likely that this peak is the secondary excitonic peak of the 1.185 nm CdTe magic-sized nanoparticles (the 449 nm peak maximum in the absorption in Figure 3.3); therefore, it is omitted in further discussions. The experimental absorption peak positions of the various CdTe nanoparticles are indicated by dashed lines in the simulations.

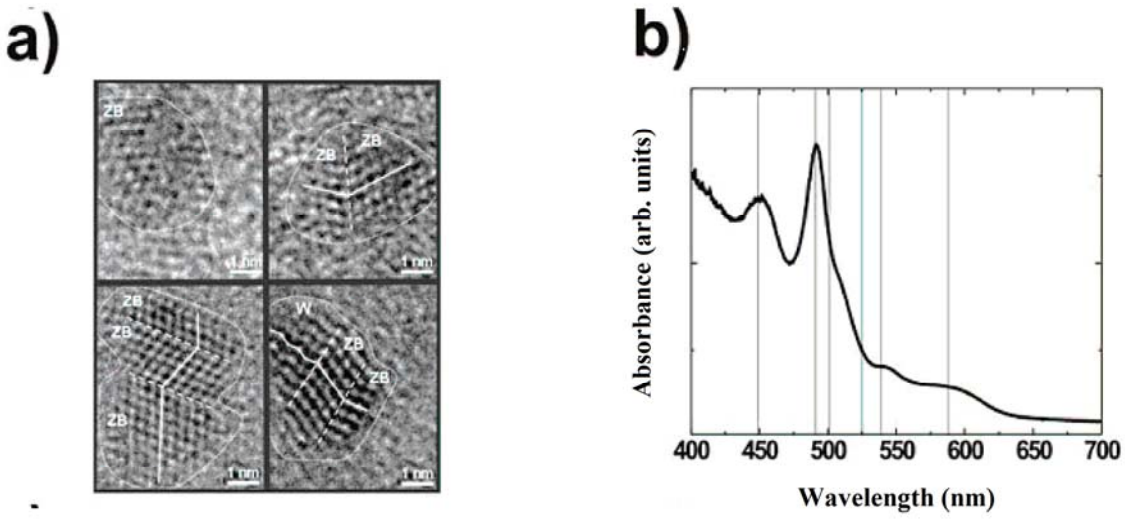

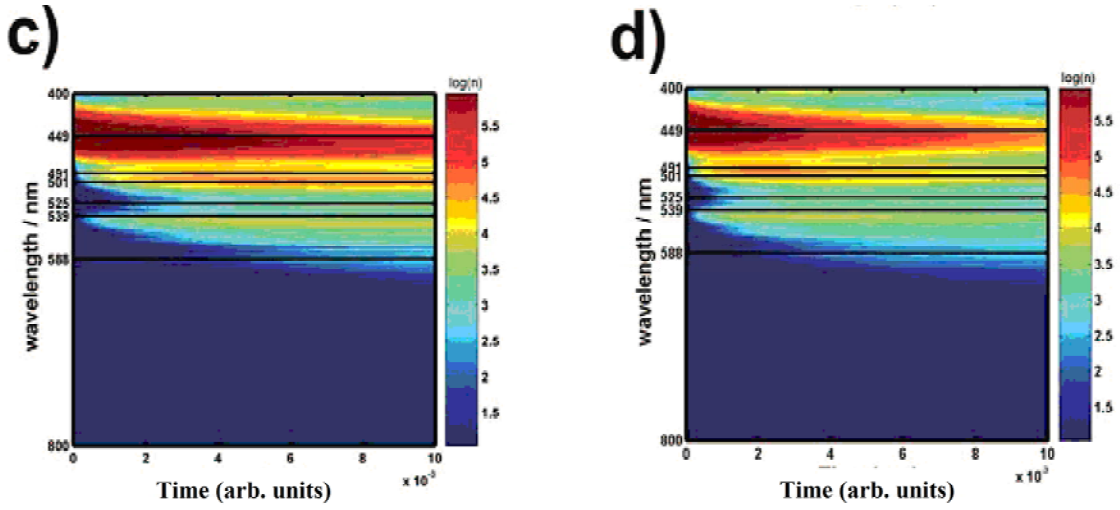

Figure 3.6 Simulation of the nanoparticle ensemble evolution for a) an initial double size distribution of 0.813±0.03 nm and 1.185±0.03 nm. b) Experimental data showing the absorption peaks of the CdTe nanoparticle aggregates. The solid lines indicate the sizes previously identified. c) S=10, Brownian aggregation of the double size distribution d) S=10, Aggregation with the average dipole-dipole interaction potential

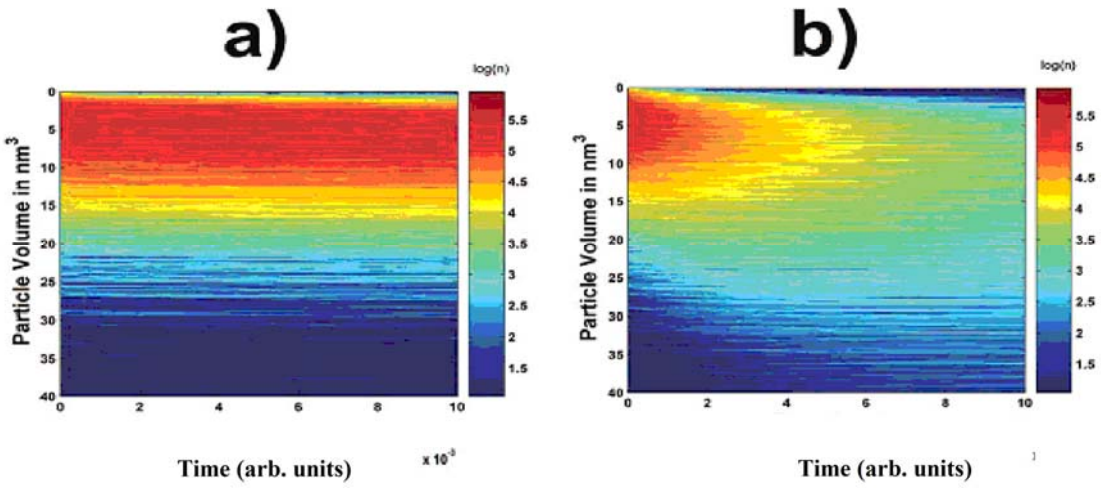

Figure 3.7 Simulation of the nanoparticle ensemble evolution for a) an initial broad size distribution, which is 1.185±0.3 nm. b) S=10, Brownian aggregation of the broad size distribution

The comparison of the experiment (dashed line on the simulations) and the simulation reveal that some of the sizes can be reproduced very well, but some sizes are missing. Specifically, the 539 nm (r =1.475 nm or V = 13.4 nm^3) and the 588 nm (r = 1.72 nm or V = 21.3 nm^3) absorption peaks are well fit by the simulations (2 and 3 times the volume of the first magic size). This also means that for some sizes the volume of the magic-sized nanoparticles is an additive property, which suggests that the neck formation during nanoparticle aggregation is not significant under the experimental conditions. Interestingly, the particles corresponding to the 491 and 501 nm absorption peak positions (r = 1.3 and 1.335 nm) are missing from the simulation if a single magic size is initially assumed. To resolve the puzzle, a second set of simulations are carried out when the initial distribution is assumed to be a double distribution of two different magic-sized particles (r = 1.185 and 0.812 nm, see Figure 3.6a). The first magic-sized particles are kept from the first set of simulations (observed experimentally), and the second set of magic-sized particles is chosen so that the volume of the first and second set of magic-sized particles equals the volume of the particle indicated by the 491 nm absorption peak position. The comparison of the experiment (Figure 3.6b) and the results from these simulations are shown in Figure 3.6c, d using the Brownian and average dipole-driven aggregation described above. Both of these simulations qualitatively yield similar results. The particle sizes corresponding to 491, 501, and 525 nm are reasonably well reproduced with respect to the experimental observation.

The question remains as to whether there is any rationale behind the observed second set of magic-sized CdTe nanoparticles. Although efforts have been made in our group using the MALDI technique, the particles could not be identified. Because the first magic size is relatively small and very reactive, it is speculated that the difficulty lies with the isolation of the

nanoparticles (and their reactivity). This is supported by the observation of the relatively low stability of the CdTe particles. The absence of the peak from the high-temperature spectrum is not a proof of the absence of particles in the growth solution. This is especially true for very small nanoparticles, whose absorbance is skewed by the presence of the solvent and precursor absorption. It is reasonable to assume that if one magic size is observable then there might be other smaller nanoparticles. Although no direct experimental evidence is given of multiple magic sizes present, recent experiments by Manin et. al.[21] have shown the presence of multiple CdSe magic-sized particles coexisting in solution. Similarly, Tonti et. al.[20] reported the presence of distinct sizes of CdSe nanoparticles under selenium-rich conditions supporting the above assumption. Briefly, the conclusions of this work are that the simulation gives good agreement between experiment and theory in terms of aggregation. The simulation suggests additional magic sizes present in the growth solution. Dipole-dipole interaction increases the rate of aggregation but, to first approximation, does not change the quality and the result of the aggregation of particles.

At last, the distribution of nanoparticles is chosen to be broad initially. The results are shown in Figure 3.7. Figure 3.7a indicates the evolution of the particle size distribution in the absence of aggregation and at low monomer oversaturation. The distribution becomes slightly broader, and Ostwald ripening is the dominating process. However, when the aggregation is turned on (Figure 3.7b), then the size distribution tends to shift to the red slightly without the presence of any distinct peaks. This situation seems to be well correlated with the experimental data presented above for the cadmium-rich condition (Figure 3.1a). In the case of the cadmium-rich condition, no well-defined peaks appear, and the first shoulder appears at a considerably larger size. These results suggest that even under cadmium-rich conditions there is aggregation

contributing to the nanoparticle distribution. The aggregation mechanism under cadmium-rich conditions is also supported by the XRD of the final products as shown in Figure 3.2. Under cadmium-rich conditions, no magic size is observed; therefore, the size of crystalline domains of the larger aggregates will be smaller than under tellurium-rich conditions.

Finally, it is important to asses how the aggregation of CdTe quantum dots and the simulation carried out in this study would correlate with nanowire formation from CdTe quantum dots in an aqueous environment.[15] We believe that water would have two significant effects on the aggregation dynamics. First, the dielectric constant of water is significantly higher that those of organics, resulting in reduced particle-particle interaction. Second, redox reactions become possible, which changes the surface chemistry; therefore, the magnitude of the permanent dipole might be very different.

Conclusions

The primary reason for the observed sequential appearance of absorption peaks is due to the formation of magic-sized NPs and not due to the aggreagation mechanism. The exact reproduction of data may critically depend on many parameters, but these data show qualitative agreement with the kinetics of the appearance of various nanoparticle sizes and quantitative agreement with the peak positions.

References

1. Shipway, A. N.; Katz, E.; Willner, I. *ChemPhysChem* **2000**, *1*, 18–52.

2. Danek, M.; Jensen, K. F.; Murray, C. B.; Bawendi, M. G. *Chem. Mater.* **1996**, *8*, 173–180.

3. Jin, R.; Cao, Y. C.; Hao, E.; Me´traux, G. S.; Schatz, G. C.; Mirkin, C. A. *Nature* **2003**, *425*, 487–490.

4. Talapin, D. V.; Rogach, A. L.; Haase, M.; Weller, H. *J. Phys. Chem. B* **2001**, *105*, 12278 12285.

5. Peng, X. G.; Wickham, J.; Alivisatos, A. P. *J. Am. Chem. Soc.* **1998**, *120*, 5343–5344.

6. Yao, J. H.; Elder, K. R.; Guo, H.; Grant, M. *Phys. Re*V. *B* **1993**, *47*, 14110–14125.

7. Tu, H.; Yang, S.; Chikan, V.; Kelley, D. F. *J. Phys. Chem. B* **2004**, *108*, 4701–4710.

8. Kalsin, A. M.; Pinchuk, A. O.; Smoukov, S. K.; Paszewski, M.; Schatz, G. C.; Grzybowski, B. A. *Nano Lett.* **2006**, *6*, 1896–1903.

9. Bishop, K. J. M.; Grzybowski, B. A. *ChemPhysChem* **2007**, *8*, 2171–2176.

10. Harrisson, S.; Wooley, K. L. *Chem. Commun.* **2005**, 3259–3261.

11. Wu, Z.-S.; Guo, M.-M.; Shen, G.-L.; Yu, R.-Q. *Anal. Bioanal. Chem.* **2007**, *387*, 2623–2626.

12. Tang, Z. Y.; Kotov, N. A.; Giersig, M. *Science* **2002**, *297*, 237–240.

(13) Shanbhag, S.; Kotov, N. A. *J. Phys. Chem. B* **2006**, *110*, 12211–12217.

14. Ethayaraja, M.; Bandyopadhyaya, R. *Langmuir* **2007**, *23*, 6418–6423.

15. Tang, Z.; Zhang, Z.; Wang, Y.; Glotzer, S. C.; Kotov, N. A. *Science* **2006**, *314*, 274–278.

16. Yong, K. T.; Sahoo, Y.; Zeng, H.; Swihart, M. T.; Minter, J. R.; Prasad, P. N. *Chem. Mater.* **2007**, *19*, 4108–4110.

17. Cho, K. S.; Talapin, D. V.; Gaschler, W.; Murray, C. B. *J. Am. Chem. Soc.* **2005**, *127*, 7140–7147.

18. Caudia Pacholski, A. K. H. W. *Angew. Chem., Int. Ed.* **2002**, *41*, 1188–1191.

19. Yu, J. H.; Joo, J.; Park, H. M.; Baik, S. I.; Kim, Y. W.; Kim, S. C.; Hyeon, T. *J. Am. Chem. Soc.* **2005**, *127*, 5662–5670.

20. Tonti, D.; Mohammed, M. B.; Al-Salman, A.; Pattison, P.; Chergui, M. *Chem. Mater.* **2008**, *20*, 1331–1339.

21. Kudera, S.; Zanella, M.; Giannini, C.; Rizzo, A.; Li, Y. Q.; Gigli, G.; Cingolani, R.; Ciccarella, G.; Spahl, W.; Parak, W. J.; Manna, L. *Ad*V. *Mater.* **2007**, *19*, 548.

22. Dagtepe, P.; Chikan, V.; Jasinski, J.; Leppert, V. J. *J. Phys. Chem. C* **2007**, *111*, 14977–14983.

23. Rockenberger, J.; Tro¨ger, L.; Rogach, A. L. *J. Chem. Phys.* **1998**, *108*, 7807.

24. Boyen, H. G.; Kastle, G.; Weigl, F.; Koslowski, B.; Dietrich, C.; Ziemann, P.; Spatz, J. P.; Riethmuller, S.; Hartmann, C.; Moller, M.; Schmid, G.; Garnier, M. G.; Oelhafen, P. *Science* **2002**, *297*, 1533–1536.

25. Leff, D. V.; Ohara, P. C.; Heath, J. R.; Gelbart, W. M. *J. Phys. Chem.* **1995**, *99*, 7036–7041.

26. Stoeva, S.; Klabunde, K. J.; Sorensen, C. M.; Dragieva, I. *J. Am. Chem. Soc.* **2002**, *124*, 2305–2311.

27. Deng, D. W.; Qin, Y. B.; Yang, X.; Yu, J. S.; Pan, Y. *J. Cryst. Growth.* **2006**, *296*, 141–149.

28. Leff, D. V.; Ohara, P. C.; Heath, J. R.; Gelbart, W. M. *J. Phys. Chem.* **1995**, *99*, 7036–7041.

29. Chikan, V.; Kelley, D. F. *J. Phys. Chem. B* **2002**, *106*, 3794–3804.

30. Friedlander, S. K. *Smoke, Dust, and Haze: Fundamentals of Aerosol Dynamics*; Oxford University Press: New York, 2000.

31. Ethayaraja, M.; Bandyopadhyaya, R. *Langmuir* **2007**, *23*, 6418–6423.

32. Shanbhag, S.; Kotov, N. A. *J. Phys. Chem. B* **2006**, *110*, 12211–12217.

CHAPTER 4 - Quantized Ostwald Ripening of Colloidal Nanoparticles

Introduction

Controlling the growth of nanoparticles (NPs) is important in order to create uniform particles with narrow size distributions for both fundamental science and technology. Ostwald ripening (coarsening) is one of the general growth mechanism that controls NP syntheses.[1-3] In general, colloidal particles are inclined to minimize their surface-to-volume ratio thereby their surface free energy. Lifshitz-Slyozov-Wagner (LSW) theory describes the size evolution of particles in terms of reducing the overall surface energy of the system. The LSW ripening critically depends on the solubility of the particles as a function of size.[3] In a system where small particles are in equilibrium with larger particles, the overall size and size distribution will increase over time.

A NP with radius larger (smaller) than a critical radius grows (dissolves), which is commonly called the Ostwald ripening. The critical radius is a function of the solution and NP's properties. The corresponding equation of the critical radius is as follows;[4]

$$r_{cr} = \frac{2\gamma V_m}{RT \ln S} \qquad (4.1)$$

In this equation, S is supersaturation of the monomers in solution, which is the ratio of the actual monomer concentration to the monomer solubility over a flat surface; R is gas constant, T is temperature, γ is specific surface energy, V_m is monomer volume. The dissolution of small particles and growth of larger particles is explained by the curvature dependence of the chemical potential;[5]

$$\mu = \mu_0 + V_m \gamma \kappa \qquad (4.2)$$

Here μ_0 is the chemical potential of atom on a flat interface, κ is mean interfacial curvature, V_m is molar volume, and γ represents specific surface energy. This equation points out the direction of material flow; from high to low curvature. Therefore, regions of high curvature (smaller particles) with high energy disappear and lower energy regions of larger particles prevail. As a result of the material flux, the total free energy of the system decreases. Ostwald ripening process results in broadening of size distribution of NPs due to the consumption of small particles in order to assist the growth of larger ones with lower surface energy.[6, 7] Simulation of the size evolution of NPs based on the LSW theory shows that the initial Gaussian size distribution of NPs will become asymmetric.[8, 9]

The inverse process of the Ostwald ripening is the size focusing of NPs. Experimentally, several research groups have achieved narrowing of size distribution (focusing) in colloidal systems and NPs.[7, 10-16] The simplest way to obtain size focusing is to utilize particles from longer reaction times and perform size selective separation based on the solubility difference of different sized particles.[12, 17] The size selective precipitation method usually requires large amount of solvent that could make the approach rather costly. Alternatively, NPs can be focused by fine tuning the reaction conditions to achieve a supersaturated environment with respect to the monomer. At the practical level, this is carried out by using so called multiple-injection method. In multiple injection method, when the size of the particles de-focuses from a regular nanoparticle synthesis, a second injection of molecular precursors takes place. The second injection causes the broad distribution to re-focus.[7] Multiple injection method requires precise timing since the growth of the nanoparticles is rather fast at high temperatures. In addition re-nucleation can take place from the relatively high monomer concentrations and solution inhomogeneities. Therefore, developing methods to increase the time to generate the size

focusing is key importance in industrial-scale laboratory synthesis of semiconductor nanocrystals with uniform size and shape.

The growth of NPs in the bimodal growth regime, which is studied by several groups,[6, 18-22] has already been shown to result in narrowing of size distribution of NP systems. Peng`s work[22] has revealed that focusing of size distribution takes place when two different sized CdS NPs are mixed at higher temperatures. During the CdS ripening, the initial two-different sized particles possessing broad size distributions undergo size focusing. According to Peng, focusing of size distribution is observed due to the dissolution of small particles in CdS solution while larger particles do not dissolve.[22] This study demonstrates the effect of interparticle interaction on the size distribution for a diffusion-controlled process. A similar observation has been reported on CdSe nanoparticles. The bimodal distributions of CdSe NPs are formed spontaneously in the growth solution at low temperatures.[20] In this system, CdSe NPs with different size values coexist for hours and focusing of size distribution takes place in the reaction system similarly to Peng's observation.[20] Another recent deliberate attempt to utilize bimodal distribution to focus the size distribution is presented by Fu et. al. This group has applied the bimodal size distribution approach to ZnO NPs via 'supersaturation control' of the monomers.[21] Besides solution-based nano materials, there are studies on the size evolution of nanomaterials on surfaces. One of the studies is on the island of nanostructured clusters. Ross et. al.[23] have observed the narrowing of the size distribution of Ge islands upon a shape transition from pyramid to dome.

The motivation of this work is to examine how the addition of small sized sacrificial nanoparticles (SNPs) to the growth solution will affect the size focusing via Ostwald ripening. The results from the Monte Carlo simulation aim to find optimum conditions to produce size

focusing. In this numerical simulation, growth rate of nanoparticles is calculated based on a method under diffusion control.[4] The multiple injection method and the Ostwald ripening process are also considered to assess the usefulness of this approach. The effect of re-nucleation rate is also studied and the calculations show that bimodal distribution yields lower rate of re-nucleation compared to the multiple injection method.

Methods

The numerical simulation method is used here to explain the behavior of bimodal size distribution of nanoparticles based on a literature method.[4] Growth of particles is controlled by the size dependant growth rate (3a).[4]

$$\frac{dr}{d\tau} = \frac{S - e^{\frac{1}{r^*}}}{r^* + Ke^{\frac{\alpha}{r^*}}} \qquad (4.3a)$$

$$r^* = \frac{RT}{2\gamma V_m} \qquad (4.3b)$$

$$\tau = \frac{R^2T^2DC^0_{flat}}{2\gamma^2 V_m}t \qquad (4.3c)$$

$$K = \frac{RT}{2\gamma V_m}\frac{D}{k_g^{flat}} \qquad (4.3d)$$

In these equations, dimensionless radius, time, and K are used given by equations 4.3b and 4.3c, respectively. S is the supersaturation of the monomers in solution, T is the temperature, R is the gas constant, D is diffusion coefficient, C^0_{flat} is solubility of the monomer in equilibrium

with a flat surface, k_g^{flat} is the rate constant for a first order deposition reaction, K is the ratio of the diffusion constant of the monomer to the reaction rate constants and indicates whether it is diffusion (K << 1) or the reaction-controlled (K >> 1) process. In this system a value of 0.001 for K is used which shows that the system is under diffusion control. Volume of the solution simulated is $3x10^{-18}$ m^3. The parameters used in the calculations are given in table 4.1 and are derived from the material parameters for a CdSe nanoparticles synthesis.

Table 4.1 Parameters and the values used in the simulation

Parameter	**Value**
Temperature	573 K
monomer volume (V_m)	3.29×10^{-5} m^3/mol
simulated volume	3×10^{-18} m^3
K	0.001
transfer coefficient (α)	0.5
monomer solubility	10^{-2} mol/m^3
specific surface energy (γ)	0.125 J/m^2

This simulation focuses on the effect of SNP (sacrificial nanoparticle) to the growth solution (quantized Ostwald ripening-QOR) in comparisons with the Ostwald ripening (OR) process and the multiple injection method (MI). In QOR approach, 1 nm-sized CdSe nanocrystals are added to the particles sizes changing between 3 to 4.5 nm with 10 % size distribution. The large difference in nanoparticles sizes is necessary to reduce mixing between the two distinct sizes during the evolution of the growth solution. The 10% deviation from the average size corresponds to the experimentally achievable size distributions.[24] The number of

SNPs used is between 5×10^2-8×10^3 and the larger size ranges from 5×10^2 to 1.5×10^5 (full list of number of particles and sizes used in the simulated volume. In the multiple injection (MI), instead of addition of small particles, corresponding number of monomers calculated and added to the growth solution as it is carried out in the experimental multiple injection method.[4, 7]

$$S = \exp\left[\frac{2\gamma V_m}{rRT}\right] \approx \left[1 + \frac{2\gamma V_m}{rRT}\right] \qquad (4.4)$$

The size dependant solubility of the NPs is approximated by the first two elements of the Taylor-series of the Gibbs–Thomson equation. Although this approximation is arguable for small size NPs, it allows explicit expression of the size dependant growth rate of NPs. Calculated S is used in equation 4.3a to calculate the growth rate of NPs for each step. MI method has the same initial number of monomers in the simulation as in the QOR method in order to directly compare the two methods. Values of V_m, γ, T used here are given in table 4.1.

Simulation is carried out as follows (Figure 4.1). First, the initial size distributions are generated. The loop starts with the calculation of the growth rates for any given particle based on the S value of the solution (Figure 4.1, step 1). As expected, the S values are different for MI and QOR even though the same number of monomers is present in both solutions. The initial S value of QOR method is chosen to correspond to the S value from the size of SNP based on equation 4.4. The S value of the MI method is significantly higher than QOR and OR methods. This S value is the sum of S from QOR method + S calculated from the monomers present in the SNPs. The second step in the simulation is the calculation of change in the size after adding corresponding number of monomers in each step (Figure 4.1, step 2). The next step is finding the new size of particles after the growth stage (Figure 4.1, step 3). In this step, if the new size of the particle is less than zero the particle is dissolved resulting in a decrease in the number of

particles. After calculating the new size, new number of monomers (step 4), and change in the monomer number (step 5) are calculated. On the next step statistical parameters are calculated (step 5), such as, mean radius, standard deviation which examine the origin of the focusing in this particular growth process. Then as a last step a new supersaturation value is calculated. A summary of the steps of this simulation is shown in Figure 4.1. In this simulation, the data are obtained by using specific parameters for CdSe NPs (table 4.1). Talapin's previous work has been used as a benchmark to test the accuracy of the numerical approach.[4]

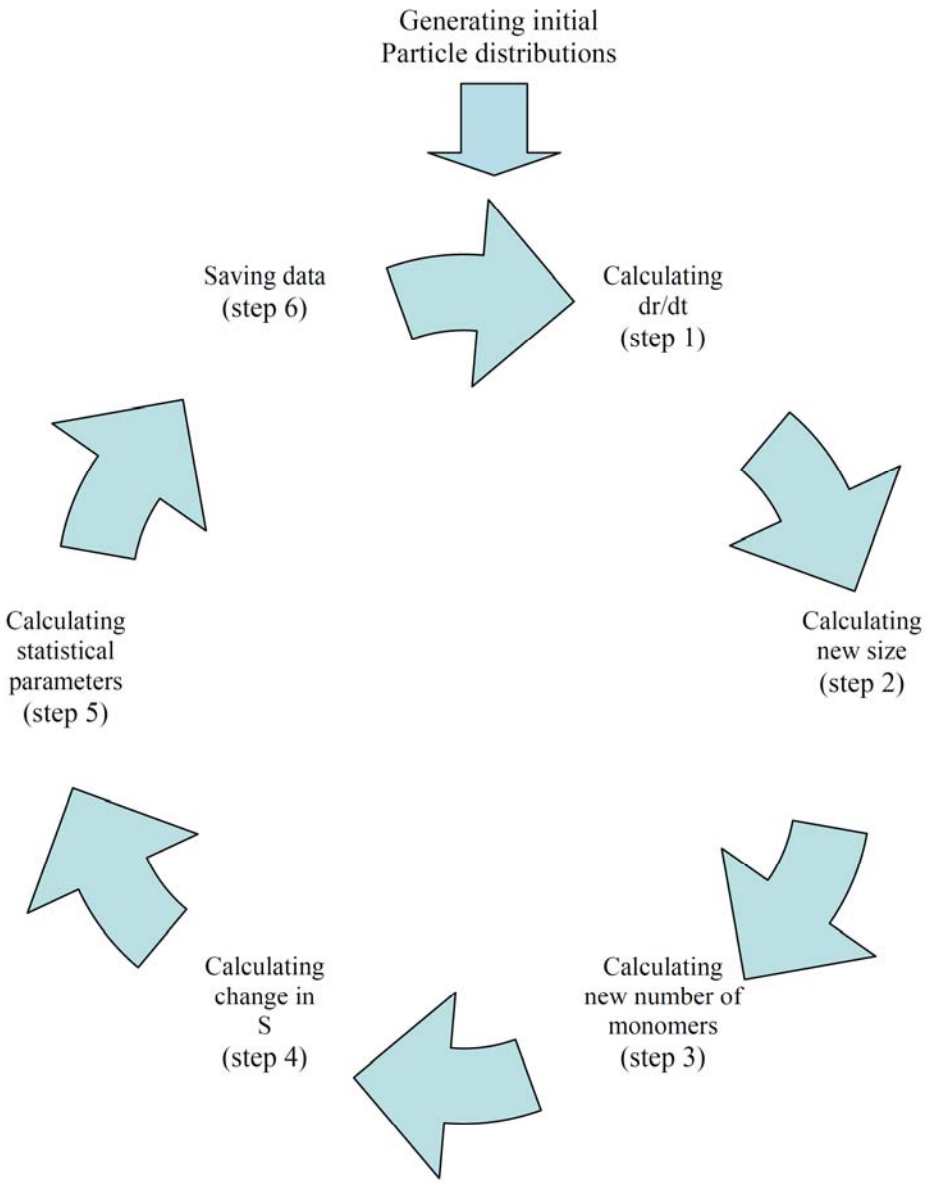

Figure 4.1 Flow chart of the steps of the simulation

Table 4.2 Different trials of the simulation

Simulation	# of monomers (SNP)	# of monomers (larger size)	SNPs	Larger size
1	8×10^4	2×10^3	1 nm	3.5 nm
2	4×10^4	2×10^3	1 nm	3.5 nm
3	2×10^4	2×10^3	1 nm	3.5 nm
4	8×10^4	2×10^3	1 nm	3 nm
5	8×10^4	2×10^3	1 nm	4 nm
6	8×10^4	2×10^3	1 nm	4.5 nm
7	8×10^4	5×10^2	1 nm	3.5 nm
8	8×10^4	1×10^3	1 nm	3.5 nm
9	8×10^4	1.5×10^3	1 nm	3.5 nm
10	8×10^4	2×10^3	1 nm	3.5 nm
11	8×10^4	3×10^3	1 nm	3.5 nm
12	8×10^4	4×10^3	1 nm	3.5 nm
13	8×10^4	8×10^3	1 nm	3.5 nm
14	0	2×10^3	1 nm	3.5 nm
15	2×10^4	2×10^3	1 nm	3.5 nm
16	3×10^4	2×10^3	1 nm	3.5 nm

17	4×10^4	2×10^3	1 nm	3.5 nm
18	5×10^4	2×10^3	1 nm	3.5 nm
19	6×10^4	2×10^3	1 nm	3.5 nm
20	8×10^4	2×10^3	1 nm	3.5 nm
21	1.2×10^5	2×10^3	1 nm	3.5 nm
22	1.6×10^5	2×10^3	1 nm	3.5 nm

Results and the Discussion

To investigate the size focusing from QOR, many of the most relevant simulation parameters to the experiment are systematically varied including the number of particles, initial supersaturation and sizes of SNPs and larger NPs present in the solution. Figure 4.2 shows a typical size evolution of particles consisting of an initial bimodal size distribution. The data illustrate the size histogram with 80×10^3 SNPs (r=1nm±0.1) and 2×10^3 larger ones (r=3.5nm±0.35). Black line indicates the change of critical radius over time. At the early stages of the simulation, the Figure clearly shows the disappearance of SNPs which are smaller than the critical radius (equation 4.1). Since the radii of large particles are greater than the critical radius, they undergo growth on the expense of SNPs. Later on, as the particles grow and the supersaturation drops, the larger size NPs will undergo Ostwald ripening shown by the broadening of the size distribution of larger sized NPs. At the end of the simulation, the size

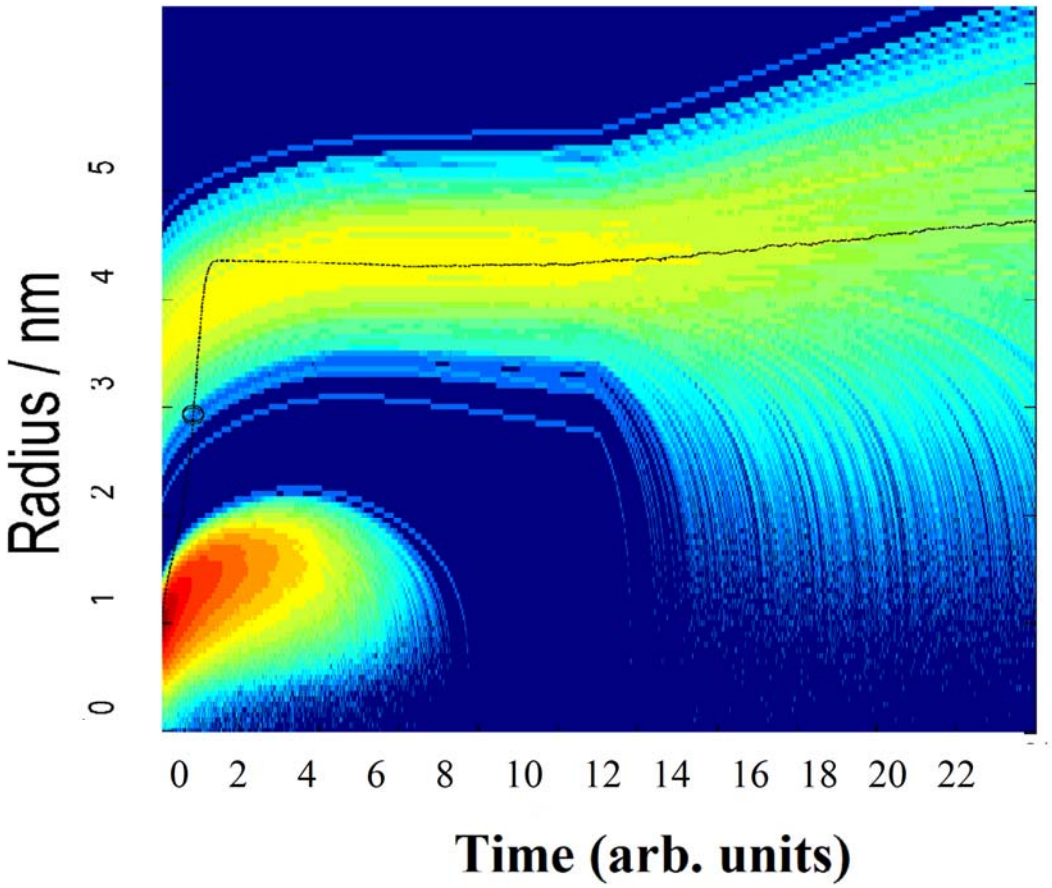

Figure 4.2 Size histogram of CdSe solution with 80x10^3 SNPs (r=1nm± 0.1) and 2x10^3 large ones (r=3.5nm±0.35). Black line indicates the change of critical radius with time.

distribution is asymmetric and corresponds to the distribution expected from LSW theory. Figure 4.3 shows the temporal evolution of the statistical parameters. Simulation of the time evolution of number of particles, size distribution, supersaturation and average size are carried out for different methods: While the supersaturation and number of particles include all particles present in the growth solution, the size and size distribution of only the larger particles are calculated

(assuming that once the reaction is over, only the larger NPs will remain and the SNPs will completely dissolve). In OR, no new particles or precursors are added to the growth solution as a result, average size gets larger and defocusing of size distribution takes place. In QOR, 8×10^4 small size, SNP, (r=1nm±0.1) of CdSe particles are added to 2×10^3 larger size (r=3.5nm±0.35). In MI method, the corresponding supersaturation value of QOR is calculated (354 from equation 4.4) and added to the reaction solution as in the repeated injection method[7, 25]. In other words, in MI the precursor and in QOR the small NPs (sacrifical nanoparticles, SNPs) are added to the solution containing a larger size. There is a decrease in number of particles over time. These SNPs dissolve and consequently, provide the monomers necessary for the larger ones to grow. The dissolution of particles is rather slow in the case of QOR. Therefore, the growth takes longer when it is compared to MI method. In QOR, the SNP provide constant addition of dissolved monomers to the solution and to the larger size NPs. Therefore, the increased supersaturation from the presence of SNP with highly curved surfaces lasts longer for QOR than in case of MI. Once SNPs are consumed, the size distribution defocuses via the 'regular' Ostwald ripening process. Figure 4.3 also shows how the absence of SNP affects the size distribution and the number of particles. Figure 4.4 summarizes the effects of different methods with different number of initial SNPs. The simulations suggest that possessing larger number of initial SNPs enhances the focusing of the larger size (better size focusing). The limit of these experiments will be based on the solubility of the SNPs in the solutions. Although the MI method creates a faster focusing than QOR , it is harder to control the growth of NPs experimentally. On the other hand, QOR's slow size focusing is advantageous in terms of reaction control. Potentially, the slower growth also may yield better quality nanocrystals if the defect removal rate is slower than the growth in case of MI method. Figure 4.5 shows the effect of increasing SNPs on the

supersaturation of QOR. When dissolution of particles takes place, the supersaturation of the larger number of particles tends to increase faster than the others. All of the different supersaturation values reach a similar maximum value and behave the same at the latter stage of the NP growth.

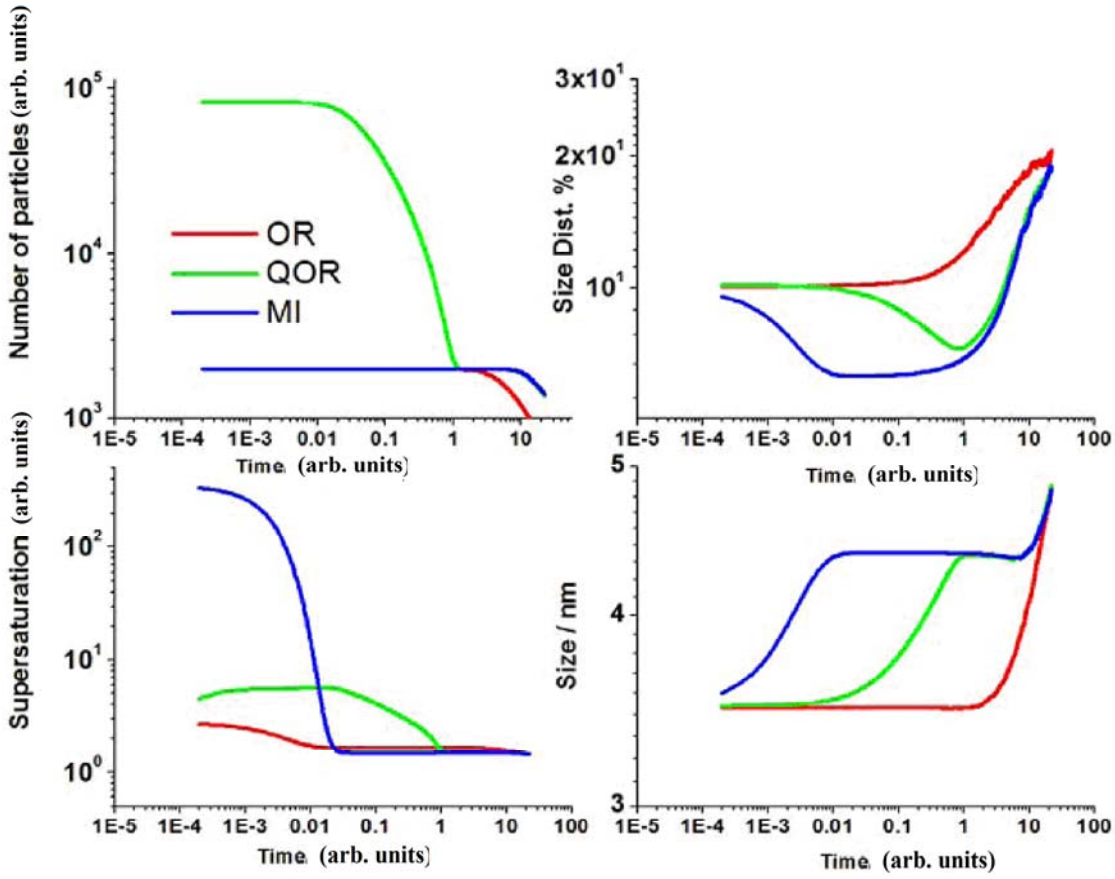

Figure 4.3 Simulation of the time evolution of number of particles, size distribution, supersaturation and size for different methods: OR (Ostwald Ripening) is shown by red lines (dark gray), QOR (Quantized Ostwald Ripening) is green lines (light gray), MI (Multiple Injection) is blue lines (black).

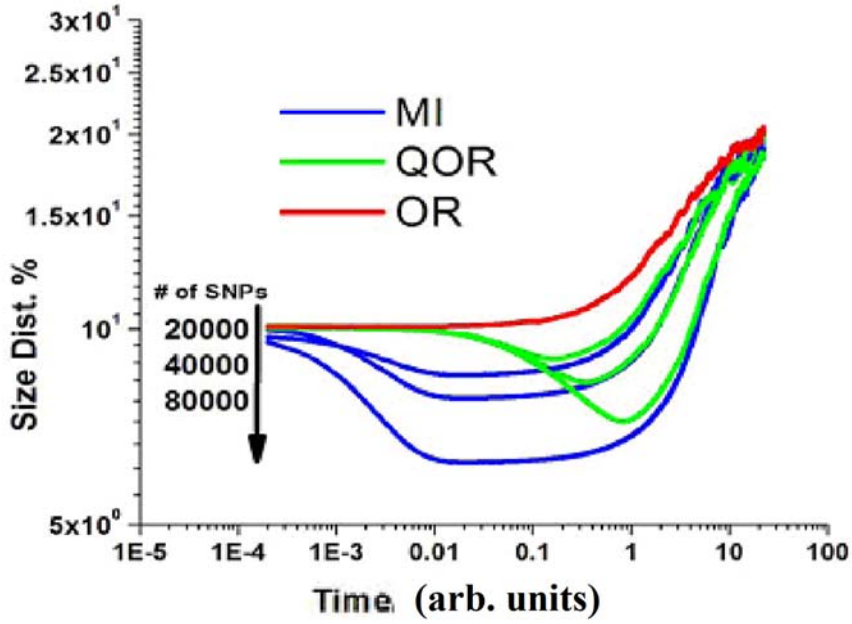

Figure 4.4 Temporal change of size distribution for MI, QOR and OR with addition of different number of SNPs.

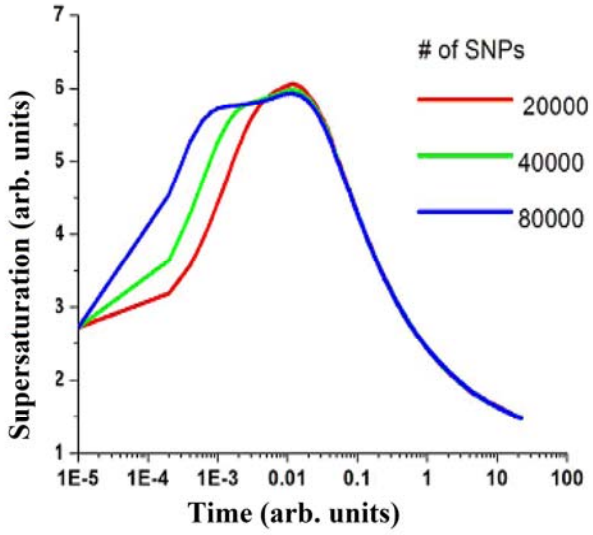

Figure 4.5 Temporal change of supersaturation with different initial number of small particles (first size).

In the previous part, a set of fixed sized particles have been simulated to explore the effect of varying number of particles on average size, supersaturation, size distribution, and number of particles. Simulations of changing the sizes of larger particles are carried out to investigate the effect on focusing. The results are summarized in Figure 4.6. The total number of

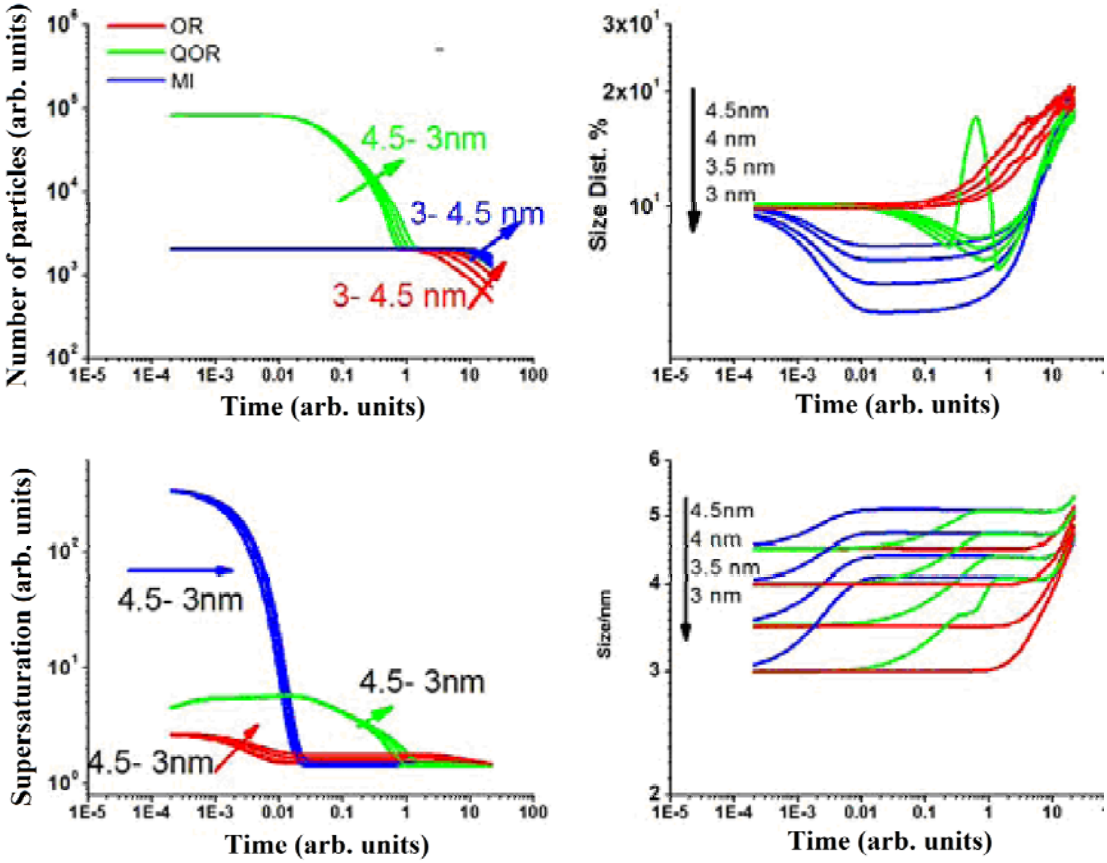

Figure 4.6 Temporal evolution of number of particles, size distribution, supersaturation, and size values are shown for different initial sized larger particles. The arrows show the direction of the size change for corresponding sizes (3-4.5 nm).

particles in the solution shows a slow decreasing pattern with decreasing size. This is caused by the size of the SNPs are not much larger than the critical size. Plot of size distribution (Figure 4.6) illustrates how the size distribution is changing with respect to time. A general pattern of

lower size distribution is seen towards the smaller sizes. A sudden drastic increase in QOR is observed for 3 nm particles which result from small difference in the two sizes present. This is an artifact which is the result of the overlapping size distributions. Although numerically this artifact can be removed by labeling the NPs to specify which distributions are originated from, this indicates the lower limit of how close the size distributions can be placed without interference. Decrease of size results in a slower decrease in supersaturation values, which can be expected based on the decreases of overall surface area of the larger size NPs. The graph also shows that larger size results in larger average size. Small particles dissolve faster and help the larger size grow.

When focusing of NPs takes place, the standard deviation of the NPs gets smaller. Provided that the initial particle (monomer) concentration is high as Talapin`s work pointed out[4], yields fast focusing of size distribution. Therefore, as higher supersaturation values are implemented, the focusing takes place faster and smaller standard values are obtained. In bimodal size distribution, since there are two different sizes, the effect of higher initial number of particles on the size distribution is explored. The simulations are carried out by changing the number of SNPs and large sizes independently. Figure 4.7 left shows the change of standard deviation with respect to number of SNPs while the number of larger size is kept constant. The number of SNPs is varied between $0\text{-}1.6\times10^5$. As more number of initial particles is used, the standard deviation of the larger size gets smaller, therefore better size focusing is achieved. As more monomers are being produced, they will provide the necessary material to the growth of larger particles. Larger size NPs, which has already experienced de-focusing, undergoes a second re-focusing process. In the next simulation (Figure 4.7 right), the number of SNPs is kept constant (8×10^4) and the number of large size is varied from 5×10^2 to 8×10^3. In this case, as

higher number of particles is used, the value of standard deviation reaches a minimum followed by a further increase. To summarize this figure, when there is more SNPs it is advantageous in terms of having focusing but when there are more larger size it will affect the focusing in a reverse way.

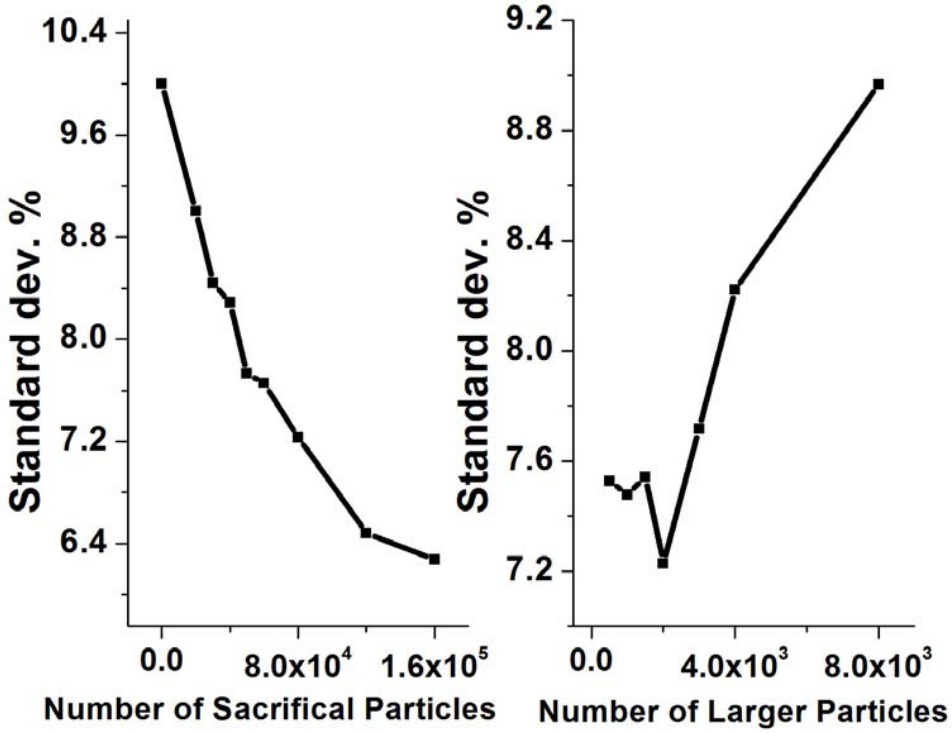

Figure 4.7 Change of standard deviation with addition of different number of particles, left (SNPs), right (larger size)

In hot injection techniques, the precursors are injected rapidly to growth solution to prevent the nucleation as seen in many syntheses.[17, 26, 27] This is done to separate nucleation and growth.[17, 26, 27] In order to examine and compare the re-nucleation rates in this system, re-nucleation rates of multiple injection method to the quantized Ostwald ripening has been calculated given by the following equations;[4]

$$J_N = B_N \exp(-\frac{\Delta G^N}{RT}) \qquad (4.5)$$

$$\Delta G^N = \frac{16\pi\gamma^3 V_m^2}{3(RT\ln S)^2} \qquad (4.6)$$

In these equations, ΔG^N is the activation energy for homogeneous nucleation, B_N represents pre-exponential factor and J_N gives the rate of nucleation. When QOR and MI are compared, the re-nucleation rate is almost 10^4-fold higher for MI (Figure 4.8). Thus, QOR technique yields much lower re-nucleation, so fewer nuclei lead to less polydispersity. Different lines in the figure correspond to different number of initial small particles. Larger number of initial particles results in higher re-nucleation rate. A limit of the applicability of this approach is the solubility of the SNPs in the solution. In order to compare the solubility of NPs used in the simulation to the experimental data, volume fractions of SNPs are calculated. All the calculated

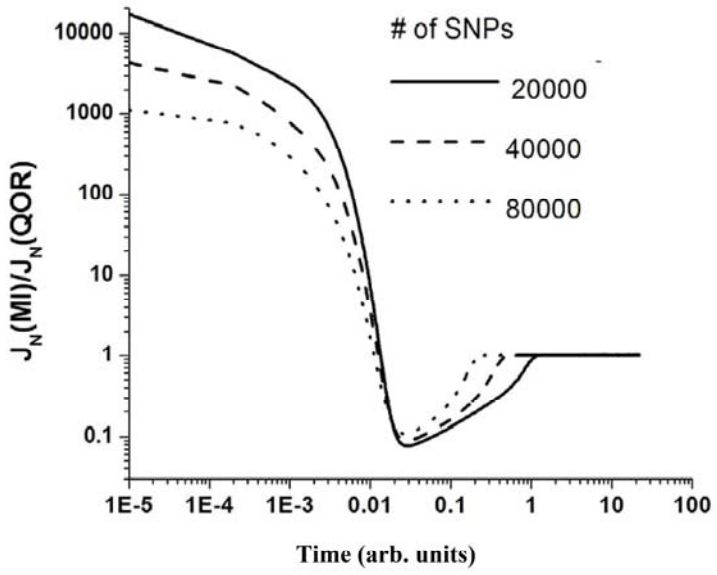

Figure 4.8 Comparison of rate of re-nucleation of MI to the QOR with different initial number of sacrificial particles added.

results from the synthetic data show that solubility used in the simulation is below the solubility limit of typical CdSe NPs in the growth solution. The volume fractions of the NPs calculated are as follows; 0.34×10^{-3} (radius of the NPs is 1 nm)[28], 1.13×10^{-3} (radius of the NPs is 0.8 nm)[29], 2.70×10^{-3} (radius of the NPs is 0.75 nm)[30] and the volume fraction used in the simulation is below 10^{-3} so that diffusional interactions between the neighboring particles can be ignored. As expected the simulation will be sensitive to the surface energy of the particles. The increase in surface energy will result in a faster kinetics and shifts the location of the critical radius. Besides, the specific surface energy value which is used in the overall simulation (0.125 J/m^2), two different values; 0.15 and 0.1 J/m^2 are also implemented into the simulation to investigate the effect of surface energy on the kinetics. The behavior of the standard deviation change in size and the minimum values of standard deviations reached are similar. Only difference is that, with the larger surface energy faster overall growth is observed.

Conclusions

In summary, Monte Carlo simulation of NPs has been carried out to explore the effect of adding SNPs to a larger size. The results show the focusing of size distribution after the addition of smaller size. This focusing is due to the quantized Ostwald ripening. In quantized Ostwald ripening, smaller sized particles from a bimodal size distribution of particles dissolve and larger ones grow similarly to the regular Ostwald ripening which result in focusing of size distribution of larger particles. A key goal in NP synthesis is producing high quality NPs with very narrow size distribution. This has already been achieved by multiple injection techniques experimentally.[7] The difference between multiple-injection and this proposed method is the time required to achieve size focusing. Quantized Ostwald ripening method extends the time for focusing to take place. Therefore, this slower growth will result in less inhomogeneous solution

in a scaled up synthesis especially, in an industrial growth of NPs. In addition, the QOR method reduces the occurrence of re-nucleation process observed mostly in the multiple injection method. It is anticipated that the proposed method can be extended to mix nanoparticles growth solution that are self focusing with a controllable focusing times. This would require the mixing of particles with arbitrary size distributions.

References

1. Marqusee, J. A.; Ross, J., *J. Chem. Phys.* **1983,** 79, (1), 373-378.
2. Oriani, R. A., *Acta Metallurgica* **1964,** 12, (12), 1399-&.
3. Marqusee, J. A.; Ross, J., *J. Chem. Phys.* **1984,** 80, (1), 536-543.
4. Talapin, D. V.; Rogach, A. L.; Haase, M.; Weller, H., *J. Phys. Chem. B* **2001,** 105, (49), 12278-12285.
5. Voorhees, P. W., *J. Stat. Phys.* **1985,** 38, (1-2), 231-252.
6. Tonti, D.; Mohammed, M. B.; Al-Salman, A.; Pattison, P.; Chergui, M., *Chem. Mat.* **2008,** 20, (4), 1331-1339.
7. Peng, X. G.; Wickham, J.; Alivisatos, A. P., *J. Am. Chem. Soc.* **1998,** 120, (21), 5343-5344.
8. Yao, J. H.; Elder, K. R.; Guo, H.; Grant, M., *Phys. Rev. B* **1993,** 47, (21), 14110.
9. De Smet, Y.; Deriemaeker, L.; Finsy, R., *Langmuir* **1997,** 13, (26), 6884-6888.
10. Qu, L. H.; Peng, Z. A.; Peng, X. G., *Nano Lett.* **2001,** 1, (6), 333-337.
11. Dabbousi, B. O.; RodriguezViejo, J.; Mikulec, F. V.; Heine, J. R.; Mattoussi, H.; Ober, R.; Jensen, K. F.; Bawendi, M. G., *J. Phys. Chem. B* **1997,** 101, (46), 9463-9475.
12. Vossmeyer, T.; Katsikas, L.; Giersig, M.; Popovic, I. G.; Diesner, K.; Chemseddine, A.; Eychmuller, A.; Weller, H., *J. Phys. Chem.* **1994,** 98, (31), 7665-7673.

13. Katari, J. E. B.; Colvin, V. L.; Alivisatos, A. P., *J. Phys. Chem.* **1994,** 98, (15), 4109-4117.

14. Reiss, H., *J. Chem. Phys.* **1951,** 19, (4), 482-487.

15. Battaglia, D.; Peng, X., *Nano Lett.* **2002,** 2, (9), 1027-1030.

16. Yang, Y. A.; Wu, H. M.; Williams, K. R.; Cao, Y. C., *Ange Chemie-International Edition* **2005,** 44, (41), 6712-6715.

17. Murray, C. B.; Norris, D. J.; Bawendi, M. G., *J. Am. Chem. Soc.* **1993,** 115, (19), 8706-8715.

18. Wang, H. L.; Ning, D.; Feng, S. L., *J. Cryst. Growth* **2000,** 209, (4), 630-636.

19. Zhao, H. G.; Chaker, M.; Ma, D. L., *J. Phys. Chem. C* **2009,** 113, (16), 6497-6504.

20. Tuinenga, C.; Jasinski, J.; Iwamoto, T.; Chikan, V., *ACS Nano* **2008,** 2, (7), 1411-1421.

21. Fu, M.; Hu, Z. S.; Tang, M.; Wei, X. P.; Shao, M. H.; Li, L. H.; Deng, Y. L., *Chinese J. Chem. Phys.* **2007,** 20, (6), 811-815.

22. Thessing, J.; Qian, J. H.; Chen, H. Y.; Pradhan, N.; Peng, X. G., *J. Amer. Chem. Soc.* **2007,** 129, (10), 2736-+.

23. Ross, F. M.; Tersoff, J.; Tromp, R. M., *Physical Review Letters* **1998,** 80, (5), 984.

24. He, R.; You, X.; Tian, H.; Gao, F.; Cui, D.; Gu, H., *Frontiers of Chemistry in China* **2006,** 1, (4), 378-383.

25. Peng, X. G.; Manna, L.; Yang, W. D.; Wickham, J.; Scher, E.; Kadavanich, A.; Alivisatos, A. P., *Nature* **2000,** 404, (6773), 59-61.

26. Li, L.; Reiss, P., *J. Ame. Chem. Soc.* **2008,** 130, (35), 11588-+.

27. Donega, C. D.; Liljeroth, P.; Vanmaekelbergh, D., *Small* **2005,** 1, (12), 1152-1162.

28. Peng, Z. A.; Peng, X. G., *J. Am. Chem. Soc.* **2002,** 124, (13), 3343-3353.

29. Riehle, F. S.; Bienert, R.; Thomann, R.; Urban, G. A.; Krugert, M., *Nano Lett.* **2009,** 9, (2), 514-518.

30. Bowers, M. J.; McBride, J. R.; Rosenthal, S. J., *J. Am. Chem. Soc.* **2005,** 127, (44), 15378-15379.

CHAPTER 5 - The Effect of In Doping on the Growth Kinetics of CdSe NPs

Semiconductor NPs are subject of vast area of research because of their size-dependent optical properties[1] and their applications ranging from luminescent biolabels[2-5] to solar cells[6-8]. A lot of efforts have been made to study the growth of different sizes[9-12], shapes[13-15] and functionalities[16-18] of semiconductor NPs. Another research area has been focused on the doping[1, 19, 20] of semiconductor NPs. Doping semiconductor NPs is achieved by adding impurities to the semiconductor lattices. Doping leads to changes in electrical conductivity and also has effects on magnetic, optical and fluorescent properties.[1]

Several research attempts have been dedicated to achieve doping and investigate this phenomenon. However, the effects of doping on the growth kinetics have not been investigated thoroughly. A recent study has explored the doping of indium and its effects on the growth kinetics[21] of CdSe NPs by using *in situ* fluorescence spectroscopy. The results of this study[21] reveal the existence of a heterogeneous regime which is very different from conventional NP growth. Heterogeneous growth consists of two different sized CdSe NPs at the same time during the growth. Another important result drawn from this study is the observation that when the dopant agents are introduced, the growth and the dissolution rates of the particles change. Indium dopants activate the magic sized CdSe NPs to further growth. The comparison of the growth rate of doped and undoped NPS revealed that when the percentage of dopants is increased, the growth of NPs is observed to take place faster. Therefore, the incorporation of dopants is not only significant in changing the electronic structure of NPs, but has also proved to have some effects on the growth rate.

Starting from this very important aspect of doping, some exciting results on the *in situ* polarization spectroscopy of magic sized quantum dots and the effect of dopants on growth rate will be presented in this chapter. Adding Indium to the solvent enhances the growth rate so that growth of ~ 500 nm peak forms more rapidly. At 80 ^{0}C, the peak at ~ 500 nm is not observed. According to the time-resolved PL (photoluminescence) data, undoped NPs follow positive anisotropy; however, indium doping results in negative anisotropy.

Experimental Methods

In a fluorescence cuvette, 10 mg of single precursor $Li_4[Cd_{10}Se_4(SPh)_{16}]^{22}$ is mixed with 3 g of HDA (hexadecylamine) to prepare the CdSe NPs. For the In-doped CdSe, the same system and the same amounts of chemicals are used with the exception of the amount of $InCl_3$ used as the dopant. Two different temperature values are used for the growth; 80 ^{0}C, and 120 ^{0}C. This system is kept under nitrogen flow during the reaction.

Time-resolved fluorescence spectroscopy is carried out by using time correlated single photon counting (TCSPC). Excitation pulses are produced from a mode-locked Ti:sapphire laser (17 fs pulse, λ_{max} = 780 nm, average power 60 mW, repetition rate = 2 MHz) pumped by a diode laser (532 nm, 4.6 W). Figure 5.1 shows the simple diagram of the basic components of the experimental setup. The laser pulse is characterized using a home-built autocorrelator with a GaAsP photodiode as the nonlinear medium. The sample is excited by the linearly polarized light coming from a blue light at wavelength of 450 nm. The vertical and the horizontal components of the intensity of the emitted light are measured. The data are used to calculate the anisotropy of the NPs by using parallel and the perpendicular PL decay. During the experiment the 1 cm-thick PL cuvvette is heated to 120 ^{0}C or 80 ^{0}C in a closed box in order to prevent entering of light. The temperature is controlled by using a temperature probe put in the sample cuvvette. In order to

test the alignment of the polarizer, a laser dye (rhodamine 6G) is used to see how the anisotropy is changing at 580 nm. The data show that vertical and the horizontal Pl decays overlap on the measurement of the laser dye.

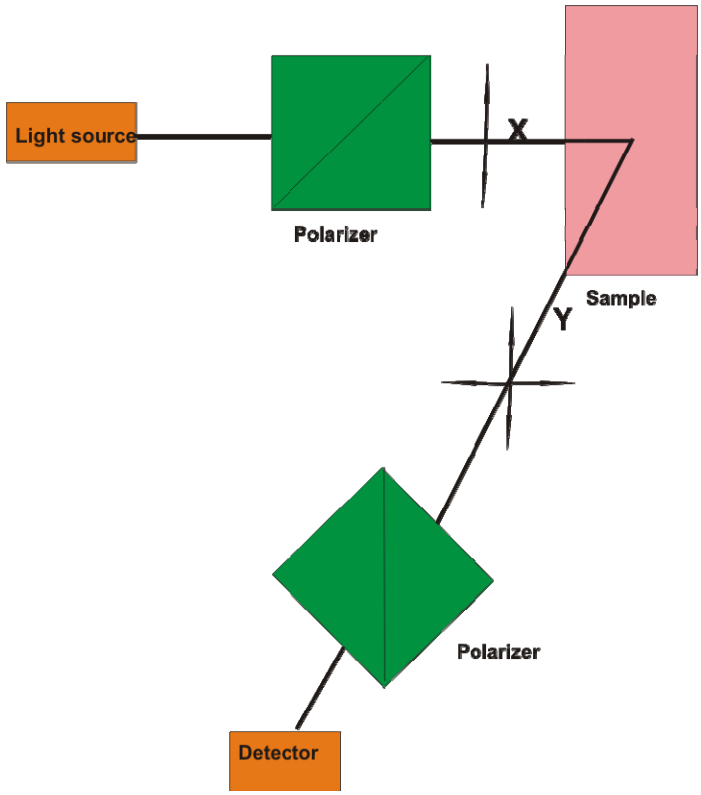

Figure 5.1 Experimental setup used in the time-resolved fluorescence spectroscopy experiments

Results and Discussion

In this study, in order to see the effect of doping and the heterogeneous growth, different time-resolved PL measurements are carried out. Following data present results of different measurements. First, the effect of temperature on the undoped CdSe NPs is investigated. Figure 5.2 shows the static fluorescence of CdSe NPs at a growth temperature of 80 ^{0}C for 6 hours of growth. There is a strong peak at 450 nm, indicating the growth of magic-sized CdSe NPs and

the peak gets more intense and shifts to the red. The data in Figure 5.3 indicate the corresponding time resolved fluorescence spectra after 3 hours and 6 hours. There is an absolute enhancement in the polarized emission versus reaction time as shown by the data in Figure 5.3a and 5.3b

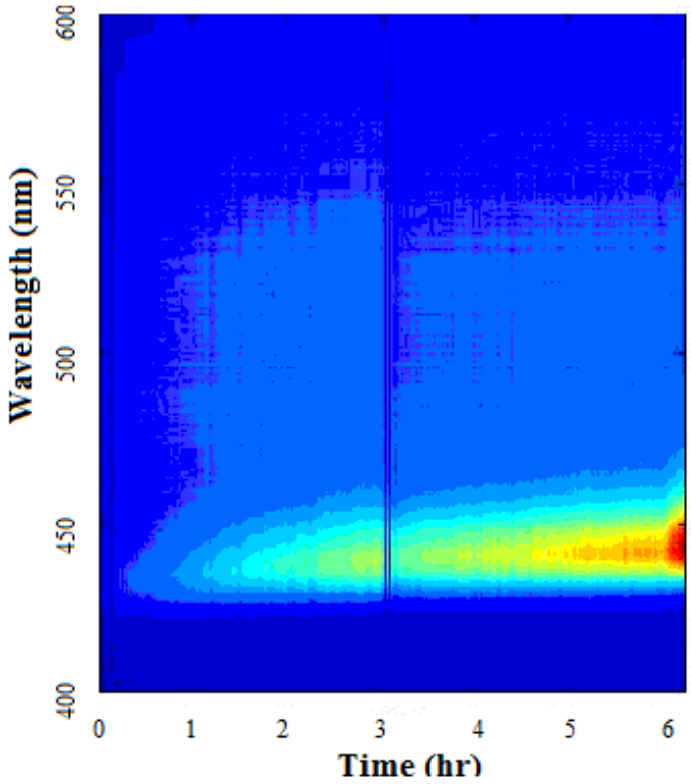

Figure 5.2 Static fluorescence spectra with respect to time at 80 ^{0}C

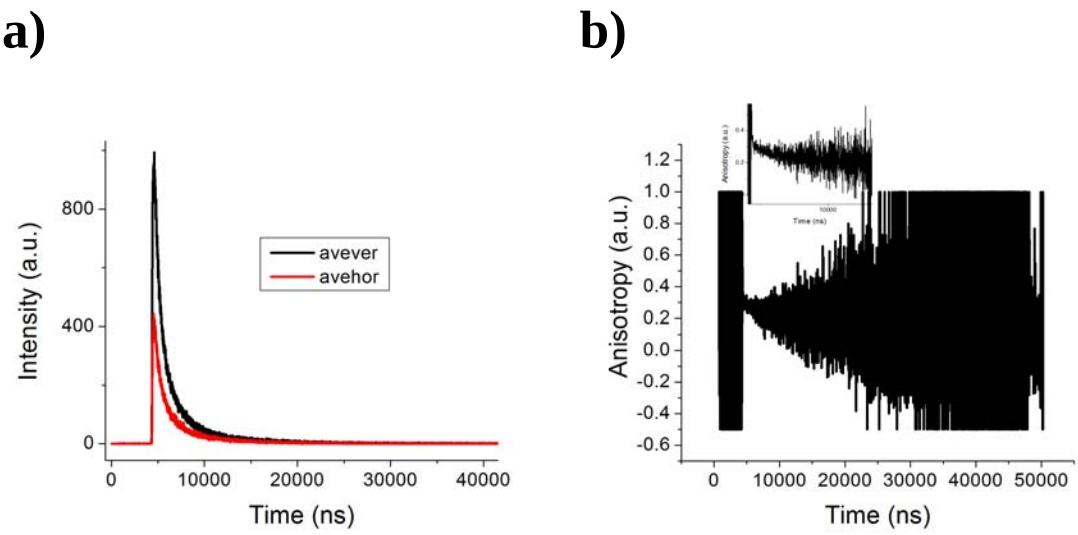

Figure 5.3 a) Time-resolved fluorescence decay taken at 450 nm of undoped CdSe NPs at 80 ^{0}C, b) fluorescence anisotropy of corresponding NPs

Another measurement done besides the static PL study is the time-resolved PL which is done to explore more about this system in terms of the PL decay times. Figure 5.3a presents the parallel and the perpendicular polarization results of the average time resolved fluorescence of the undoped samples at 80 ^{0}C. The polarization experiment indicates a relatively fast decay time. The anisotropy measurement illustrates that the anisotropy is decaying from a value close to 0.4. Since it does not start at exactly 0.4 anisotropy, this result probably shows that the absorption and the emission dipoles are not exactly collinear.

a)

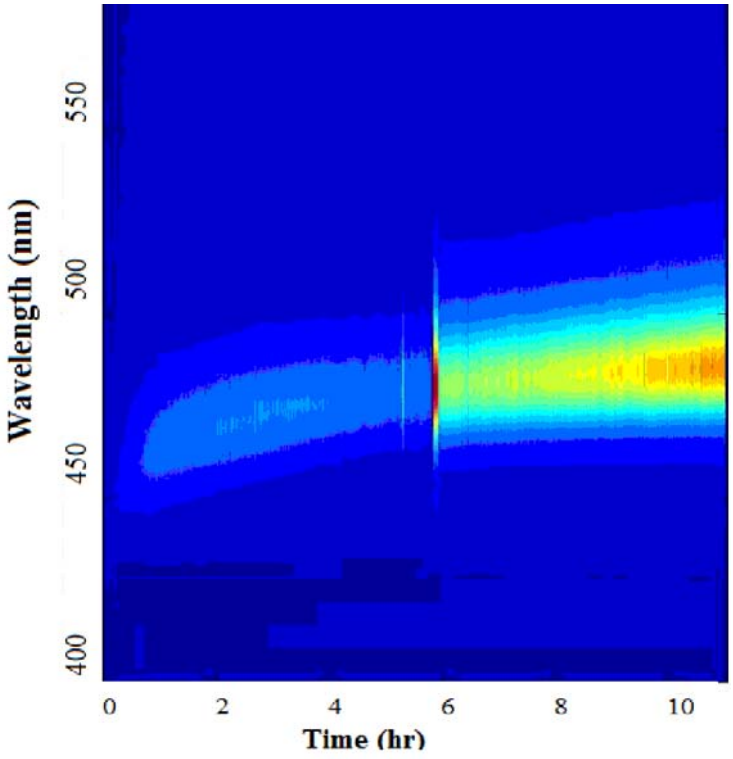

b)

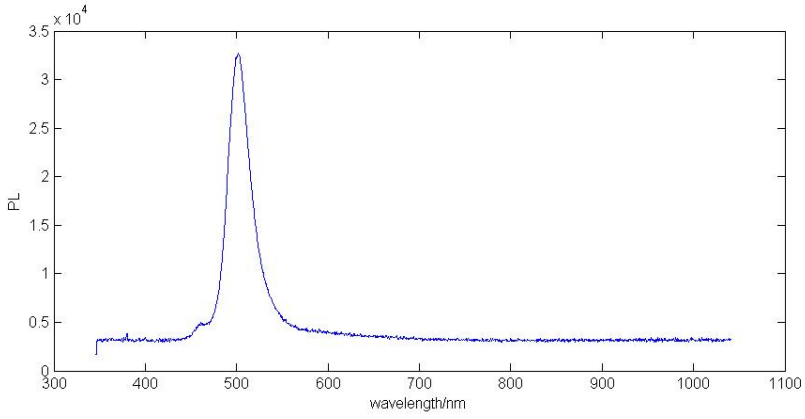

Figure 5.4 a) Static fluorescence spectra with respect to time at 120 ^{0}C for undoped CdSe NPs, b) corresponding last PLspectrum, the shoulder at around 470 is a result of the magic size NPs

After the low temperature experiment, in order to see the effect of temperature increment on growth, the same experiments is carried out at 120 ^{0}C. Figure 5.4 shows the undoped CdSe NPs at a growth temperature of 120 ^{0}C. After around 6 hours the magic sized particles at 450 nm disappear and the next size forms at 490 nm. The small size is believed to provide the required supersaturation necessary for the growth of the 490 nm peak.[21] The difference between the lower temperature and the 120 ^{0}C growth is at 80 ^{0}C just the magic size NPs forms, however, at 120 ^{0}C both small and large sizes form (heterogeneous growth). The heterogeneous growth is different than the normal growth of NPs where there is a constant shift from blue to red. In heterogeneous growth, there is more than one peak formation corresponding to multiple NP sizes and they retain their size for a while.

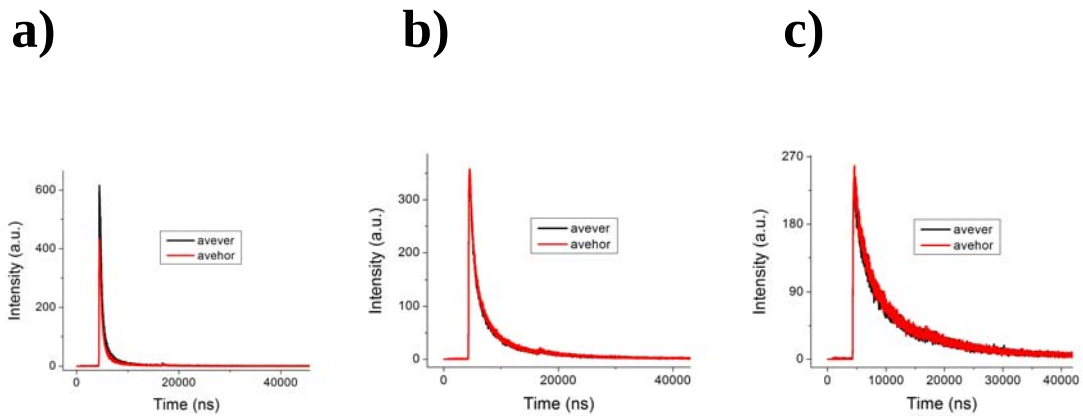

Figure 5.5 Time-resolved fluorescence decay of undoped CdSe NPs at 120 ^{0}C for a) 450 nm peak, b) 470 nm peak, c) 500 nm peak

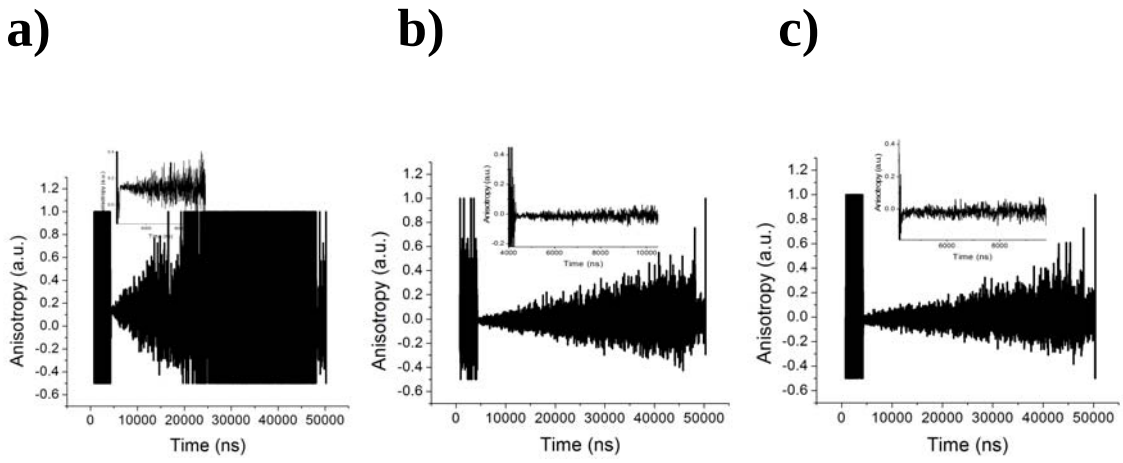

Figure 5.6 Fluorescence anisotropy of corresponding NPs for a) 450 nm peak b) 470 nm peak c) 500 nm peak

During the 120 ^{0}C experiment, firstly, the magic size peak forms and later, the heterogeneous growth generates two different peaks. Figure 5.5 demonstrates the fluorescence decays at different times of the experiment. Figure 5.5a presents the polarization data when a 450 nm filter is used just to see the peak formed at 450 nm (magic size peak). Later, 2 different peaks form and to get the time-resolved fluorescence data for each peak, first a 470 nm filter is used and a 490 nm filter is used to detect the larger size. Figure 5.5b shows the PL decay of just first peak in the presence of the second peak at a longer wavelength value. Figure 5.5c is the corresponding PL decay of 490 nm peak. PL decay time of the larger particles is much slower than the magic size peak. This phenomenon is a result of the surface defects of the larger particles. Due to the trapping of electrons at lower energy states, the PL decay time increases. On the other hand, the intensity of the 490 peak is more than the magic size peak. However, when there is only one peak due to the magic size (Figure 5.4a), the intensity of the peak is more than the peak in the presence of the heterogeneous growth. Another important observation is the anisotropies of these different peaks (Figure 5.6). When only the magic size peak at 450 nm is

present, different parallel and the perpendicular emissions are observed (Figure 5.5a), which results in a nonzero anisotropy (Figure 5.6a). However, as the Figures 5.5b and c indicate, the values of the parallel and the perpendicular polarization do not differ remarkably and the anisotropy values average to zero (Figure 5.6b and c).

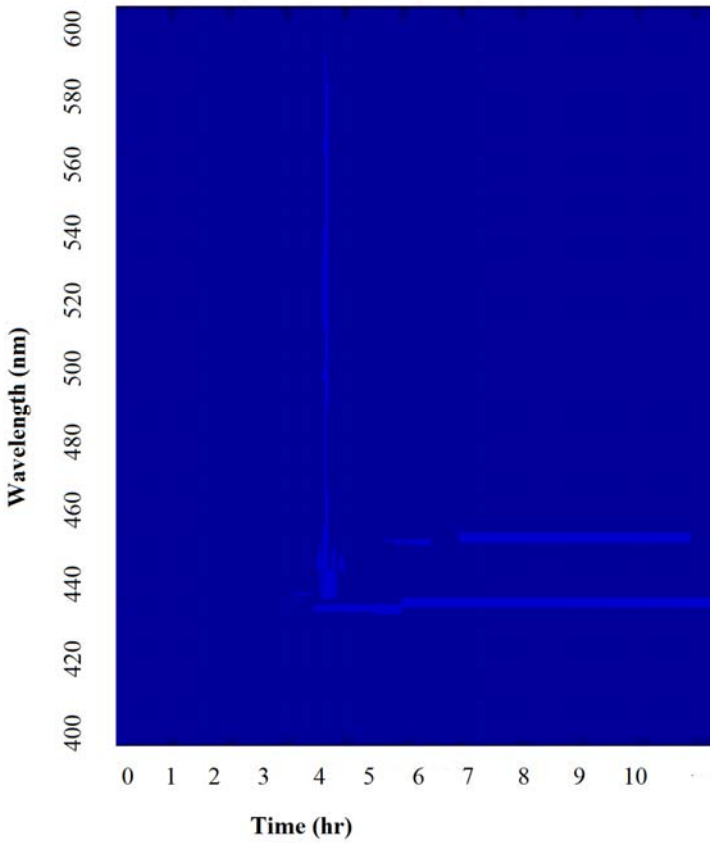

Figure 5.7 Static fluorescence spectra with respect to time at 80 ^{0}C for In-doped CdSe NPs at 450 nm

After the investigation of PL of undoped CdSe NPs, in order to see the dopant effect, the experiments are carried out by the addition of In as the dopant. Figure 5.7 shows the formation of magic sized CdSe NPs upon the addition of In dopants. As in the undoped 80 ^{0}C synthesis, only the peak at around 450 nm forms. Upon addition of In as shown in Figure 5.7, the intensity

of the fluorescence decreases remarkably. Therefore, the addition of In decreases the emission of magic sized CdSe NPs as reported[21] before.

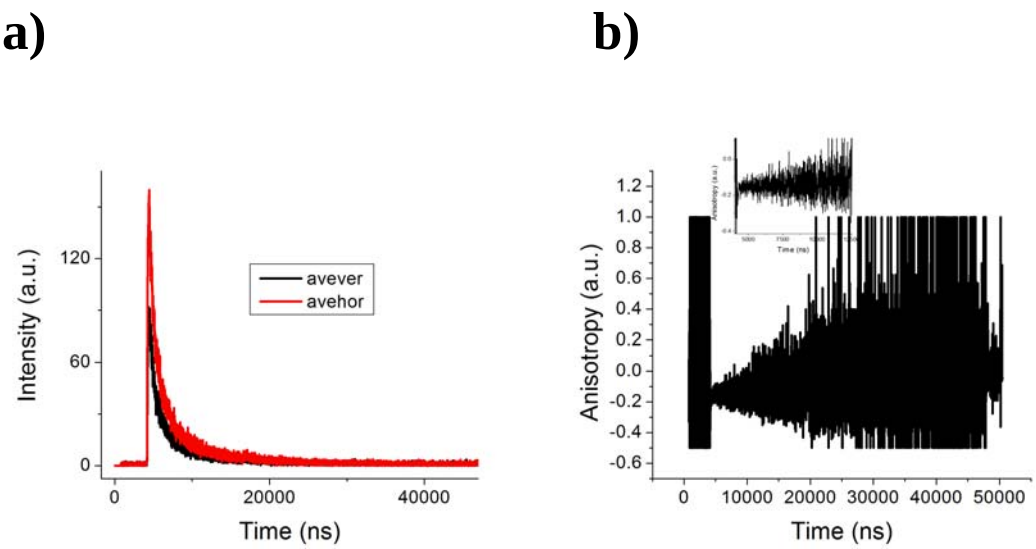

Figure 5.8 a) PL decay of In-doped CdSe NPs at 80 ^{0}C, b) corresponding anisotropy measurement

The effect of addition of In dopant on the time-resolved fluorescent decay is shown in Figure 5.8a and b is the corresponding anisotropy. The intensity is remarkably lower than the undoped 80 ^{0}C experiment (Figure 5.3a, 8a) which is due to the defects caused by the addition of In to the surface of NPs. The decay lifetime of perpendicular emission is shorter than the parallel emission (Figure 5.8a), which leads a negative anisotropy value (Figure 5.8b).

a)

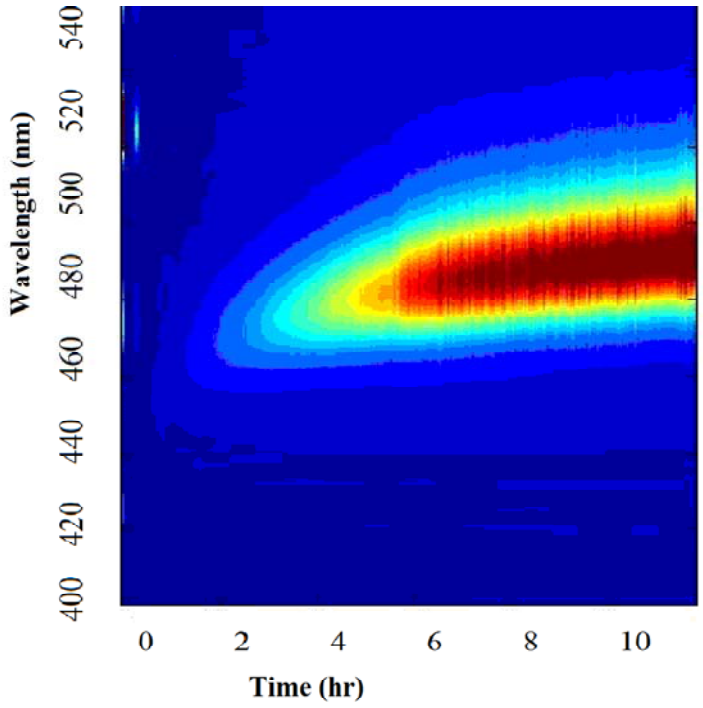

b)

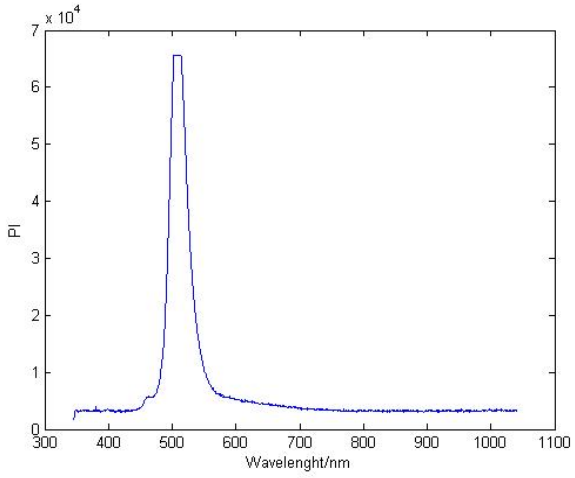

Figure 5.9 a) Static fluorescence spectra with respect to time at 120 ^{0}C for In-doped CdSe NPs, and b) the corresponding last Pl spectrum

As in the undoped PL measurement, in order to see the effect of temperature increment on growth, the PL experiments are carried out at 120 ^{0}C for the In-doped CdSe NPs. Figure 5.9 presents the static fluorescence spectra upon addition of In to CdSe NPs at 120 ^{0}C. The effect of In on growth can be seen here. The emission maximum at 490 nm is reached after 6 hours of growth. On the other hand, as Figure 5.4a indicates, without the In dopant, the development of the 490 nm peak takes a longer time (more than 8 hours). Thus, these results demonstrate that the addition of dopants enhances the growth rate. Figure 5.4b presents the last spectrum taken during the growth. As the last static PL spectrum of doped (Figure 5.9b) and undoped (Figure 5.4b) CdSe NPs are compared, In doping also improves the fluorescence if the system is kept long enough to the decrease of the defect formation.

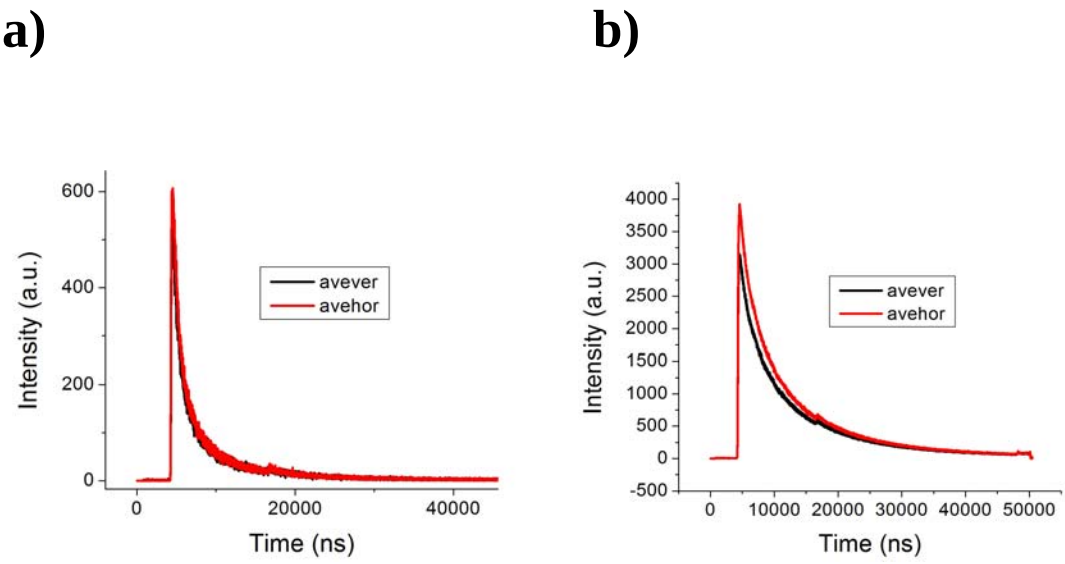

Figure 5.10 Time-resolved fluorescence decay of In-doped CdSe NPs at 120 ^{0}C for a) 470 nm peak b) 500 nm peak

a) **b)**

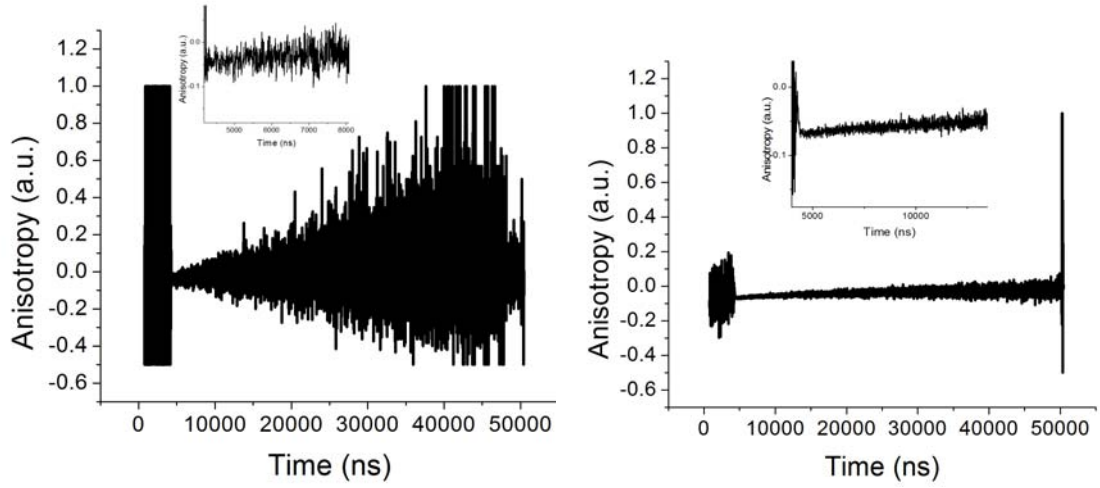

Figure 5.11 Fluorescence anisotropy of corresponding NPs for a) 470 nm peak b) 500 nm peak

The addition of dopants leads to different phenomena on the time-resolved spectra of CdSe NPs at 120 ^{0}C. One thing observed for undoped experiment at 120 ^{0}C is due to the overlapping values of parallel and the perpendicular polarization emissions (Figure 5.5b, c), the anisotropy is around a zero value. However, when In dopant is incorporated, the perpendicular emission follows a more rapid decay than the parallel one. As a result of the larger value of perpendicular decay, a negative anisotropy results for the 500 nm peak (Figure 5.11a and b) that is most likely due to supperlatice formation of magic-sized NPs.

Conclusions

Time-resolved fluorescence and static fluorescence experiments are carried out to explore the heterogeneous growth regime with and without the addition of In dopants. The results led to the following conclusions: (1) during the low temperature synthesis at 80 ^{0}C, the heterogeneous growth regime is not observed, magic size CdSe NPs is formed at around 460 nm; (2) upon

heating the NP solution to a higher temperature, 120 ^{0}C, the heterogeneous regime emerges and two distinct sizes at around 460 nm and 500 nm appear: (3) the dopants have an effect of accelerating the reaction: (4) as the time-resolved PL data demonstrate, undoped NPs follow the usual positive anisotropy: however, In doping results in negative anisotropy. In the future, the study will be expanded on different dopants such as, gallium, and tin. There will be more studies to explore more on this area since this is an on-going project.

References

1. Bryan, J. D.; Gamelin, D. R., Doped Semiconductor Nanocrystals: Synthesis, Characterization, Physical Properties, and Applications. In *Progress in Inorganic Chemistry, Vol 54*, John Wiley & Sons Inc: New York, 2005; Vol. 54, pp 47-126.

2. Chan, W. C. W.; Nie, S. M., Quantum dot bioconjugates for ultrasensitive nonisotopic detection. *Science* **1998,** 281, (5385), 2016-2018.

3. Quarta, A.; Ragusa, A.; Deka, S.; Tortiglione, C.; Tino, A.; Cingolani, R.; Pellegrino, T., Bioconjugation of Rod-Shaped Fluorescent Nanocrystals for Efficient Targeted Cell Labeling. *Langmuir* **2009,** 25, (21), 12614-12622.

4. Fan, J. Y.; Li, H. X.; Iiang, J.; So, L. K. Y.; Lam, Y. W.; Chu, P. K., 3C-SiC nanocrystals as fluorescent biological labels. *Small* **2008,** 4, (8), 1058-1062.

5. Lee, J.; Kim, J.; Park, E.; Jo, S.; Song, R., PEG-ylated cationic CdSe/ZnS QDs as an efficient intracellular labeling agent. *Physical Chemistry Chemical Physics* **2008,** 10, (13), 1739-1742.

6. Huynh, W. U.; Dittmer, J. J.; Alivisatos, A. P., Hybrid nanorod-polymer solar cells. *Science* **2002,** 295, (5564), 2425-2427.

7. Thanachayanont, C.; Inpor, K.; Sahasithiwat, S.; Meeyoo, V., MEH-PPV/CdS nanorod polymer solar cells. *Journal of the Korean Physical Society* **2008,** 52, (5), 1540-1544.

8. Alivisatos, A. P., Hybrid-nanorod polymer solar cells. *Abstracts of Papers of the American Chemical Society* **2004,** 227, 060-IEC.

9. Rogach, A. L.; Talapin, D. V.; Shevchenko, E. V.; Kornowski, A.; Haase, M.; Weller, H., Organization of matter on different size scales: Monodisperse nanocrystals and their superstructures. *Advanced Functional Materials* **2002,** 12, (10), 653-664.

10. Trindade, T.; O'Brien, P.; Pickett, N. L., Nanocrystalline semiconductors: Synthesis, properties, and perspectives. *Chemistry of Materials* **2001,** 13, (11), 3843-3858.

11. El-Sayed, M. A., Small is different: Shape-, size-, and composition-dependent properties of some colloidal semiconductor nanocrystals. *Accounts of Chemical Research* **2004,** 37, (5), 326-333.

12. El-Sayed, M. A., Some interesting properties of metals confined in time and nanometer space of different shapes. *Accounts of Chemical Research* **2001,** 34, (4), 257-264.

13. Manna, L.; Milliron, D. J.; Meisel, A.; Scher, E. C.; Alivisatos, A. P., Controlled growth of tetrapod-branched inorganic nanocrystals. *Nat Mater* **2003,** 2, (6), 382-385.

14. Manna, L.; Scher, E. C.; Alivisatos, A. P., Synthesis of soluble and processable rod-, arrow-, teardrop-, and tetrapod-shaped CdSe nanocrystals. *J. Am. Chem. Soc.* **2000,** 122, (51), 12700-12706.

15. Kumar, S.; Nann, T., Shape control of II-VI semiconductor nanomateriats. *Small* **2006,** 2, (3), 316-329.

16. Mokari, T.; Sztrum, C. G.; Salant, A.; Rabani, E.; Banin, U., Formation of asymmetric one-sided metal-tipped semiconductor nanocrystal dots and rods. *Nature Materials* **2005,** 4, (11), 855-863.

17. Salgueirino-Maceira, V.; Correa-Duarte, M. A., Increasing the complexity of magnetic core/shell structured nanocomposites for biological applications. *Advanced Materials* **2007,** 19, (23), 4131-4144.

18. Li, X. L.; Liu, Y. Q.; Fu, L.; Cao, L. C.; Wei, D. C.; Wang, Y., Efficient synthesis of carbon nanotube-nanoparticle hybrids. *Advanced Functional Materials* **2006,** 16, (18), 2431-2437.

19. Mikulec, F. V.; Kuno, M.; Bennati, M.; Hall, D. A.; Griffin, R. G.; Bawendi, M. G., Organometallic synthesis and spectroscopic characterization of manganese-doped CdSe nanocrystals. *Journal of the American Chemical Society* **2000,** 122, (11), 2532-2540.

20. Yang, P.; Lu, C.; Hua, N. P.; Du, Y. K., Titanium dioxide nanoparticles co-doped with Fe3+ and Eu3+ ions for photocatalysis. *Materials Letters* **2002,** 57, (4), 794-801.

21. Tuinenga, C.; Jasinski, J.; Iwamoto, T.; Chikan, V., In situ observation of heterogeneous growth of CdSe quantum dots: Effect of indium doping on the growth kinetics. *Acs Nano* **2008,** 2, (7), 1411-1421.

22. Roy, S.; Tuinenga, C.; Fungura, F.; Dagtepe, P.; Chikan, V.; Jasinski, J., Progress toward Producing n-Type CdSe Quantum Dots: Tin and Indium Doped CdSe Quantum Dots. *Journal of Physical Chemistry C* **2009,** 113, (30), 13008-13015.

Appendix A - Simulation Code of Aggregation Dynamics

Following is the code used to simulate the aggregation of NPs written on matlab from chapter 3.

```
function [ output_args ] = Simulation( input_args )
% constants
T=512; %Temperature;
nu=0.001% viscosity in Kgm-1s-1
kb=1.3806503E10-23% Boltzmann constant m2Kgs-2K-1
Dpre=T*kb/(6*pi*nu*1E+9);
V_monomer=4.1E-5;% volume of the monomer
Monomer_solubility=0.005;% solubility of the monomer in mol/L
Simulated_volume=0.6E-14;
width=0.05;%width of the intial distribution
av_size=1.5;% avergae size of initial distribution
S=900;%supersaturation
K=0.001;
alpha=0.5;
dt=2E-5;%time step
number_of_particles=40000;



%creating new window
h=figure;
```

```
set(h,'Position',[20,100, 400, 400] );


%Generation inital distribution
r = randn(number_of_particles,1)*width+av_size;

%calculation of the nanoparticle volumes
V=round((4/3)*r.^3*pi()/V_monomer);% Vi is the volume of the nanoparticles in terms of monomer number

% calculating free monomers in solution
monomer_number_in_solution=S*Simulated_volume*Monomer_solubility*6E23;
monomer_number_in_particles=sum(V);
total_monomer_number=monomer_number_in_particles+monomer_number_in_solution;

%plotting initial distribution
 subplot(2,1,1)
 hist(r,80);
 title('Size histogram');
 xlim([0 10]);
 xlabel('r size in nm');

%Plotting dr/dt , the growth rate
```

```
plotrate=[];
plotratex=[];
for i=0.2:0.05:5
    plotrate=[plotrate; (S-exp(1/i))/(i+K*exp(alpha/i))];
    plotratex=[plotratex; i];
end
subplot(2,1,2);
h=plot(plotratex, plotrate);
ylim([-5 100]);
title('dr/dt');
xlabel('r size in nm');

%creating new window for the rest of the simulation
h=figure;
set(h,'Position',[450,100, 700, 400] );
refresh(h);

%initializing the first value for the time dependant quantities
 time=[0];
 S_time=[S];
 Average_size_time=[av_size];
 Size_dist_time=[width];
 V_time=[Simulated_volume];
```

```
 n_time=[0,0,0,0];
% n_time=n_time';

%creating bin vector x in V (nm3)
bin_size=400;
for j=1:bin_size
   x(j)=j*0.25;
end

%initializing correction for aggregation population
n_corr=zeros(1,bin_size);

%creating bin vector in r(nm)
x_r=((3/4)*x/pi).^(1/3);


%creating in vector in lambda
x_lambda=(2*x_r-1.38435)./(0.00121*2*x_r-0.00066);

%initilizing arrays for time depedant qunatities
Dist_time(:,1)=x;
Monomergrowth_rate_time(:,1)=x;
Agg_rate_time(:,1)=x;
```

```
%types of calculation type=1,2,3 1:Brownian 2:Orineted attachment 3:Average dipole
type=1;

%D vector for various nanoparticles
for i=1:bin_size
   D(i)=Dpre/x_r(i);
end

%calculating q matrix
q=zeros(bin_size,bin_size);

for k=1:bin_size
      for i=1:bin_size
         if(type==1)
         q(i,k)=4*pi*(D(i)+D(k))*(x_r(i)+x_r(k))*1E-9;
         elseif (type==2)
         q(i,k)=4*pi*(D(i)+D(k))*(x_r(i)+x_r(k))*1E-9/Wo(x_r(i),x_r(k),T);
         elseif (type==3)
         q(i,k)=4*pi*(D(i)+D(k))*(x_r(i)+x_r(k))*1E-9/Wa(x_r(i),x_r(k),T);
         end;
      end
```

```
end

%making string matrix for info file
str1=['Temperature=',num2str(T),' K'];
str2=['Average size=',num2str(av_size),'+-',num2str(width),' nm'];
str3=['S=',num2str(S)];
str4=['K=',num2str(K)];
str5=['# of particles=',num2str(number_of_particles)];
str6=['alpha=',num2str(alpha)];
str7=['dt=',num2str(dt)];
str8=['type of calculation=',num2str(type)];
string_info=strvcat(str1,str2,str3,str4,str5,str6,str7,str8);

%%%%%%%%%%%%%%%%%%%%%%%%%%%%%%%%%%%%%%%%%%%%%%%%
%%%%%%%%%%%%%%%%%%%%%%%%%%%%%%%%%%%%%%%%%%%%%%%%
%%%%%%%%%%%%%%%%%%%%%%%%%%%%%%%%%%%%%%%%%%%%%%%%

%Simulation starts here
 for j=1:2000
    str2 = num2str(j);
    %plotting S
    subplot(3,3,1);
    plot(time,S_time);
```

```
str3=['i=', str2,' th step'];
Title(str3);
xlabel('Time');
ylabel('S');

%plotting average size dist
subplot(3,3,4);
plot(time,Average_size_time);
title('Average Size');
xlabel('Time');

%plotting average size
subplot(3,3,7);
plot(time,Size_dist_time);
title('Size distribution');
xlabel('Time');
drawnow;

%%%
```

```
r=[];
rate=[];
r=((3/4)*V*V_monomer/pi).^(1/3);
for i=1:length(r)
   if r(i)>0
    rate(i)=4*r(i)^2*pi*(4/3)*pi*(S-exp(1/r(i)))/(r(i)+K*exp(alpha/r(i)))^3;
   else
    rate(i)=0;
   end
end

% calculating new V (# of monomers/particle)
dV=[];
 % calculating  dV
dV=(rate*dt/V_monomer);

for i=1:size(V)
   if V(i)+dV(i)>0
   V(i)=V(i)+dV(i);
   else
   V(i)=0;
   end
end
```

```
%removing zeros from matrix
[i_row j_col]=find(V>0);
V=V(i_row,1);

%calculating r again for the average dist and std
r=((3/4)*V*V_monomer/pi).^(1/3);

% change in monomer #
monomer_number_in_solution=total_monomer_number-sum(V);

%plotting rate due to monomer exchange
rate=[];
for i=1:bin_size
   rate(i)=4*x_r(i)^2*pi*(4/3)*pi*(S-exp(1/x_r(i)))/(x_r(i)+K*exp(alpha/x_r(i)))^3;
end
subplot(3,3,[5 6]);
title('dV histogram');
dV=(rate*dt/V_monomer);
plot(x',dV);
xlim([0 200]);
xlabel('size in nm3');
ylabel('change in monomer #');
```

```
  Monomergrowth_rate_time(:,j+1)=dV;

  drawnow;


  % Calculating new S

  S=monomer_number_in_solution/(Simulated_volume*Monomer_solubility*6E23);


  time=[time;time(j)+dt];

  S_time=[S_time;S];

  Average_size_time=[Average_size_time; mean(r)];

  Size_dist_time=[Size_dist_time; std(r)];


%%%%%%%%%%%%%%%%%%%%%%%%%%%%%%%%%%%%%%%%%%%%%

%%%%%%%%%%%%%%%%%%%%%%%%%%%%%%%%%%%%%%%%%%%%%

%%%%%%%%%%%%%%%%%%%%%%%%%%%%%%%%%%%%%%%%%%%%%

  V_try=V*V_monomer;

  [n V_agg]=hist(V_try,x);


  %plotting sizedistribution in terms of nanoparticle volume in nm3


  subplot(3,3,[2 3]);

  title('Size histogram');

  hist(V_try,x);

  xlim([0 200]);
```

```
xlabel('size in nm3');
[d1 d2]=hist(V_try,x);
Dist_time(:,j+1)=d1;
drawnow;

%calculating second term: sum q(i,k)*n(i)
diss_vector=n*q;

%intializing dndt
dndt=zeros(bin_size,1);

%rate for aggregation
for k=1:bin_size
    for i=1:k-1
        dndt(k)=dndt(k)+q(k-1,i)*n(i)*n(k-i);
    end
    dndt(k)=0.5*dndt(k)-n(k)*diss_vector(k);
end
dn=dndt*dt*0;

Agg_rate_time(:,j+1)=dn;

%correcting for the rounding error
```

```
    n=n+dn'+n_corr;

    %recording changes in total particle number, volume, changes in particle volume, statitsical
error
    sums=[sum(n),sum(V),sum(dn),sum(n_corr)];
    n_time=[n_time;sums];

    %plotting aggregation rate
    subplot(3,3,[8 9]);
    plot(x,dn);
    xlabel('size in nm3');
    ylabel('dn/dt');
    drawnow;

    %generating new size distribution
    new_dist=[];
    for i=1:bin_size
        sizen=round((n(i)));
        if (sizen<=0)
        else
            for k=1:sizen
                %devision factor of rand depends on the bin size for bin size=
                %1 is rand(1,1)-0.5
```

```
            new_dist=[new_dist; x(i)+rand(1,1)/4-0.125];
        end
    end
end

%new volume histogram
[n_new V_agg]=hist(new_dist,x);

%calculating statistical error
n_corr=n-n_new;

%adjusting monomer volume and monomer number for the new statistics
old_monomer_number=sum(V);
new_dist_monomer=new_dist/V_monomer;
V=new_dist_monomer;
new_monomer_number=sum(V);
correction_factor=new_monomer_number/old_monomer_number;

%correcting for statitical errors
Simulated_volume=Simulated_volume*correction_factor;
total_monomer_number=total_monomer_number*correction_factor;
dt=dt*correction_factor;
```

```
    %recalculating monomer # in solution
    monomer_number_in_solution=S*(Simulated_volume*Monomer_solubility*6E23);

    %recording change in Simulated Volume
    V_time=[V_time; Simulated_volume];

    %changing time step in the middle of the run
    %if (j==100) dt=dt*10; end%changing time resolution during simulation
end

%saving time dependant quantities

save('C:\Users\Viktor Chikan\Desktop\data\Dist_time.txt','Dist_time','-ASCII','-double','-tabs');
save('C:\Users\Viktor Chikan\Desktop\data\Monomergrowth_rate_time.txt','Monomergrowth_rate_time','-ASCII','-double','-tabs');
save('C:\Users\Viktor Chikan\Desktop\data\Agg_rate_time.txt','Agg_rate_time','-ASCII','-double','-tabs');
save('C:\Users\Viktor Chikan\Desktop\data\S_time.txt','S_time','-ASCII','-double','-tabs');
save('C:\Users\Viktor Chikan\Desktop\data\Average_size_time.txt','Average_size_time','-ASCII','-double','-tabs');
save('C:\Users\Viktor Chikan\Desktop\data\Size_dist_time.txt','Size_dist_time','-ASCII','-double','-tabs');
```

```
save('C:\Users\Viktor Chikan\Desktop\data\V_time.txt','V_time','-ASCII','-double','-tabs');
save('C:\Users\Viktor Chikan\Desktop\data\time.txt','time','-ASCII','-double','-tabs');
save('C:\Users\Viktor Chikan\Desktop\data\n_time.txt','n_time','-ASCII','-double','-tabs');
x_r=x_r';
x_lambda=x_lambda';
save('C:\Users\Viktor Chikan\Desktop\data\x_r.txt','x_r','-ASCII','-double','-tabs');
save('C:\Users\Viktor Chikan\Desktop\data\x_lambda.txt','x_lambda','-ASCII','-double','-tabs');
save('C:\Users\Viktor Chikan\Desktop\data\info.txt','string_info');

k=0;
h=0;
```

Average Dipole Function

```
function
y = Wa(c1,c2)
T=512;
nu=1*100*3.33E-30;
e0=8.854E-12;
k=1.380E-23;
ai=c1*1E-9;
aj=c2*1E-9;
F=@(r) (ai+aj)*exp(-2*nu^4./(r.^6*(k*T)^2*48*pi^2*e0^2))./r.^2;
y =quad(F,ai+aj,1E-2,1E-10);
```

```
end
```

Oriented Attachment Function

```
function y = Wo(c1,c2)

T=512;

nu=1*100*3.33E-30;

e0=8.854E-12;

k=1.380E-23;

ai=c1*1E-9;

aj=c2*1e-9;

F=@(r) (ai+aj)*exp(-nu^2./((2*pi*e0.*r).*(r+2*ai).*(r+2*aj)*k*T))./r.^2;

y =quad(F,ai+aj,1E-1,1E-10);

end
```

Appendix B - Simulation Code of Quantized Ostwald Ripening

Following is the code used to simulate the NP growth written on matlab from chapter 4.

```
function [ output_args ] = magic( input_args )
% constants
%%%%%%%%%%%%%%%%%%%%%%%%%%%%%%
T=573; %Temperature K;
kb=1.3806503E10-23;% Boltzmann constant m2Kgs-2K-1
R=8.314472; % gas constant in J/K mol
se=0.1;%specific surface energy J/m2
V_monomer=3.29E-5;%volume of the monomer in m3
Monomer_solubility=0.01;% solubility of the monomer in mol/m3
Simulated_volume=3E-18;%m3
S=1;% intial supersaturation
S=1+2*se*V_monomer/R/T/1E-9;
K=0.001;%K=0.001 is diffusion control K=1000 is reaction control
alpha=0.5;
dt=0.0002;%time step
monomer_number=S*Simulated_volume*Monomer_solubility*6.022E23;% calculating free monomers in solution
F1=R*T/(2*se*V_monomer); %converting dimensionless radius to radius
%%%%%%%%%%%%%%%%%%%%%%%%%%%%%%%

%Defining initaldistributions
```

```
%%%%%%%%%%%%%%%%%%%%%%%%%%%%%%%
average_size1=1;%size 1
nofsize1=40000;
sizedist1=0.1;
average_size2=3.5;%size2
nofsize2=2000;
sizedist2=0.35;
threshold=(average_size1+average_size2)/2;% for calculating statistical data where to spearate the sizes
%%%%%%%%%%%%%%%%%%%%%%%%%%%%%%%

%Generation inital distributions
%%%%%%%%%%%%%%%%%%%%%%%%%%%%%%%%
r1 = normrnd(0,sizedist1,nofsize1,1)+average_size1;
r2 = normrnd(0,sizedist2,nofsize2,1)+average_size2;
r=[r1; r2];%combining r1 and r2
x=0:0.05:8;%bin vector for histogram
[n x]=hist(r,x);%histogram of inital distribution
r=r/1E9;
%%%%%%%%%%%%%%%%%%%%%%%%%%%%%%%%%

%calculation of the nanoparticle volumes
%%%%%%%%%%%%%%%%%%%%%%%%%%%%%%%%%%%%%%%%
```

```
V=6.022E23*(4/3)*r.^3*pi()/V_monomer;% V is the volume of the nanoparticles in terms of monomer number
sum(V)*V_monomer/6.022E23
r=r*F1;%converting radius to dimensionless radius (r*)
%%%%%%%%%%%%%%%%%%%%%%%%%%%%%%%%%%%%%%%%


%Calculating S for repeated injection
%%%%%%%%%%%%%%%%%%%%%%%%%%%%%%%%%%%%%%%
r1=r1/1E9;
V1=6.022E23*(4/3)*r1.^3*pi()/V_monomer;
monomer_number_in_magic_size=sum(V1);
magic_S=monomer_number_in_magic_size/(Simulated_volume*Monomer_solubility*6E23);% Corresponding to magic size
repeated_injection_S=magic_S+S
%%%%%%%%%%%%%%%%%%%%%%%%%%%%%%%%%%%%%%%

%Initializing time depedant arrays to save data
%%%%%%%%%%%%%%%%%%%%%%%%%%%%%%%%
Vnew=[];
t=0;
t_time=t;
S_time=S;
```

```
N_time=nofsize1+nofsize2;
r1std_time=(sizedist1/average_size1)*100;
r1mean_time=[average_size1];
r2std_time=(sizedist2/average_size2)*100;
r2mean_time=[average_size2];
hist_time=[n];
%%%
```

```
% calculating  dr
%%%%%%%%%%%%%%%%%%%%%%%%%%%%%%%%%%
dr=rate*dt;
%%%%%%%%%%%%%%%%%%%%%%%%%%%%%%%%%%

%calculating new size after growth
%%%%%%%%%%%%%%%%%%%%%%%%%%%%%%%%%%
for i=1:size(r)
    if (r(i)+dr(i))>0
    r(i)=r(i)+dr(i);
    else
    r(i)=0;
    end
end
%%%%%%%%%%%%%%%%%%%%%%%%%%%%%%%%%%

%removing zeros from r
%%%%%%%%%%%%%%%%%%%%%%%%%%%%%%%%%%
r = r(r ~= 0);
%%%%%%%%%%%%%%%%%%%%%%%%%%%%%%%%%%

%calculating regular r from r*
%%%%%%%%%%%%%%%%%%%%%%%%%%%%%%%%%%
```

```
    rregular=(r/F1);
    rregular = rregular(rregular ~= 0);
    %%%%%%%%%%%%%%%%%%%%%%%%%%%%%%%%%%%


    % calculating new V (# of monomers/particle)


%%%%%%%%%%%%%%%%%%%%%%%%%%%%%%%%%%%%%%%%%%%%%%%
%%%%%%%
        Vnew=6.022E23*((4/3)*pi()*rregular.^3/V_monomer);


%%%%%%%%%%%%%%%%%%%%%%%%%%%%%%%%%%%%%%%%%%%%%%%
%%%%%%%


    % change in monomer #
    %%%%%%%%%%%%%%%%%%%%%%%%%%%%%%%%%%%%%
    change=sum(V)-sum(Vnew);
    V=Vnew;
    monomer_number=monomer_number+change;
    %%%%%%%%%%%%%%%%%%%%%%%%%%%%%%%%%%%%%%


    % Calculating new S
```

```
%%%%%%%%%%%%%%%%%%%%%%%%%%%%%%%%%%%%%%%%%%%%%%
%%%%%%%%%%%%%%
    S=monomer_number/(Simulated_volume*Monomer_solubility*6E23);
    S_time=[S_time S];

%%%%%%%%%%%%%%%%%%%%%%%%%%%%%%%%%%%%%%%%%%%%%%
%%%%%%%%%%%%%%

    %calculating statistical data
    %%%%%%%%%%%%%%%%%%%%%%%%%%%%%%%%%%%%%%%%%%
    rregular= rregular*1E9;
    rregular1=rregular(rregular <= threshold);
    rregular2=rregular(rregular > threshold);
    r1mean=mean(rregular1);
    r1std=100*std(rregular1)/r1mean;
    r2mean=mean(rregular2);
    r2std=100*std(rregular2)/r2mean;
    r1mean_time=[r1mean_time r1mean];
    r1std_time=[r1std_time r1std];
    r2mean_time=[r2mean_time r2mean];
    r2std_time=[r2std_time r2std];
    N=length(r);
```

```
N_time=[N_time N];
%%%%%%%%%%%%%%%%%%%%%%%%%%%%%%%%%%%%%%%%%%

%graph dist (plot1)
%%%%%%%%%%%%%%%%%%%%%%%%%%
subplot(2,2,1);
hist(rregular,x);
title('Size histogram');
xlim([0 6]);
xlabel('r size in nm');
[n x]=hist(rregular,x);
y1=max(n);
y2=round(4*max(n)/5);
y3=round(3*max(n)/5);
y4=round(2*max(n)/5);
y5=round(max(n)/5);
str1 = num2str(r2mean);
str1=['r2= ' str1 ' nm'];
text(4,y1,str1);
str2 = num2str(r2std);
str2=['std2= ' str2 ' %'];
text(4,y2,str2);
t=t+dt;
```

```
t_time=[t_time t];
str3 = num2str(t);
str3=['\tau= ' str3];
text(4,y3,str3);
str4= num2str(S);
str4=['S= ' str4];
text(4,y4,str4);
str5= num2str(N);
str5=['N= ' str5];
text(4,y5,str5);
hist_time=[hist_time; n];
%%%%%%%%%%%%%%%%%%%%%%%%%%%%

%subplot std vs. ave r (plot2)
%%%%%%%%%%%%%%%%%%%%%%%%%%%%%%
subplot(2,2,2);
plot(r2mean_time,r2std_time);
xlabel('mean radius of 2');
ylabel('std. dev. of 2');
%%%%%%%%%%%%%%%%%%%%%%%%%%%%%%

%subplot S and N (plot3)
```

```
%%%%%%%%%%%%%%%%%%%%%%%%%%%%%%%%%%%%%%%%%%%%%%
%%%%%%%%%%%%%%
    subplot(2,2,3);
    [haxes,hline1,hline2] = plotyy(t_time,N_time,t_time,S_time);
    xlabel('time');
    axes(haxes(1))
    ylabel('N');
    axes(haxes(2))
    ylabel('S');

%%%%%%%%%%%%%%%%%%%%%%%%%%%%%%%%%%%%%%%%%%%%%%
%%%%%%%%%%%%%%

    %subplot std dev (plot4)
    %%%%%%%%%%%%%%%%%%%%%%%%%
    subplot(2,2,4);
    plot(t_time,r2std_time);
    xlabel('time');
    ylabel('Std. Dev. of 2');
    %%%%%%%%%%%%%%%%%%%%%%%%%

    drawnow();
```

```
 end
    %saving data
    %%%%%%%%%%%%%%%%%%%%%%%%%%%%%%%%%%%%%%%%%%%%%%%%%%%%%%%%%%%%%%%%%%%%%%%
    S_time=S_time';
    save S_time.txt S_time -ascii
    N_time=N_time';
    save N_time.txt N_time -ascii
    hist_time=[x; hist_time];
    hist_time=hist_time';
    save hist_time.txt hist_time -ascii
    t_time=t_time';
    save t_time.txt t_time -ascii
    r1mean_time=r1mean_time';
    save r1mean_time.txt r1mean_time -ascii
    r1std_time=r1std_time';
    save r1std_time.txt r1std_time -ascii
    r2mean_time=r2mean_time';
    save r2mean_time.txt r2mean_time -ascii
    r2std_time=r2std_time';
    save r2std_time.txt r2std_time -ascii
    %%%%%%%%%%%%%%%%%%%%%%%%%%%%%%%%%%%%%%%%%%%%%%%%%%%%%%%%%%%%%%%%%%%%%%%
end
```